Electron beam lithography of a diffractive element for surface plasmon resonance sensing

Andra St. Quintin

Department of Electrical and Computer Engineering
McGill University, Montreal

August, 2012

A thesis submitted in partial fufillment
of the requirements for the degree of
Master of Engineering

ABSTRACT

Surface plasmon resonance (SPR) sensing is seen as a viable option for developing biological sensors that provide portable, real-time, integrated detection systems. Certain implementations of this sensing technique have already been commercialized, but there is a continued trend to provide systems that are ever-more compact and integrated. In accordance with this trend, previous work has designed a multi-channel SPR device which relies on diffractive lenses to couple light to and from its sensing spots. This thesis presents the development of a fabrication process for these lenses using electron beam lithography, and presents optical results from a prototype device. The fabrication process is demonstrated to provide a high degree of control for pattern alignment and for the size of fabricated features. The developed method is then used to create a reflective diffractive lens on a silicon substrate. The diffraction efficiency of the lens is measured to be approximately 18%, and the focal spot size of the lens is in accordance with predictions based upon the fabricated profile.

SOMMAIRE

La résonance plasmonique de surface (SPR) est considérée comme une option convenable pour le développement de capteurs biologiques offrant un système de détection portatif, en temps réel et intégré. Certains instruments utilisant cette technique de détection ont déjà été commercialisés; cependant, la tendance se maintient pour le développement de systèmes qui sont encore plus compacts et intégrés. Dans cette même direction, un dispositif SPR à multiples canaux basé sur des lentilles diffractives pour focaliser la lumière vers et depuis les régions de détection a été conçu précédemment. Cette thèse présente la conception d'un procédé de fabrication pour ces lentilles utilisant la lithographie par faisceau d'électrons ainsi que les résultats optiques obtenus avec un prototype. Il est démontré que le procédé de fabrication permet un grand contrôle de l'alignement du motif et de la taille des détails. La méthode conçue est ensuite utilisée pour créer une lentille diffractive et réflective sur un substrat de silicium. L'efficacité de diffraction de la lentille est de 18% environ et la taille du faisceau au foyer est en accord avec les prédictions basées sur le profile de fabrication.

ACKNOWLEDGEMENTS

I would first like to thank my supervisor, Prof. Andrew Kirk, for his guidance and feedback throughout the course of my degree. I was always grateful for his ability to suggest a different angle from which to approach the various fabrication challenges I encountered, and for his help in better understanding the underlying physical principles related to the design and performance of the lens.

I also wish to thank the microfabrication team – Dr. Matthieu Nannini, Dr. Lino Eugene, Mr. Don Berry, and Mr. John Li – for their extensive process development support, training on the various equipment, and tireless maintenance of the facility. Many thanks are also due to Prof. Thomas Szkopek for his expertise and insight into the workings of the electron beam lithography system, and his creative suggestions for overcoming problems in order to utilize the system to its absolute limits. I also appreciate the help provided by Dr. Joe Nabity in customizing the drivers of his NPGS software to interface correctly with our system to improve the control of the stage position.

This thesis was based upon a great deal of previous design work completed by Imran Cheema, whom I would like to thank for passing on all the relevant design details throughout the fabrication process, as well as for his many constructive suggestions with regards to testing and analysis. I am also grateful for the support from the many members of the Photonics Systems Group, in particular Phillip Roche, Sandrine Filion Côté, and Venkat Veerasubramanian for their guidance in the lab and helpful comments with regards to data analysis.

Many thanks are also due to Samantha Grist for her careful reading of this document and her feedback on the areas that required greater detail or clarity.

Lastly, I would like to thank my family for the love and support that continually flowed from the West Coast.

TABLE OF CONTENTS

GLOSSARY OF TERMS AND ACRONYMS

EBL	Electron Beam Lithography
EL 6	EBL copolymer resist (6% solids in Ethyl Lactate)
ELISA	Enzyme-Linked Immunosorbent Assay
MAGscale	EBL parameter relating magnification and field of view
NPGS	Nanometer Pattern Generation System (control software)
PMMA	Polymethyl methacrylate (EBL resist)
raster rotation	SEM parameter controlling the angle of the field
RCWA	Rigorous Coupled Wave Analysis
RIE	Reactive Ion Etching
RIU	Refractive Index Units
SEM	Scanning Electron Microscope
SPR	Surface Plasmon Resonance

1 : INTRODUCTION

1.1 Overview

With the emerging popularity of lab-on-a-chip devices, it is desirable to develop biological sensors that can be effectively integrated with microfluidic systems to provide portable and real-time detection. A potential candidate for this type of application is surface plasmon resonance (SPR) sensing, which can optically interrogate certain bio-chemical properties of a sample. One key aspect of an integrated SPR sensor is the lens system that directs light to and from the detection spots, thus eliminating the mechanical scanning components found in conventional SPR systems. This thesis presents work on the development of a fabrication process for an array of diffractive micro-lenses for an integrated SPR system.

In this document, Chapter 1 provides an introduction to SPR sensing and the concept of diffractive lenses, Chapter 2 reviews existing literature related to the theoretical efficiency and practical fabrication of diffractive lenses, Chapter 3 presents the design specifications of the particular lenses for the system, Chapter 4 details the fabrication process and the particular challenges overcome while implementing it, Chapter 5 presents fabrication and optical results, and Chapter 6 provides a conclusion and summary of future fabrication work for the project.

1.2 Motivation: Integrated SPR Sensing

1.2.1 The Need for Integrated Sensors

In a multitude of biological applications, specific protein markers or DNA segments are used as the means of identifying a particular disease. Although there are already several well-established techniques for identifying and quantifying these types of biological analytes, such as immunoassays and mass spectrometry, these methods are generally time consuming, complicated, and require bulky equipment. Consequentially, a miniaturized and integrated microfluidic sensing system has the potential to provide considerable improvement over currently used methods for both point-of-care diagnostic applications [1, 2] and drug discovery investigations [3, 4].

In many senses, the conventional gold standard for detecting specific proteins or DNA sequences is the enzyme-linked immunosorbent assay, or ELISA [5]. Its basic operation involves introducing a sample with the potential antigen to the detection surface, where the antigen will bind. The surface is then washed with a liquid containing antibodies, which bind to the antigen of interest. These antibodies are also linked to an enzyme, which are labelled with fluorescent tags, or are linked to an enzyme that will change the colour of a subsequently added enzyme substrate. The intensity or colour of each sensing spot is then compared to reference spots to determine the concentration of antigen present. This process is highly sensitive and highly parallelized, but typically takes anywhere from several hours to a few days to complete [5]. As such, it is incapable of providing real-time detection, and is also not very practical for developing into a portable system for point-of-care diagnostics.

Another traditional analysis technique is mass spectrometry, in which particles from the sample are ionized and vaporized, and then separated by their mass-to-charge ratio using electric or magnetic fields. The resulting currents for different ratios are then amplified and measured, providing a unique relative abundance graph for a wide variety of molecules [6]. Although some research has explored the possibility of miniaturizing mass spectrometry sensors [7], currently the demonstrated systems are mostly limited to gaseous samples, which severely limits their areas of application [8].

With the shortcomings inherent in these types of conventional techniques, there is a need for sensors that are capable of providing real-time detection, and that can more easily be miniaturized and parallelized. Unlike ELISA, SPR sensors are capable of real-time detection since they do not require the multiple washing steps required to introduce a fluorescent tag or activate a transducing enzyme, although the trade-off for this speed is a lack of molecular specificity. Additional wash steps can be incorporated into SPR sensing to create sandwich or inhibition assays for increased specificity [9], or to introduce other molecules such as gold nanorods for signal enhancement [10]; however, these methods still tend to be faster than ELISA. SPR sensors are also advantageous because they are well-suited to miniaturization and parallelization, since the sensing mechanism is comparatively simple to implement and can be integrated into a small area. Consequentially, SPR sensors are being extensively investigated as a contender for the ultimate goal of commercially providing a faster and cheaper alternative to existing methods for biological detection.

1.2.2 Surface Plasmon Resonance Sensors

A surface plasmon is defined as the quantization of a wave of collective electron oscillations at the surface of a metallic interface [11]. Accordingly, SPR is the phenomenon whereby under specific conditions, light incident on a surface couples into this evanescent electromagnetic mode along the metal surface. For such coupling to occur, the momentum of the incoming light must match the momentum required for a surface plasmon. In SPR sensors, one of the most widely used geometries for momentum matching is the Kretschmann configuration [12, 13], where a high-index prism couples light to a thin metal interface with a lower index dielectric on the other side as illustrated in Figure 1.1a. The surface plasmon is then generated at the interface between the metal and the second dielectric, with a resonance condition that is a function of the wavelength of light, the incident angle, and the effective refractive index at the interface.

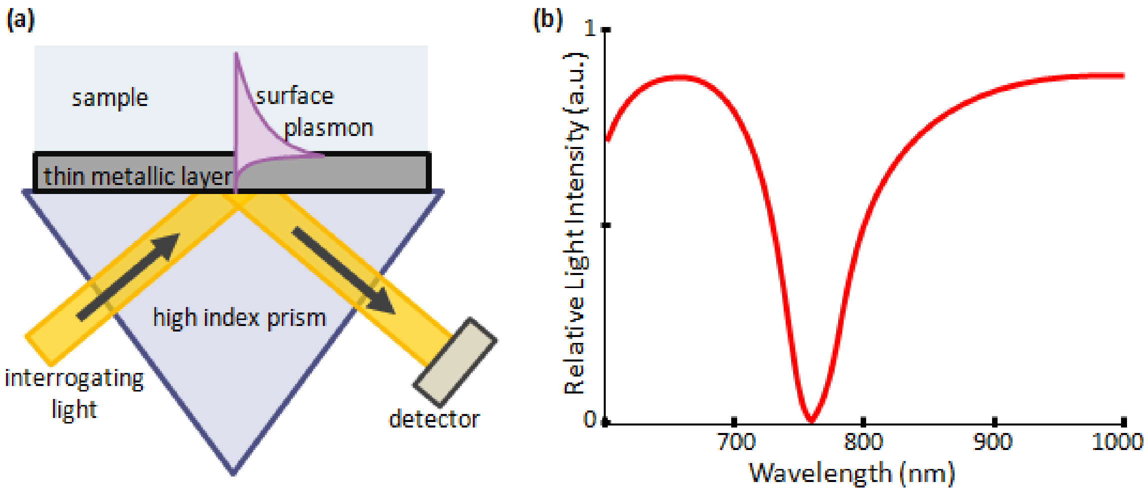

Figure 1.1: (a) Coupling light into a surface plasmon mode using the Kretschmann configuration. (Based on figure from [12].) **(b)** Typical sensing curve for an SPR configuration using wavelength-based interrogation. (Based on figure from [14].)

SPR sensors observe the light reflected back off a sample over a range of angles or wavelengths, with the minimum reflection corresponding to the maximum coupling of light into the surface plasmon mode, as shown in Figure 1.1b. This resonance point is highly sensitive to the refractive index of the interface, and therefore very small changes in refractive index can be observed based on the angle or wavelength at which maximum coupling occurs. For biological applications, a suitable surface, typically gold, is functionalized with bio-molecules that are able to capture the particular biological analyte of interest. Microfluidics then introduce the biological sample to the sensor spot, and if the analyte is present it will bind to the functionalized surface. Analytes bound to the surface very slightly modify its refractive index, which can then be observed by interrogating the sample from the opposite side using SPR. The greater the concentration of analyte present on the surface, the greater the change in the refractive index, and therefore the greater the shift in the observed resonance.

When used in a diagnostic context, one of the goals of SPR sensors is to be able to detect pathogens earlier than is possible with conventional methods, which implies detecting exceptionally low concentrations of analytes. Commercial SPR sensors are typically able to detect concentrations down to approximately 1 pg/mm^2 of an adsorbed analyte [15]. However, the exact detection limit of an SPR sensor in terms of analyte concentration depends on the specific application, and on the particular functionalization of the surface to capture the analyte of interest [16, 17]. The molecular specificity required to distinguish a particular analyte against a background of other biological molecules in a solution also varies widely between applications [18, 19], the details of which are beyond the scope of this thesis.

To isolate the optical performance of SPR sensors, their sensitivity and noise level are typically characterised by the refractive index change that they are able to detect, denoted in terms of refractive index units (RIU), a parameter which is independent of specific applications. Currently, the best SPR sensors have noise detection limits in the range of 10^{-7} RIU [14, 20], which is approaching a range that is capable of providing detection comparable to other sensing methods. Statistical calculations have suggested that detector shot noise is ultimately the limiting factor for RIU resolution of SPR systems, with analysis of several prior experimental results indicating that existing systems are operating close to this limit [20]. Consequentially, resolution limits could be improved by capturing a greater photon flux by using larger or faster detectors [20]. Longer integration time of a signal could also improve the resolution limit, but this solution may not be practical for observing certain fast binding events [21]; and more importantly, uncontrollable temperature drift generally prevents extended integration periods because a change of 0.1°C will induce a 10^{-5} RIU change [22]. Separate from the predominant issue of shot noise, some improvements may also be possible by increasing the coupling between incident light and surface plasmons, using techniques such as the use of metal waveguides to create hybrid plasmons [20]. Regardless, whether the limiting factor in a particular sensor's performance is actually its optical detection limit or its biological surface functionalization depends largely on its specific application. For instance, selectively detecting a particular protein against a background of many other proteins would require improved surface chemistry, whereas tracking a rapid real-time binding event might only require improved optical capabilities.

1.2.3 Miniaturized SPR Sensors

Early implementations of SPR sensors utilized the geometry shown in Figure 1.1a, and used rotation stages to scan the incident beam over the desired range of angles and a simple photodetector to measure the resulting intensity [23]. However, it is generally desirable to avoid such mechanical components, especially when miniaturizing a system. Consequentially, focused beam methods for providing angular interrogation are more common, whereby a lens is included prior to the prism to focus incident light to a point on the sample surface, which simultaneously provides a range of angles at the surface that can then be re-collimated and recorded by a photodiode array [24, 25]. Efforts to miniaturize and integrate SPR sensors have explored multiple alternative avenues, such as implementations based on fibre [26], waveguide [27], and imaging [28] configurations; however, these methods tend to have less sensitivity than the conventional approach of coupling light through a bulk prism [15]. Several integrated SPR systems using prism-based configurations have been previously demonstrated, most notably the commercially produced Spreeta sensor. Pictured in Figure 1.2, this design encapsulates a compact light source, prism, and detector array into a hand-held device. Using time-averaging techniques, the noise limit of the Spreeta 2000 sensor has been measured as 1.8 $\cdot 10^{-7}$ RIU [29].

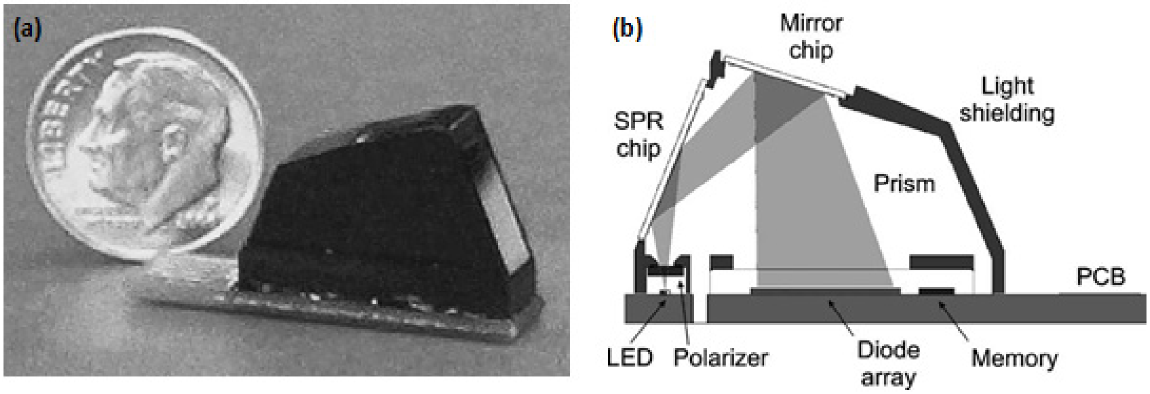

Figure 1.2: (a) Photograph of the Spreeta 2000 sensor, with a coin shown for size comparison. **(b)** Schematic of the inside of the Spreeta 2000 sensor, with the entire beam path occurring within the prism. (Reprinted with permission from [29].)

In order to take advantage of the sensitivity generally associated with the prism-coupling approach while also providing a system that can be further miniaturized and parallelized, micro-diffractive lenses have been demonstrated as method to focus light onto a detection spot, thus providing a range of angular interrogation. As illustrated in Figure 1.3a and b, this type of design replaces the focusing optics, coupling prism, and index matching gel with a single injection moulded chip that has been patterned with diffractive optics [30]. Additional work based on the same principle has taken advantage of the fact that the feature sizes of the diffractive optics can be larger and therefore easier to fabricate if they are designed for light incident at an angle as opposed to light normal to the surface [31]. The chip layout for this design is illustrated in Figure 1.3c and d. The normal and angled-incidence designs have demonstrated detection limits of $5 \cdot 10^{-7}$ and 2.6 $\cdot 10^{-5}$ RUI, respectively.

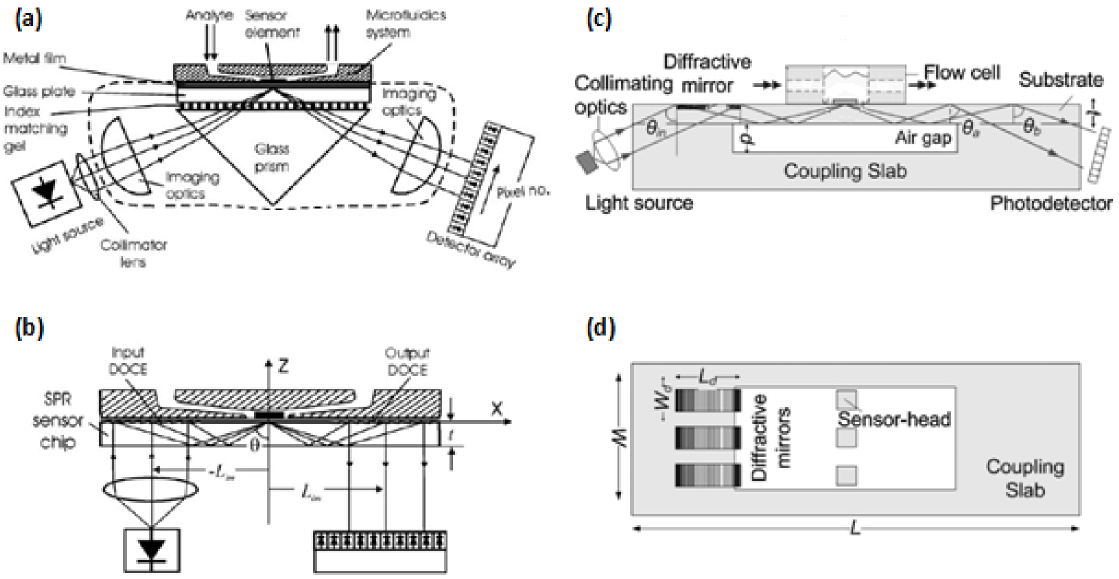

Figure 1.3: (a) Side-view illustration of a conventional prism-based coupling geometry, where the components encircled with a dotted line are replaced in the design of **(b)** with an injection moulded slab of plastic patterned with diffractive optical elements. (Reproduced with permission from [30].) **(c)** Side view of a second diffractive optics SPR design illuminating the diffractive optics at an angle as opposed to at normal incidence. **(d)** Top view of the same design. (Reproduced with permission from [31].)

In spite of these considerable advances, SPR sensors are still not yet able to seriously compete with the well-established classical techniques in the mass market. As such, the long-term goal for this multichannel SPR sensor project is to achieve further miniaturization and parallelization of the diffractive sensing optics without seriously compromising the system's detection limits. Ultimately, this system will be capable of providing a real-time and portable diagnostic system with a wide variety of potential applications.

1.3 Diffractive Lenses

Diffractive lenses are a logical choice for focusing and collimating light in an integrated SPR array because they are easier to miniaturize compared to refractive lenses and can be more easily adjusted to correct for spherical aberrations [32]. Although diffractive lenses have the limitation of being designed for a single wavelength, angular-based SPR sensors operate at a single wavelength, so this limitation is not of concern. A more detailed description of the theory, efficiency, and fabrication of diffractive lenses follows in Chapter 2, but a preliminary explanation of diffractive lenses is provided here for introductory purposes.

The most intuitive explanation of a diffractive lens involves its derivation from the more familiar refractive lens. Rather than considering the lens in terms of classical ray optics, it should be considered in terms of interference owing to the phase difference imparted along various paths. When travelling a distance d through a medium of refractive index n, light of wavelength λ will experience a phase shift of $2\pi d\cdot(n-1)/\lambda$ as compared to light travelling the same distance in air. As illustrated in Figure 1.4a, the phase shift imparted by a refractive lens varies across its diameter, and typically varies by several multiples of 2π through its thickness along the optical axis. However, in terms of optical interference, a phase shift of 2π is indistinguishable from a phase shift of 0, and therefore the lens profile in Figure 1.4a is optically equivalent to its 2π modulus shown in Figure 1.4b. For fabrication purposes, the profile can be discretized as shown in Figure 1.4c.

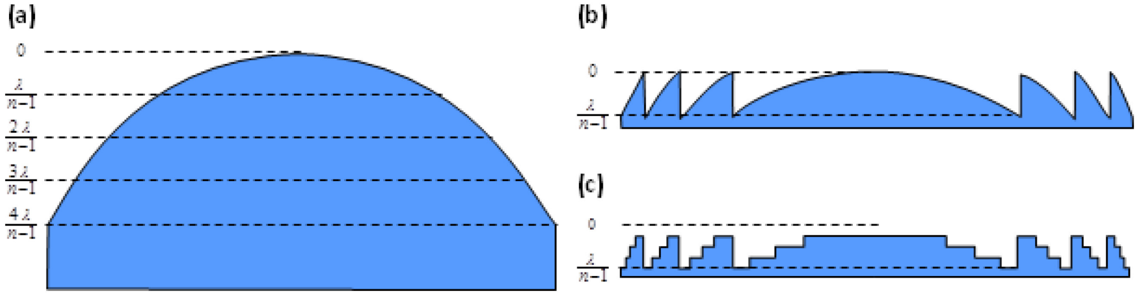

Figure 1.4: (a) Side view of a refractive lens, with dashed lines indicating distances through the lens at which a multiple of a 2π phase shift is added. **(b)** The 2π modulus of the same lens. **(c)** A discretized version of the same lens, with heights providing π/2, π, and 3 π/2 phase shifts. (Adapted from [33].)

Each section of the lens where its profile varies from a zero to 2π phase shift is referred to as an optical zone, or Fresnel zone. By considering the geometry required such that all contributions from the zones in a lens add constructively at the focal point, it is possible to show that for a given focal length f, the zone boundary locations, R_m, are given by

$$R_m = \sqrt{mf\lambda}, \tag{1.1}$$

where m is the zone order [34]. In the case of a circular lens, this relationship implies a series of ever-narrower concentric rings as illustrated in Figure 1.5a. However, in this particular project, the intent is to use a cylindrical lens to focus light in just one optical axis, which is realized with a collection of parallel lines that become narrower as they move away from the optical axis, illustrated in Figure 1.5b. Specifically, the geometric layout of this project utilizes an off-axis lens, meaning that only a portion of the total lens is required.

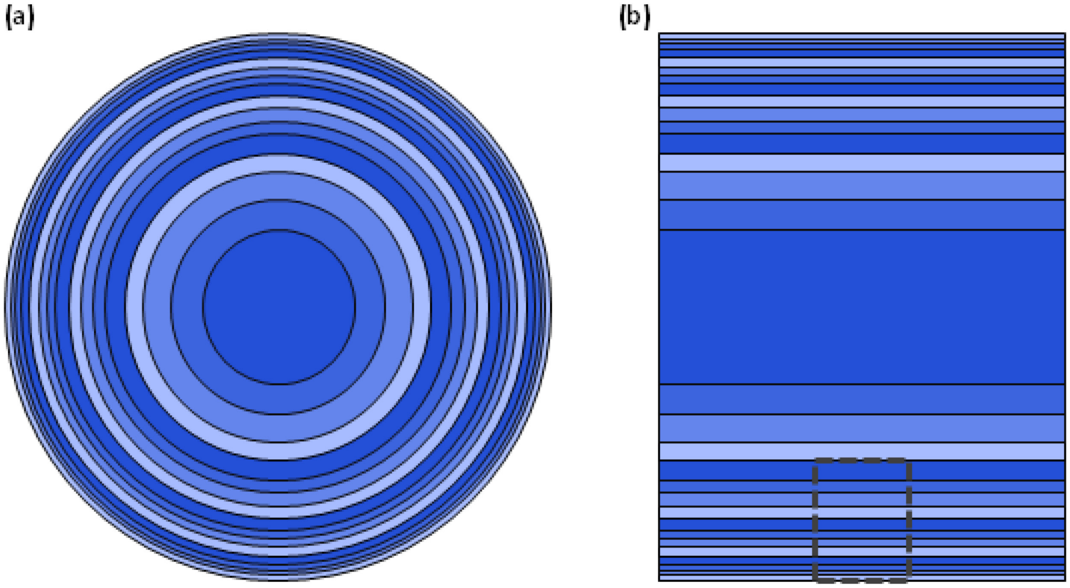

Figure 1.5: (a) Top view of a circular diffractive lens similar to that shown in Figure 1.4c. **(b)** Top view of a cylindrical diffractive lens similar to that in Figure 1.4c, with the dashed lines showing where a portion of an off-axis lens might be selected away from the optical axis.

One of the most obvious concerns when designing a diffractive lens is its efficiency. As will be discussed in detail in the next chapter, the more closely a discretized lens can approximate the ideal continuous profile, the higher its diffraction efficiency will be. In practice, diffractive lenses always have lower efficiency than refractive lenses; however, in a compact and multi-channel SPR system it is important to maintain a reasonably high efficiency. Minimizing the size of the light source and its power supply is important for portability reasons. But at the same time, the illumination must be distributed over a large number of sensing channels with sufficient intensity in each channel to provide adequate sensitivity for biological sensing. Efficient lenses are also important because un-diffracted light would create undesirable background light across the multi-channel device, which would contribute to optical noise and result in reduced sensitivity. Nevertheless, in this type of application, the ease of integration of diffractive lenses still makes diffractive lenses a more attractive option in spite of their challenges with regards to efficiency.

One integration advantage of diffractive lenses compared to refractive lenses is their reduced thickness, which is important in terms of microfabrication logistics. This consideration is particularly significant when designing an off-axis lens, since the further away the area of interest is from the optical axis, the steeper its profile would be in a refractive lens. The trade-off for this reduction in thickness is that the steeper profile translates into ever-decreasing feature widths in the diffractive lens design, which must be taken into consideration in conjunction with fabrication limitations.

In addition to the consideration of lens thickness, diffractive lenses are also attractive compared to refractive lenses when considering aberrations. To compensate for third order aberrations, larger-scale refractive lenses rely on doublet, triplet, or even more complicated lens pairings, or on the use of aspheric surfaces. At the micro-scale, multiple lens surfaces pose a difficult problem in terms of fabrication or alignment, and although moulding of small-scale aspheric surfaces is possible, it is challenging in the case of micro-lens arrays [35]. By comparison, it is straightforward to lay out arrays of diffractive lenses. Compensating for aberrations in a diffractive lens is also relatively straightforward: the discretized profile can be altered to approximate aspheric surfaces with no increase in the fabrication complexity. Again in the context of an off-axis lens, this design flexibility is useful because aberrations in spherical lenses become more noticeable further away from the optical axis. The design requirements of this particular project also require non-normal illumination of the lens, which also requires aberration correction that can be accommodated in the discretized profile.

1.4 Summary

Despite their advantages, diffractive lenses still present certain challenges in terms of fabrication, primarily those relating to minimum feature widths and small variations in feature pitch. The lenses designed for the SPR sensor system in this project require feature widths on the order of 300 nm, owing to their comparatively short focal length, off-axis configuration, and four-level profile. Consequently, the majority of the work presented in this thesis relates to developing a fabrication process that is capable of consistently and accurately transferring the required pattern into the substrate. To demonstrate the capabilities of this process with respect to diffractive lenses, this thesis also presents optical results from a simplified prototype lens.

The major research contributions contained within this thesis are as follows:

- development of an electron beam lithography field-stitching protocol:
    - demonstration of a method to determine the required raster rotation value for aligning the microscope and stage axes without pre-existing alignment marks,
    - identification of issues involved in field stitching in both x and y axes and a demonstration of a method to overcome these problems,
- demonstration of a calibration method for electron beam lithography patterns to overcome proximity effects in order to obtain desired feature widths,
- demonstration of a functioning cylindrical diffractive lens:
    - fabrication of a lens with dimensions of 1 mm in the focusing axis and 100 μm in the non-focusing axis,
    - quantification of the spot size and diffraction efficiency of the +1 and -1 diffractive spots,
    - analysis of loss mechanisms resulting from fabrication imperfections,
- description of avenues of future work and suggested approaches.

2 : DIFFRACTIVE LENSES: DESIGN AND FABRICATION

2.1 Introduction

The fabrication of diffractive lenses for an SPR application builds on a considerable amount of previous work related to both the design and fabrication of diffractive optics. This chapter first presents a brief review on the theory of diffractive lenses and its importance for optimizing the geometry of diffractive lenses to maximize their efficiency, and then presents a review of the most commonly used fabrication techniques and some of the designs that have been realized using these methods.

2.2 Theory of Diffractive Lenses

The initial explanation of diffractive lenses provided in Chapter 1 considered a diffractive lens as an approximation to the phase profile of a conventional lens surface. However, other design approaches can be taken to determine the spacing of optical zones. Furthermore, a more complete understanding of diffractive lenses can be obtained by considering Maxwell's equations and the propagation of light first as predicted by scalar theory, and then by the use of rigorous coupled wave theory. These models are important for optimizing the zone boundary locations and step heights of a diffractive lens to maximize its diffractive efficiency.

2.2.1 Zone Profiles from the Localized Grating Equation

Instead of considering the phase profile of a cylindrical diffractive lens in terms of a 2π modulus of a refractive lens, it is also possible to consider it as a diffraction grating with a non-uniform period across its width [36-38]. Collimated incident light at an angle θ_1 can be focused by a diffractive lens if the lens diffracts light at different angles of θ_2 at different positions along the lens. These angles can be determined trigonometrically as illustrated in Figure 2.1, and given by

$$\theta_2(x) = \tan^{-1}\left(\frac{x}{f}\right), \tag{2.1}$$

for a position a distance x from the optical axis and a focal length of f. From these angles, it is possible to rearrange the grating equation [39] to solve for the localized period of the lens, Λ, as

$$\Lambda(x) = \frac{m\lambda}{n_2 \sin(\theta_2(x)) - n_1 \sin(\theta_1)}, \tag{2.2}$$

where m is the diffracted order, λ is the wavelength of light, and the angles and refractive indices are as illustrated in Figure 2.1.

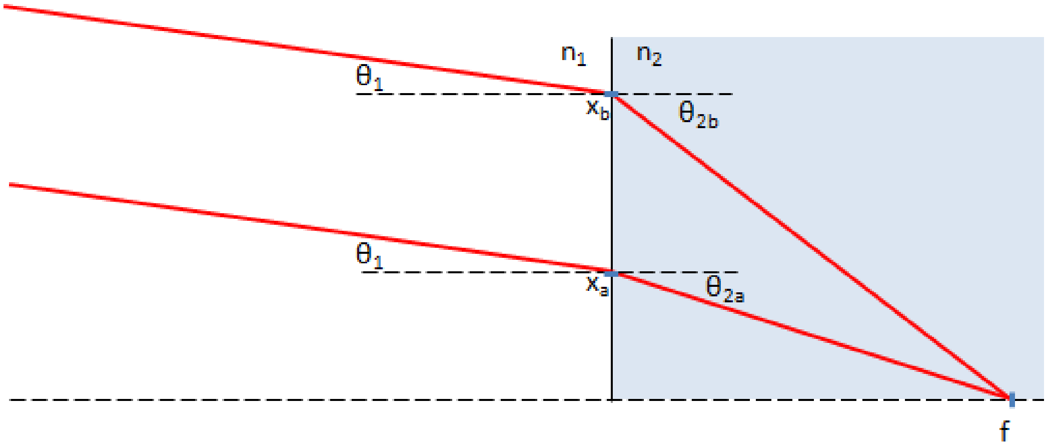

Figure 2.1: Illustration of positions and angles to be used when calculating the local period of a refractive lens using Equation 2.1 and Equation 2.2.

This formulation can be particularly useful in the case of off-axis lenses or large incident angles, where the equivalent aspheric refractive surface may be less straightforward to determine. In the case of an off-axis lens that starts a distance x_a from the optical axis, the width of its first Fresnel zone, $\Lambda(x_a)$, will be given by Equation 2.2. The next Fresnel zone will begin at a point x_b, equal to $x_a + \Lambda(x_a)$, and again its width can be found using Equation 2.2. This process can be repeated across the total width of the lens.

The grating equation is based upon a scalar theory of diffraction, which is described in further detail in Section 2.2.2. As will be discussed in Section 2.2.3, the diffraction efficiency predicted by scalar theory becomes invalid as feature sizes become comparable to the wavelength of light and thus a rigorous theory is required. However, even for small feature sizes, the diffraction *angles* predicted by scalar theory remain correct [40]. It has been shown that at a wavelength of 633 nm incident on a grating with a period of 833 nm, deviations from the diffraction angle predicted by scalar theory are less than 0.5° for diffraction angles less than 88° [41]. Therefore, although scalar theory will not accurately predict the efficiency of a diffractive lens with features comparable to the wavelength, the grating equation will still be correct for predicting the location of its focal point.

2.2.2 Scalar Theory Diffraction Efficiency

For scalar theory to be valid, it must be assumed that the electric and magnetic fields are uncoupled and thus can be solved independently. This approximation is reasonable when the features of interest are large in comparison to the wavelength of light, and when the observation plane is located in the far-field [42]. By also working in the paraxial limit and by approximating circular wavefronts as quadratic wavefronts, the problem becomes further approximated by the Fraunhofer diffraction regime, wherein the resulting diffraction pattern at an observation plane is given by the two-dimensional Fourier transform of the phase object [40].

In the context of scalar theory, a diffractive lens can essentially be thought of as a phase grating, where the period of the grating varies as a function of position across the lens as described in Section 2.2.1. Therefore, when designing diffractive lenses it is helpful to first consider the efficiency of an infinite grating with a fixed period. To do so, it is necessary to calculate the far field diffraction pattern expected for each sub-level in a period using the Fourier transform, add together all sub-levels to evaluate the contribution from a single period, and then add the contributions from an infinitely long grating. For an N level grating with normal illumination, it can be shown that scalar theory predicts the maximum possible efficiency of the first diffraction order, η_{max}, will be [32]

$$\eta_{max} = \left[\frac{\sin\left(\frac{\pi}{N}\right)}{\pi/N}\right]^2, \tag{2.3}$$

and that the depth of each sub-level, d_m, should be

$$d_m = \frac{m\lambda}{N(n_2-1)}, \tag{2.4}$$

where n_2 is the refractive index of the grating material, and m is an integer from 0 to N-1. Plotting Equation 2.3 in Figure 2.2, it is clear that significant increases in diffraction efficiency are expected for designs with more than two levels, with close to 100% diffraction efficiency expected for sixteen and thirty-two level designs.

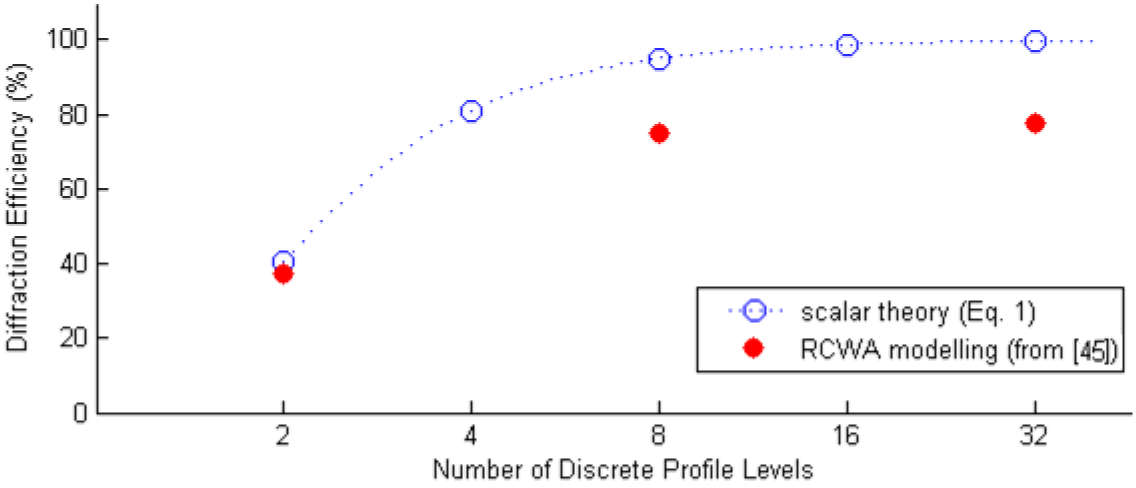

Figure 2.2: Diffraction efficiency as a function of discretization levels, showing predictions based on the scalar theory of Equation 2.3 (open circles), and predictions based on rigorous theory for a TM polarized plane wave (solid circles). (Based on data from [45].)

2.2.3 Rigorous Theory

As the width of features in a diffractive element become comparable to the wavelength of light, scalar theory begins to break down. Although its predictions for the angles of diffractive orders remain accurate, it no longer accurately predicts the diffraction efficiency [40]. Therefore, more rigorous methods of solving Maxwell's equations are required, which involve the consideration of wave propagation in three regions: the modulated region of the grating, as well as the dielectric on either side [40].

A number of such methods exist [43], but one of the most common is rigorous coupled wave analysis (RCWA), which was first demonstrated to model diffraction from a sinusoidal grating with light at non-normal incidence [44]. In short, RCWA involves finding the solution to the coupled wave equations in the three distinct regions using the superposition of many waves, and then matching the boundary conditions. It improves on previous coupled wave methods by making fewer assumptions, most notably by including higher-order waves and second order derivatives of the field amplitudes. It also uses a matrix formulation to obtain a solution, as opposed to a modal approach, which requires more complicated methods [44]. Since its introduction, RCWA has proven popular in the analysis of diffraction gratings because it is relatively simple, provides comparatively fast convergence, and is versatile for a wider variety of grating designs [43].

By extending the use of RCWA to diffractive lenses, it is possible to obtain more accurate results of their expected efficiency as the feature sizes become sub-wavelength. For example, RCWA was applied to investigate the theoretical performance of cylindrical diffractive lenses designed for a wavelength of 1.0 μm with a diameter of 50 μm and focal length of 100 μm, which were modelled as continuous, 32-level, 8-level, and 2-level profiles [45]. Their predicted efficiencies are compared with the efficiencies predicted by scalar theory in Figure 2.2. For the 2-level grating, the minimum feature size is 2.5 µm, and it can be seen that the scalar theory only slightly overestimates the lens' efficiency. However, for the 8 and 32-level profiles the features become sub-wavelength, and RCWA predicts a substantially lower efficiency than that expected from scalar theory.

To address this shortcoming, rigorous theory can be used in conjunction with parametric optimization to adjust the geometry of a lens to improve its efficiency. By adjusting the sub-zone boundaries in a 4-level structure, it is possible to overcome the very low efficiency associated with a resonance effect that occurs at feature sizes comparable to the wavelength, with predicted performance comparable to or even exceeding scalar predictions [36]. Further work along the same lines suggests that this optimization should be particularly pronounced for off-axis lenses, although the optimized design presents an even greater fabrication challenge because it reduces the feature sizes even further [37]. An illustration of one such optimization is presented in Figure 2.3.

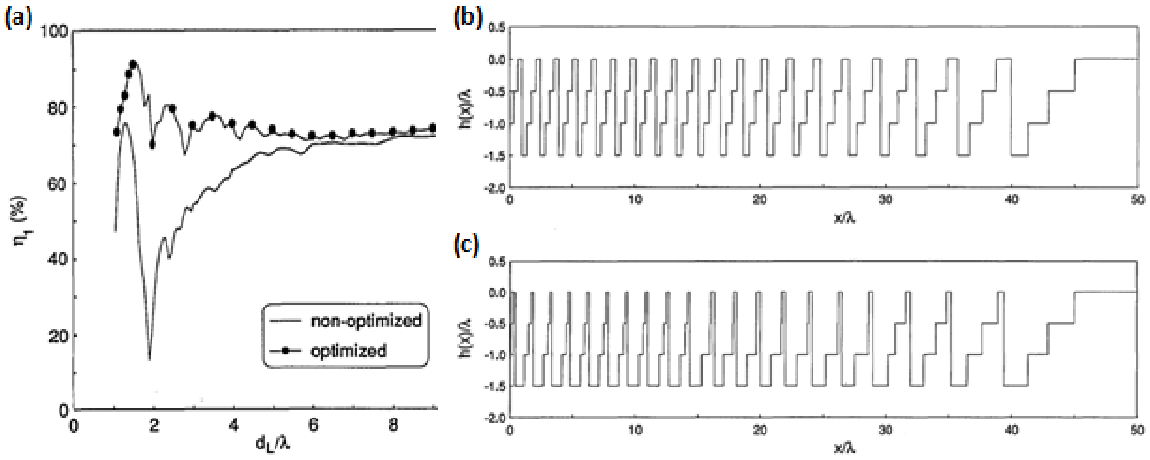

Figure 2.3: (a) Diffractive efficiency for a 4-level structure as a function of zone width divided by wavelength for optimized and non-optimized geometries. **(b)** Lens profile of non-optimized design. **(c)** Lens profile of optimized design. (Reproduced with permission from **[37]**.)

Rigorous analysis is also useful for modelling the effects of various types of fabrication errors on diffractive lens performance. For larger lenses fabricated with optical lithography, the effects of mask misalignment, overexposure, and etch depth errors have been studied, with typical mask alignment errors causing the worst degradation in performance [46]. The premise of this work was that the small feature variations resulting from fabrication errors would not adequately be captured by scalar analysis. The results showed that scalar and rigorous estimations of diffraction efficiencies differed by 5-10%, with more severe differences for smaller f-number lenses.

2.3 Primary Fabrication Method: Electron Beam Lithography

Particularly in the cases of short focal lengths and off-axis lenses, diffractive lens designs often include sub-micron features which require an alternative to conventional optical lithography. Therefore, prior to surveying a number of diffractive lenses reported in the literature, it is worthwhile considering one of the most commonly used tools in their fabrication: electron beam lithography (EBL).

In traditional photolithography, diffraction effects around the edges of the physical patterning mask become significant for sub-micron features, leading to unresolved or poorly defined features. Although industrial-scale facilities continue to push the limits with deep-UV lithography to obtain ever-smaller minimum feature sizes [47], most recently the 22 nm CMOS manufacturing process developed by Intel [48], research facilities typically have not readily had access to these types of machines. In contrast, EBL is a direct-write patterning technique that traces out patterns with a high energy electron beam, where the wavelength of the electrons is not the limiting factor in feature sizes. Furthermore, EBL provides a high degree of flexibility during the prototyping and development process, since the patterns only require definition in software as opposed to a physical mask.

Similar to a scanning electron microscope, an EBL system essentially consists of an electron emission source, generally using either Schottky emission or cold field emission; an accelerating voltage, ranging from 10 to 100 kV; and magnetic or electrostatic focusing lenses [49, 50]. Dedicated lithography systems, such as those provided by JEOL, Vistec, Elionix, and Crestec, tend to offer the highest performance; however, companies such as Raith and Nabity also offer conversions to existing electron microscope systems [51]. A schematic of the electron optics in the Hitachi SU-70 electron microscope used for this thesis work is shown in Figure 2.4a. The condenser lenses and objective lens are electro-magnetic coils that exert a magnetic field with radial and axial components. The Lorentz force from these coils causes the electrons to travel in a spiral path, focusing them towards the microscope axis, as illustrated in Figure 2.4b [52].

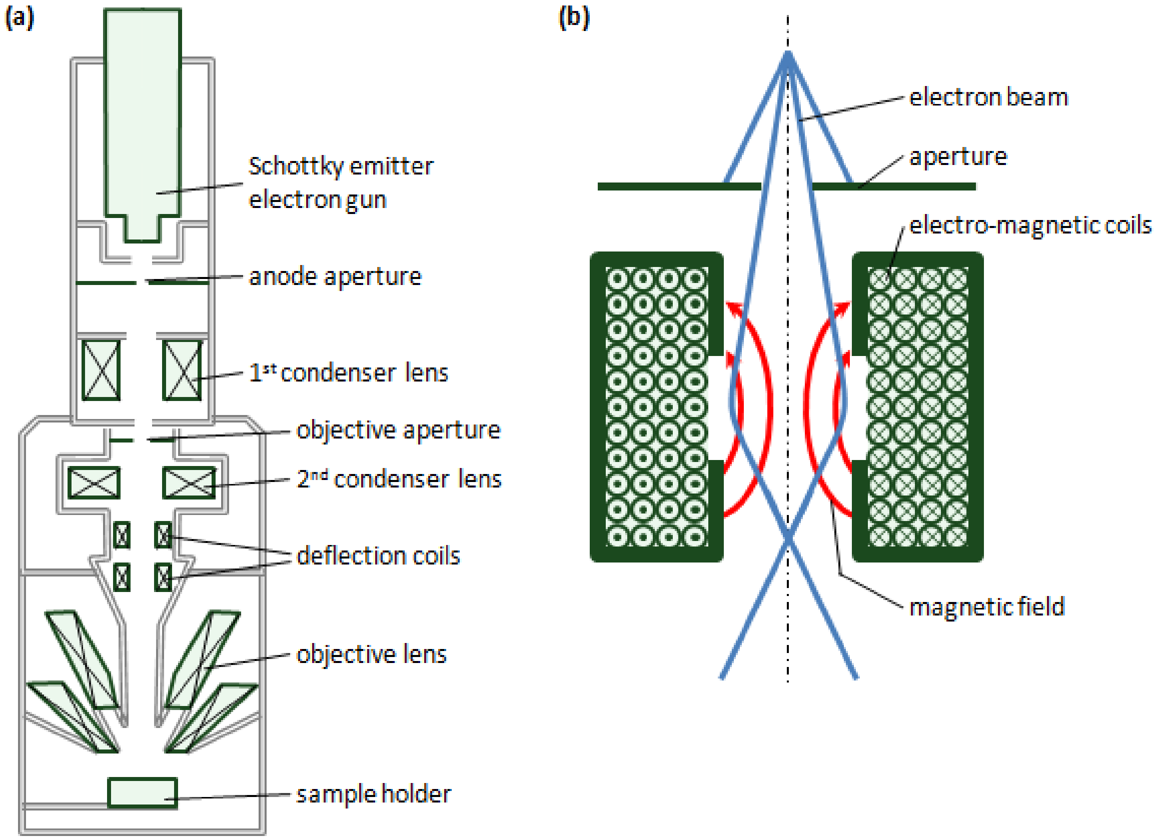

Figure 2.4: (a) Simplified schematic cross-section of the electron focusing optics in the Hitachi SU-70 electron microscope. (Based on figure from [53].) (b) Schematic cross-section of the function of a magnetic electron lens. (Based on figure from [52].)

In essence, pattern transfer in an EBL system involves focusing the electron beam to a very tight spot, and then using computer control to laterally deflect the beam such that it traces out patterns defined in software. The beam transfers the patterns into an electron-sensitive resist, a layer which can be envisioned as analogous to a light-sensitive film in photography. Polymethyl methacrylate (PMMA) is one commonly used resist [54], consisting of polymer chains that are broken apart by electron beam exposure, allowing them to be subsequently removed in a suitable solvent [55]. PMMA is useful for creating diffractive optics because it is transparent in the visible spectrum, and because its index of refraction is between 1.48 and 1.50 [56], it can be closely matched to a glass substrate if required.

PMMA is also well suited for use in conjunction with liftoff and etching techniques for diffractive optics that require pattern transfer into the substrate. The dose required for PMMA exposure varies quite dramatically depending on its thickness, the size and density of features, the conductive properties of the substrate, and the accelerating voltage, with a dose of 50 to 500 μC/cm^2 recommended by one common manufacturer [57]. Many variations exist in the solvents used for development, although there are a few fairly standard developer mixtures [58]: methyl ethyl ketone:ethanol (MEK:EtOH) at a ratio of 26.5:73.5, 2-ethoxyethanol:methanol at a ratio of 3:7, or methyl isobutyl ketone:2-propanol (MIBK:IPA) at a ratio of 1:3.

Basic EBL is generally considered to have a lateral resolution limit on the order of 10 nm, with the nature of the polymer bonds during resist development suggested as the limiting factor [59]. For most diffractive lenses, feature sizes down to the 10 nm scale are not necessary; however, very stringent feature width tolerances are often required, meaning that the ability to control the patterning on the order of 10 nm is important. Of particular concern with regards to this feature control is the proximity effect in electron beam lithography, whereby backscattered electrons increase the exposure dose in the area surrounding the actual beam location, which tends to widen features that are in close proximity to each other [60]. Such effects are particularly difficult to deal with in diffractive optical structures owing to the densely packed features over a large area [61].

Although other patterning methods for diffractive lenses with sub-micron features do exist, such as diamond turning [62], direct laser writing [63], and interferometric laser writing [64], the majority of reported techniques do involve the use of EBL.

2.4 Previously Fabricated Diffractive Lenses

Presented below are a number of diffractive lenses which have been reported in the literature, consisting of various lens geometries, materials, and fabrication methods. When considering these designs, there are a number of important distinctions to be made. Multi-layer diffractive lenses are desirable because of their improved efficiency over two-level designs; however, they are more difficult to fabricate. Fabrication considerations also involve the feature sizes required, which are directly proportional to the focal length of the lens. A related consideration is the overall size of the lens: a lens with a large aperture but a short focal length is typically difficult to obtain owing to the difficulty of patterning increasingly small features over a large area. Finally, the choice of substrate is dependent on the required wavelength, with visible wavelengths typically using polymer resists, quartz, or fused silica; and infrared wavelengths typically using polymer resists, silicon, or gallium arsenide.

2.4.1 Polymer Lenses

Micro-scale Fresnel lenses for visible or near-visible applications were first fabricated in the early 1980’s, initially as an alternative to graded-index micro lenses [65]. For this work, 650 μm of PMMA was spin-coated on a glass substrate and then covered with a thin layer of gold to prevent charge accumulation during EBL. The pattern was written with a 30 keV electron beam using a dose of 210 $^{-4}$ C/cm^2 and then developed in a 1:3 solution of MIBK:IPA. One lens fabricated with this procedure is shown in Figure 2.5a, which had a 5 mm focal length and 1 mm diameter, and was able to diffract light to a 5 μm focal point with approximately 30% efficiency. This spot size is not drastically larger than a diffraction limited spot, and the efficiency is slightly lower than what could be theoretically achieved. The minimum feature size of this lens was 3.2 µm; the same work also reported fabricating a lens with a minimum feature size of 1 µm, but did not report on its efficiency.

Further work on EBL fabrication of PMMA lenses demonstrated that it was possible to reduce the minimum feature size of a lens down to less than a micron [66], allowing for lenses with shorter focal lengths and larger numerical apertures. This design was for an off-axis lens with an incident angle of 30° and numerical aperture of 0.5, which required approximately 1500 optical zones with features as small as 370 nm. Unlike the binary profile of the lenses in [65], this lens was corrugated in nature, owing to the manner in which the PMMA was removed during the development process, which in effect creates a blazed grating. A portion of this design is pictured in Figure 2.5b. When illuminated with 780 nm light, it was able to produce a 1.3 µm focal spot with approximately 20% efficiency.

Subsequent work has resulted in smaller lenses with smaller features, such as the EBL fabrication of a binary lens in PMMA with a 2 µm diameter and 20 nm minimum feature size [67]. However, the optical performance of this lens was not reported. Furthermore, the thickness of this lens was only 50 nm, which is far from the optimal feature depth dictated by Equation 2.4, and would likely need to be transferred into a hard mask to etch the pattern sufficiently deep into the substrate.

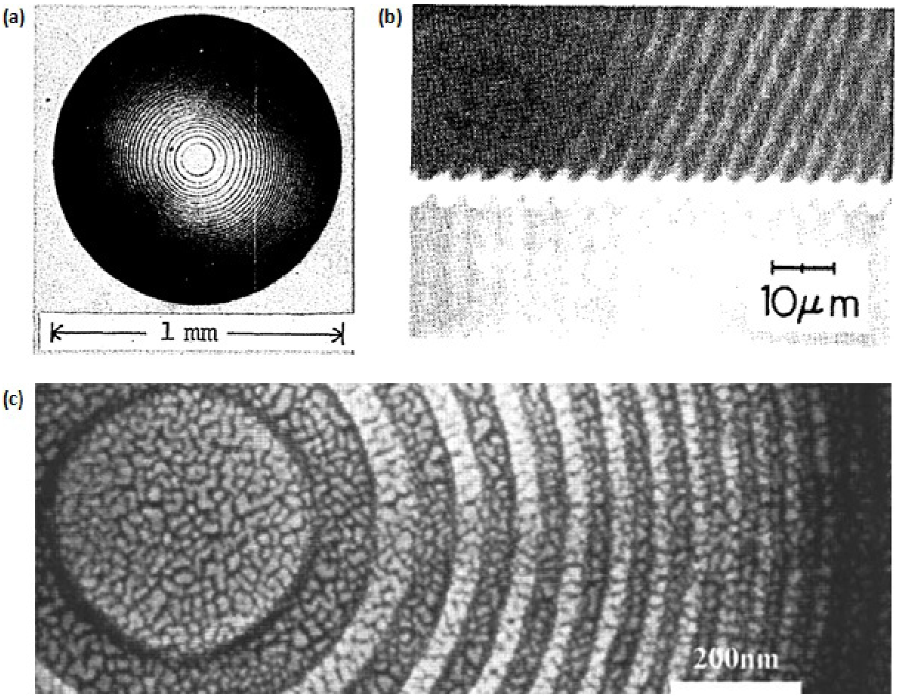

Figure 2.5: (a) Micrograph of a binary level lens written by EBL in PMMA. (Reproduced with permission from **[65]**.) **(b)** SEM image of an off-axis corrugated lens written in PMMA. (Reproduced with permission from **[66]**.) **(c)** SEM image of a binary level lens written in PMMA. The apparent texture is due to the grain size of the metal deposited for SEM imaging. (Reproduced with permission from **[67]**.)

As mentioned above, an important consideration when using EBL for tightly packed features is the proximity charging effect, whereby backscattered electrons alter the total dose received at any particular point. It has been demonstrated that by using a linear correction factor to the nominal EBL dose, it is possible to maintain the ideal 50% duty cycle across the features of a lens, even as the features become increasingly close together at the outermost zones, as demonstrated in Figure 2.5a [61]. This work was performed in hydrogen silsesquioxane (HSQ), which provides very high lateral resolution and also offers a refractive index comparable to that of glass [68]. The same work showed that it was also possible to pattern this resist using x-ray lithography after first using EBL to create a pattern in PMMA and then coating it with gold, which could serve as a mass-replication method for arrays of diffractive lenses. An array of these lenses is shown in Figure 2.5b. The lenses were designed to have a numerical aperture of 0.85, and were tested at a wavelength of 400 nm. Although their efficiency was not reported, the Gaussian skirt waist of their focal points was close to that predicted by simulations, approximately 570 nm.

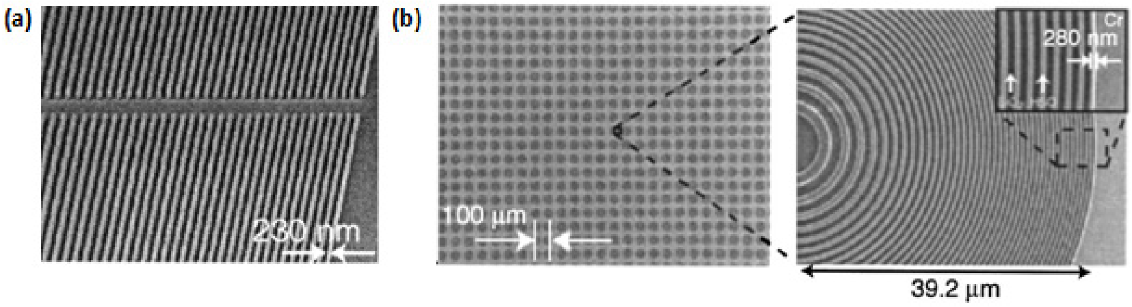

Figure 2.6: (a) Portions of cylindrical lenses with controlled line-widths using correction for the proximity effect with electron beam lithography, patterned in HSQ. **(b)** An array of binary lenses patterned in HSQ using x-ray lithography, and surrounded by chromium to prevent the transmission of unwanted light. (Reproduced with permission from [61].)

2.4.2 Etched-Substrate Lenses

Although using PMMA directly as the lens material is attractive due to its simplicity, it has limitations in regards to its durability, its feasibility for creating multi-level structures, and its suitability for use as a replica mould. As a more robust alternative, it is possible to etch EBL patterns into a substrate, which can involve first patterning a resist with EBL, developing this pattern and then using it as a mask when etching the substrate.

One such example is a blazed grating fabricated by EBL and then etched into silicon dioxide [69]. This process involved using a less common resist, X AR-N 7700/18, covered with a thin aluminium layer to prevent charge build-up on the substrate. Once developed, the pattern was then transferred into the silicon dioxide using reactive ion etching (RIE) with CHF_3, which etches the substrate approximately twice as fast as the resist. For a grating with a 4 µm period and 1.29 µm depth, the diffraction efficiency was 48.6%, compared by the rigorous theory prediction of 81.8% for a blazed grating.

Directly transferring the pattern from the resist to the substrate is comparatively simple; however, the etch selectivity between PMMA and substrates such as silicon is typically poor [70]. Therefore, the pattern is often first transferred into a “hard mask”. One implementation of the hard mask method used EBL with 50 nm PMMA, transferred the pattern into 20 nm of chromium underneath the PMMA using RIE, and then used the chromium pattern as a hard mask to transfer the pattern into the silicon substrate with RIE [71]. Interestingly, this approach used a low energy electron beam of just 2.5 keV, which was intentionally defocused prior to writing. Rather than the conventional approach of writing with a very tightly focused beam and using a number of adjacent passes of the beam to create wider lines, this approach wrote “wide” lines with a single pass of the defocused beam and controlled the line widths to a high degree of precision by adjusting the amount of defocus and the energy dose used. The diffractive optics had feature widths as small as 100 nm, with an etch depth of 1 µm, pictured in Figure 2.7. These patterns were designed as Bragg-Fresnel lenses for use with high energy photons in a synchrotron optics beam line, where they were reported to have an efficiency of approximately 26% [72].

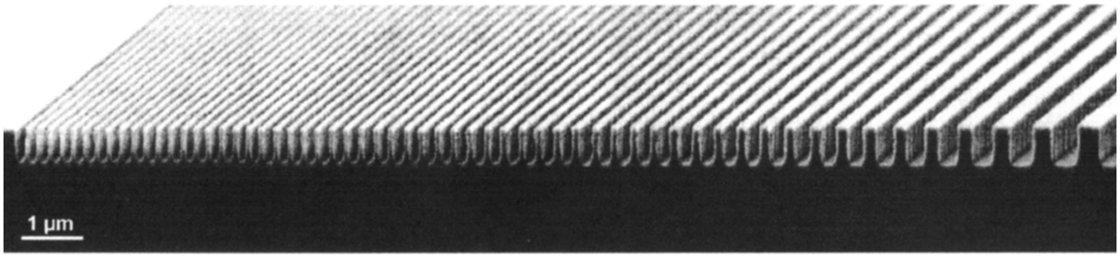

Figure 2.7: Cross section of a diffractive lens etched 1 µm into silicon, with line-widths determined by varying the defocus and dose of the electron beam when patterning PMMA. (Reproduced with permission from **[71]**.)

2.4.3 Multilevel Lenses from Binary Masks

In accordance with the theory discussed in Section 2.2, a diffractive lens with two discrete profile levels will have comparatively low diffraction efficiency, and therefore it is desirable to create a multilevel lens. One standard method involves using multiple iterations of a fabrication process to increase the number of discrete profile levels. Despite consisting of multiple levels, these designs are often termed "binary lenses" because of the binary nature of the masks used to create them. By using n binary masks, it is possible to create 2^n discrete steps [40]. This approach is attractive because it is fairly straightforward to extend a single iteration of a binary write technique such as EBL to multiple iterations. However, the primary drawback with this method is the necessity of accurate alignment of the patterns between subsequent steps.

One such process involved depositing a chromium layer followed by PMMA, EBL patterning and developing the PMMA, wet etching the chromium, and etching the substrate with RIE [73]. Three sequential repetitions of this process created eight-level lenses in both quartz and gallium arsenide. By using high-resolution alignment marks that were scanned by the electron beam prior to writing each repetition, it was possible to achieve alignment errors on the order of 50 nm. Several lenses were fabricated in this manner, with a few examples shown in Figure 2.8. Optical testing of the f/3 lens fabricated in quartz (with a minimum feature size of 500 nm) indicated a diffraction efficiency of 88%, which is not drastically less than that predicted by scalar theory.

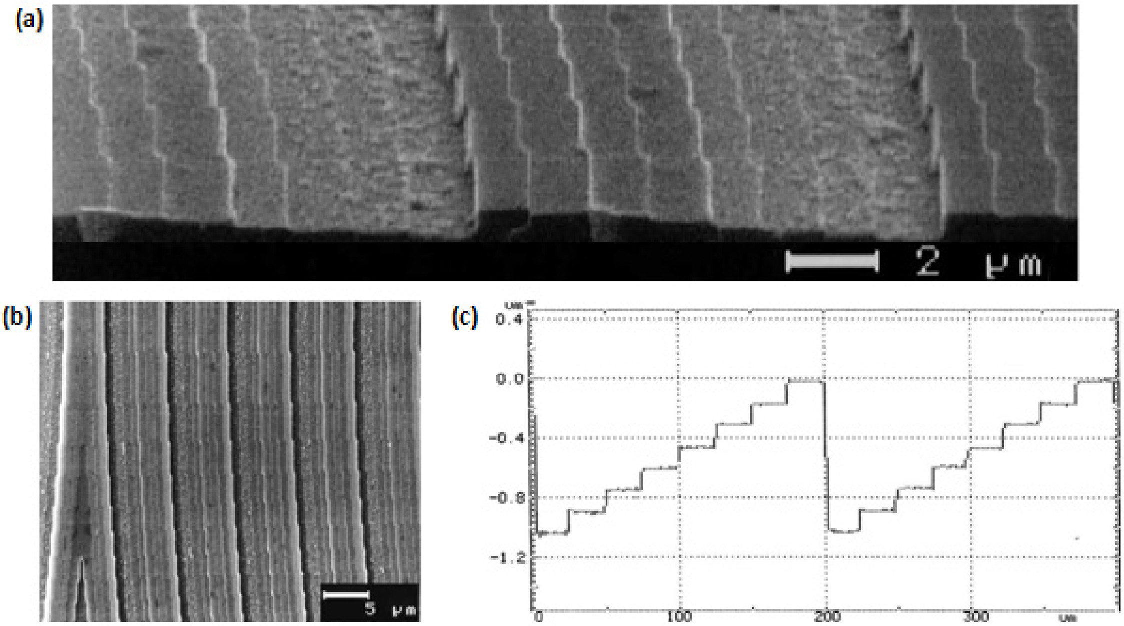

Figure 2.8: **(a)** Side view of two optical zones of an 8-level lens created in gallium arsenide. **(b)** Top view of the outermost zones of an 8-level lens in quartz. **(c)** Profilometer scan of a portion of the 8-level lens in quartz (although not the same section pictured in the top view). (Reproduced with permission from **[73]**.)

2.4.4 Alternative Multi Phase-Level Approaches

Owing to the difficulties associated with alignment between multiple patterning steps, alternative methods to create multi-level structures have been investigated. Grey-scale EBL is one “analogue write” method that has been proposed, whereby different exposure doses vary the amount of PMMA that is removed when developed [74]. With a writing voltage of 50 keV, this technique has been used to create a 6-level structure in PMMA, with features 20 nm deep and as small as 500 nm in width. These structures were then directly transferred into a silicon substrate by RIE with approximately a 1:1 etch ratio. This multi-level patterning technique was proposed as a method for creating diffractive optics, but it has not yet been demonstrated with optical results. And although it appears promising, there are some considerable limitations in attaining the micron-scale height that is typically required for diffractive optics. As mentioned above, PMMA does not typically provide a very robust mask for etching, meaning that the PMMA thickness would have to be comparable to the height of the desired structure. This limitation is problematic because increasing resist thickness typically implies a loss of feature resolution [75], owing to electron scattering in the material.

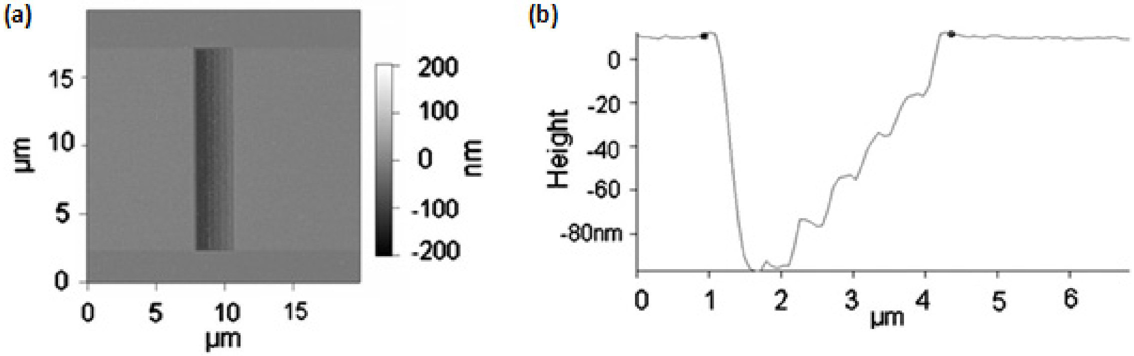

Figure 2.9: (a) Top view of a multi-level structure in silicon created by grey-scale lithography. **(b)** Atomic force microscope trace of the structure's height. (Reproduced with permission from **[74].**)

As an alternative to improving efficiency by using a multilevel structure, various designs have utilized a chirped or patterned structure to create an effective index of refraction, essentially allowing for multiple phase regions while only requiring a two-level surface relief profile. One such design created a circular lens with four effective phase regions [76], as illustrated in Figure 2.10a. Between the two extremes of completely exposed and completely unexposed levels of PMMA, the lens had two intermediate phase levels created with a 700 nm period: one with a 350 nm pillars and the other with 550 nm pillars. For fabrication, 100 nm of aluminium followed by 70 nm of PMMA was deposited onto the quartz substrate, and the pattern was written with EBL and then developed. The aluminium was dry etched using the PMMA as a mask, and then the quartz was dry etched using the aluminium as a hard mask. The lens was 1 mm in diameter and had a focal length of 2 cm. When optically tested at a wavelength of 633 nm, it was found to have an efficiency of 53%, in comparison with the 65% predicted by scalar theory. At the focal point the full width at half maximum was measured to be 15 µm, compared with the diffraction limited focal point of 15 µm for the Gaussian skirt width.

The same basic design principle was also used to create an effective refractive index using a series of concentric sub-wavelength rings [77], shown in Figure 2.10b, with a diameter of 36 µm and focal length of 65 µm. Its efficiency was not reported, but its measured Gaussian skirt width of 3 µm was approximately twice that of the expected diffraction limit.

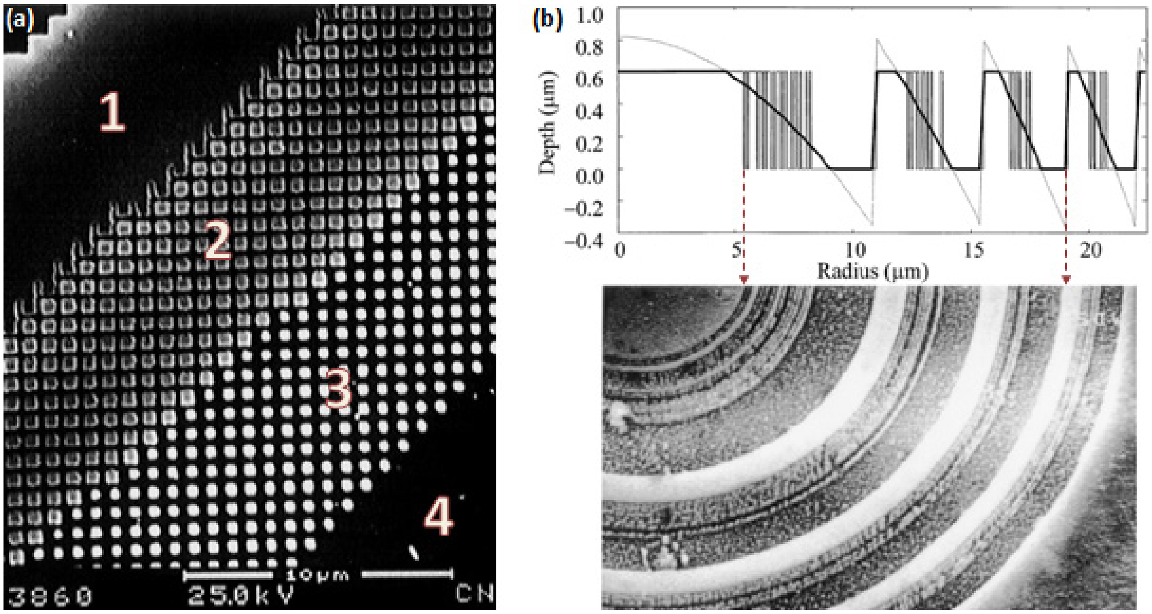

Figure 2.10: (a) A single optical zone with four regions of different effective refractive index, created by using different fill factors in a two-level profile. Regions 1 and 4 appear the same, but 1 is completely un-etched and 4 is completely etched. (Reproduced with permission from **[76]**.) **(b)** A portion of a lens created using chirped structures to create an effective refractive index. The top image shows an equivalent continuous profile lens (grey line), the effective phase-structure (thick black line), and the profile desired for fabrication (thin black line). (Reproduced with permission from **[77]**.)

2.4.5 Mass Replication

As discussed above, EBL is a useful tool for fabricating diffractive lenses because of the small feature sizes it is capable of attaining; however, it is not practical for fabricating a large number of devices. For mass fabrication, it is desirable to have a master pattern which can then be used multiple times as a stamp or mould in conjunction with a polymer [78]. This type of stamping replication is referred to as nanoimprint lithography [79, 80], which can also be used in a "step and repeat" configuration to pattern a larger area on a single polymer [81].

Nanoimprint lithography has been demonstrated as a replication tool for diffractive lenses, attaining features 200 nm tall and 80 nm wide, although optical performance was not reported [82]. Deeper structures are also possible, including a diffraction grating with a period of 800 nm and depth of 400 nm, with an estimated deviation error of 24 nm on the actual replicated linewidths [83].

Another soft lithography alternative to nanoimprint lithography is replica moulding, whereby a polymer is coated on top of the mould, cured, and then released [84]. A slightly more unusual replica moulding technique was used to create a chirped diffraction grating [85]. In this process the master mould was a diffraction grating with a uniform pitch made from an elastic material, which was compressed to varying degrees across its width during the moulding process, thus altering the pitch and producing a chirped grating.

2.5 Summary

The theory of diffractive lenses described above provides an introduction to the constraints involved for optimizing the geometry of a diffractive optical element. Although the design process of the diffractive lens was not a part of the work for this thesis, its basic considerations have been introduced to provide context for the existing lens design that will be presented in Chapter 3.

In terms of the physical realisation of the current design, a number of previously reported designs give important information with regards to the most feasible fabrication procedures and expected optical performance. These designs have demonstrated desirable qualities including small feature widths, accurate feature-width control, comparatively large aperture lenses, and multilevel structures. As will be presented in Chapter 4, this thesis project endeavours to develop and utilize a fabrication process that can integrate all of these desired attributes and that is compatible with the facilities available at McGill University.

3 : DESIGN SPECIFICATIONS

3.1 Introduction

The design of the sensor layout and the diffractive optics were previously completed by another student and thus were not inherently a part of this thesis project[1]. This chapter presents a brief summary of the previous work to provide the larger context of the design and to highlight the design constraints for the existing project.

3.2 Multi-Channel Design

The overall goal for the proposed SPR sensor project is to create a compact, multi-channel angular-based SPR sensor. Similar to a previously demonstrated device [31], light will be coupled to and from the sensing spots using diffractive optics rather than the more conventional prism-based method. The optics will be integrated with an electrowetting-on-dielectric microfluidic system similar to that described in [86], in order to provide precision and flexibility in transporting analytes to each sensor spot. This combined platform will be connected to an input light source at a wavelength of 850 nm, and to a CCD and to provide readout of the SPR signal. 850 nm is an appropriate choice of wavelength because while the angular sensitivity of SPR sensors improves with decreasing wavelength, the sharpness of the SPR dip improves with increasing wavelength [87]. At 850 nm the sensitivity of the system still provides a reasonable shift in angles with changing refractive index, while also providing an SPR dip with an easily identifiable centre point. Longer wavelengths are also advantageous for the design of the diffractive optics, since they allow for larger feature sizes. Additionally, operation at

---

[1] M. Imran Cheema, unpublished work carried out as part of Genome Canada / Genome Quebec project entitled '*Integrated Proteomics Platforms for High-Throughput Biomarker Discovery and Validation'.*

visible or near-visible wavelengths is preferable owing to the greater availability of reasonably priced high resolution cameras at these wavelengths.

Compared to the previous device [31], which was comprised of three sensing channels utilizing diffractive mirrors, the proposed SPR sensor design is further miniaturized and parallelized, incorporating 108 parallel sensing channels and using considerably smaller diffractive lenses rather than diffractive mirrors. The top view of the entire chip is illustrated in Figure 3.1a. Viewed from the side in Figure 3.1b, each channel consists of one cylindrical lens to focus light onto the sensing spot, thus providing a range of interrogation angles, and another to re-collimate light on its way to a CCD sensor.

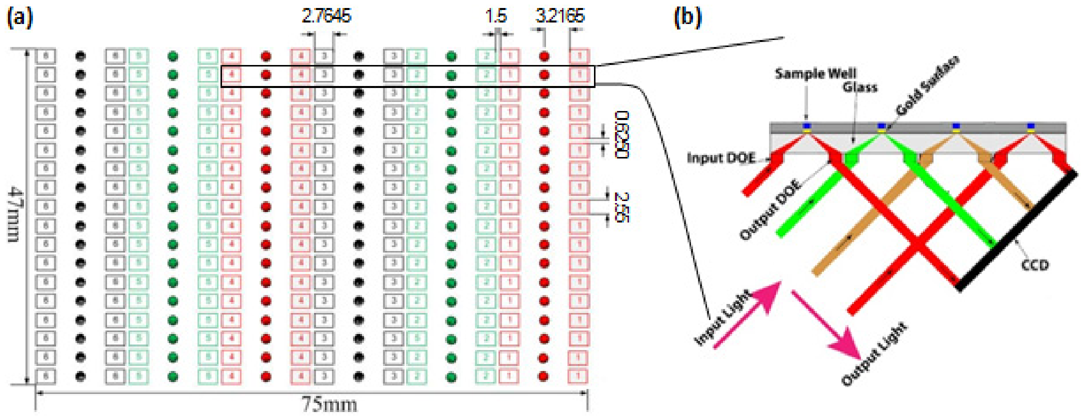

Figure 3.1: (a) Top view of the proposed multi-channel SPR sensor. All dimensions in millimetres. (Reproduced with permission from M. Imran Cheema.) **(b)** Side view of four sensing channels coupling light to and from the sensing spots. (Reproduced with permission from Andrew G. Kirk.)

The overall layout of the diffractive lenses required several design considerations. One major concern was the positioning of the optics such that the 0th order light would not be coincident on any sensing spots or at signal locations on the CCD output. Another consideration was cross-talk between sensing channels, which required adjacent pairs of lenses to be placed sufficiently far apart so that diffraction from each lens aperture in the non-focusing axis would not impact neighbouring channels.

3.3 Individual Lens Profile

3.3.1 Lens Requirements

Illumination of each sample spot is provided from the back side of the optically transparent chip as illustrated in Figure 3.1b. The thickness of the chip determines the required focal length of the lens, and the range of angles appropriate for angular-based SPR measurements determines the width of the lens. Table 3.1 provides a summary of the requirements for each individual lens, and Figure 3.2 provides a diagram of the lens geometry.

Table 3.1: Summary of requirements for a single lens.

Parameter	**Value**
wavelength	850 nm
substrate index of refraction	1.5
incident angle	45°
focal length	1.5 mm
diffracted angles	65° - 75°
starting distance from optical axis	3.2165 mm
end distance from optical axis	5.9810 mm
lens width (focusing axis)	2.7645 mm
lens height (non-focusing axis)	2.55 mm

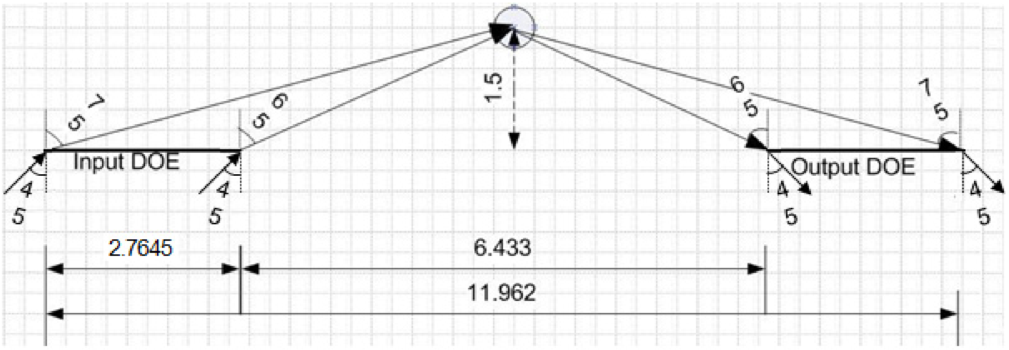

Figure 3.2: Positional and angular specifications for two lenses in a single sensing channel. All lengths are in millimetres; all angles are in degrees. (Modified reproduction with permission from M. Imran Cheema.)

3.3.2 Optical Zone Boundaries

As discussed in the previous chapters, a cylindrical diffractive lens is essentially comprised of a series of lines of decreasing width, and can be thought of as a grating with a period that varies across the lens. The grating equation of Equation 2.2 was used to determine the local feature pitches across the width of the lens, starting at a position 3.2165 mm from the optical axis with a diffracted angle of 65°. The first optical zone at 3.2165 mm requires a pitch of 1.353 μm, meaning that the second optical zone should begin at 3.2179 mm. Equation 2.1 indicates the angle required for the second optical zone, which can then be used in the grating equation of Equation 2.2 to calculate the pitch of the second optical zone. This process can be repeated in a stepwise method across the entirety of the design, as plotted in Figure 3.3.

However, during the original design process, Equation 2.2 was used to calculate the period for the first and last optical zones, and then it was incorrectly assumed that the period would vary linearly between these two extremes, also shown in Figure 3.3. The software pattern discussed below was also incorrectly based upon this linear profile, and accordingly the fabricated device presented in Chapter 5 displays this trend. Unfortunately, the discrepancy between these two design methods was not realized until after the current device had been fabricated, and time constraints prevented the fabrication of another device with the correct profile. As will be discussed in Chapter 5, the difference between the ideal hyperbolic profile and the fabricated linear profile means the wave-fronts are not shaped exactly as would be required for optimal focusing, and thus some aberrations should be expected in the focal properties of the lens.

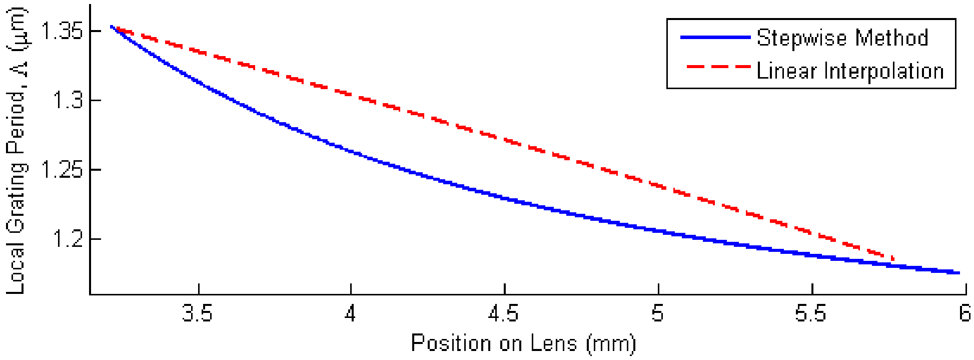

Figure 3.3: Determination of the local grating period of the design based upon Equation 2.2. The left-most edge of the graph corresponds to the left-most edge of the output lens shown in Figure 3.2.

3.3.3 Feature Heights

As a compromise to ensure both reasonable diffraction efficiency and fabrication feasibility, it was determined that the diffractive lenses should be designed as 4-level devices. Optimal depths for an *N* level device were given by Equation 2.4 which for a 4 level device with refractive index of 1.5 at a wavelength of 850 nm requires step sizes of 0, 425, 850, and 1275 nm. Figure 3.4 shows a side-view of the first and last optical zones of the device, illustrating their lateral and vertical dimensions.

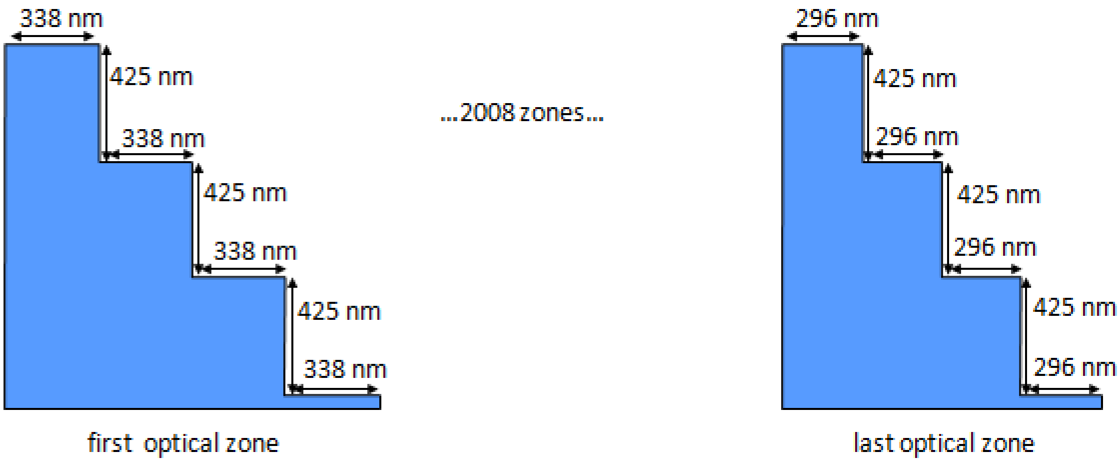

Figure 3.4: Side-view of the two extreme optical zones in the design.

3.4 Simplified Design

For this master's project, a four-level lens was not yet realized, but the fabrication process was sufficiently developed to create a two-level lens. Accordingly, all features were twice as wide as they would have been for a four-level design. Additionally, owing to fabrication logistics discussed in Chapter 4, an entire lens was not created, but a smaller section of the lens was fabricated for demonstration purposes. The width of the fabricated lens was approximately 1.2 mm, which is a significant portion of the entire width. The section of lens selected for fabrication began with the largest features and then extended outwards away from the optical axis. In the non-focusing axis the device was 100 μm across, as dictated by the size of a single EBL write-field, which is much smaller than the entire design but sufficient for demonstrating optical characteristics.

As will be discussed in Chapter 4, the lens must be written using several smaller EBL write-fields. Although the EBL patterning software has the capabilities to automatically fracture one large pattern into several appropriately-sized sections, this sectioning was done prior to inputting the pattern into the EBL software in order to add a few important reference marks on each field. Firstly, numbers were inserted near the top of each field for reference purposes during characterization. Secondly, extensions to the main length of the lines were included at five evenly spaced points across the width of each field to provide known locations for measuring the width of the lines during subsequent imaging sessions. Fracturing was performed such that lines were always written within a single write-field rather than having portions of their width written in two separate fields. Dump-points for the electron beam were located at the corners of each field to allow the pattern to be written without the use of a beam-blanker. The pattern for a single EBL write-field is illustrated in Figure 3.5.

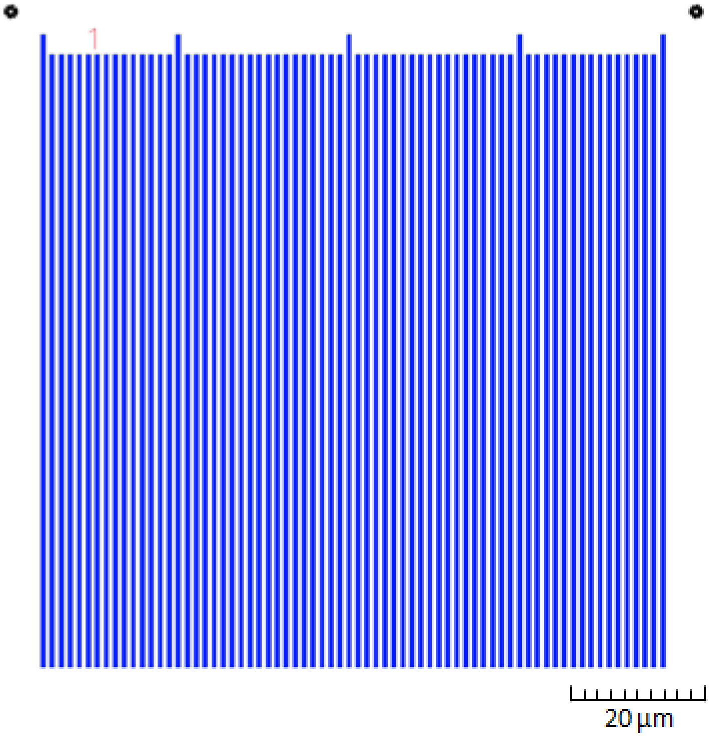

Figure 3.5: The layout for a single EBL write-field for the simplified lens design. The lines and spaces form a 50% duty cycle, although it may appear somewhat larger in the image. The field number label is illustrated in red; the dump-points for the electron beam are marked in black.

3.5 Summary

This chapter has presented the design constraints for the long-term goal of a multi-channel SPR sensing device, as well as the simplified design profile that has been fabricated and tested in the current thesis project. The development of the fabrication process for this simplified device will be presented in Chapter 4, followed by fabrication and optical results in Chapter 5.

4 : FABRICATION PROCESS DEVELOPMENT

4.1 Introduction

As discussed in Chapter 2, diffractive lenses have been created using a number of microfabrication techniques. For this project, the basic premise was to write the pattern using EBL, transfer the pattern to a hard mask, etch the pattern into the substrate, and then replicate the substrate pattern in an optical polymer.

Owing to the comparatively large area of the lenses of the design presented in Chapter 3 and the small features they contain, there were a few main issues to be resolved for their fabrication. This chapter presents a step-by-step recipe of the fabrication process that was used, a description of the problem of field stitching in EBL and an explanation of the methods used to tackle these issues, a calibration method for ensuring accurate control of feature widths, and a list of further fabrication improvements that will be necessary to complete the full design.

4.2 Process Flow

When developing the process flow for diffractive lenses, EBL was an appropriate choice for patterning because the lens design includes features on the order of 300 nm. Another significant design constraint was the required feature heights, which implied that a hard mask would be necessary to etch features sufficiently deep into the substrate.

With the facilities available at McGill, two options were seen as feasible for the creation of a hard mask via EBL. The first option was to deposit a thin layer of chromium under the PMMA layer, pattern and develop the PMMA, and then etch the chromium with RIE. Wet-etching of the chromium would have been unsuitable owing to the undercutting that would occur. The second option was to use a dual layer of PMMA and EL 6 copolymer, pattern and develop these layers, and then perform a liftoff process with chromium. As dry-etching recipes are often difficult to optimize [88], and as the McGill facilities have some experience with liftoff processes, the latter was chosen as the patterning method for this project.

The overall process flow is shown in Figure 4.1, comprising of two repetitions of essentially the same process with a few minor modifications. The parameters for each process step are described in detail below in Table 4.1. Additional technical details on EBL procedures used in this process are provided in an appendix at the end of this document.

Figure 4.1 shows the intended process flow for the fabrication of the final device, but for this thesis, a four-level profile was not yet realized. Instead, a single repetition of the process flow produced a two-level profile. Furthermore, the pattern has not yet been transferred into the optical polymer, and therefore the etch depth of the pattern was altered to allow for reflective testing on the silicon master. The exact process flow described below is that followed for the tested device; however, with a few minor modifications it would be capable of producing the four-level device, as described in Section 4.2.1.

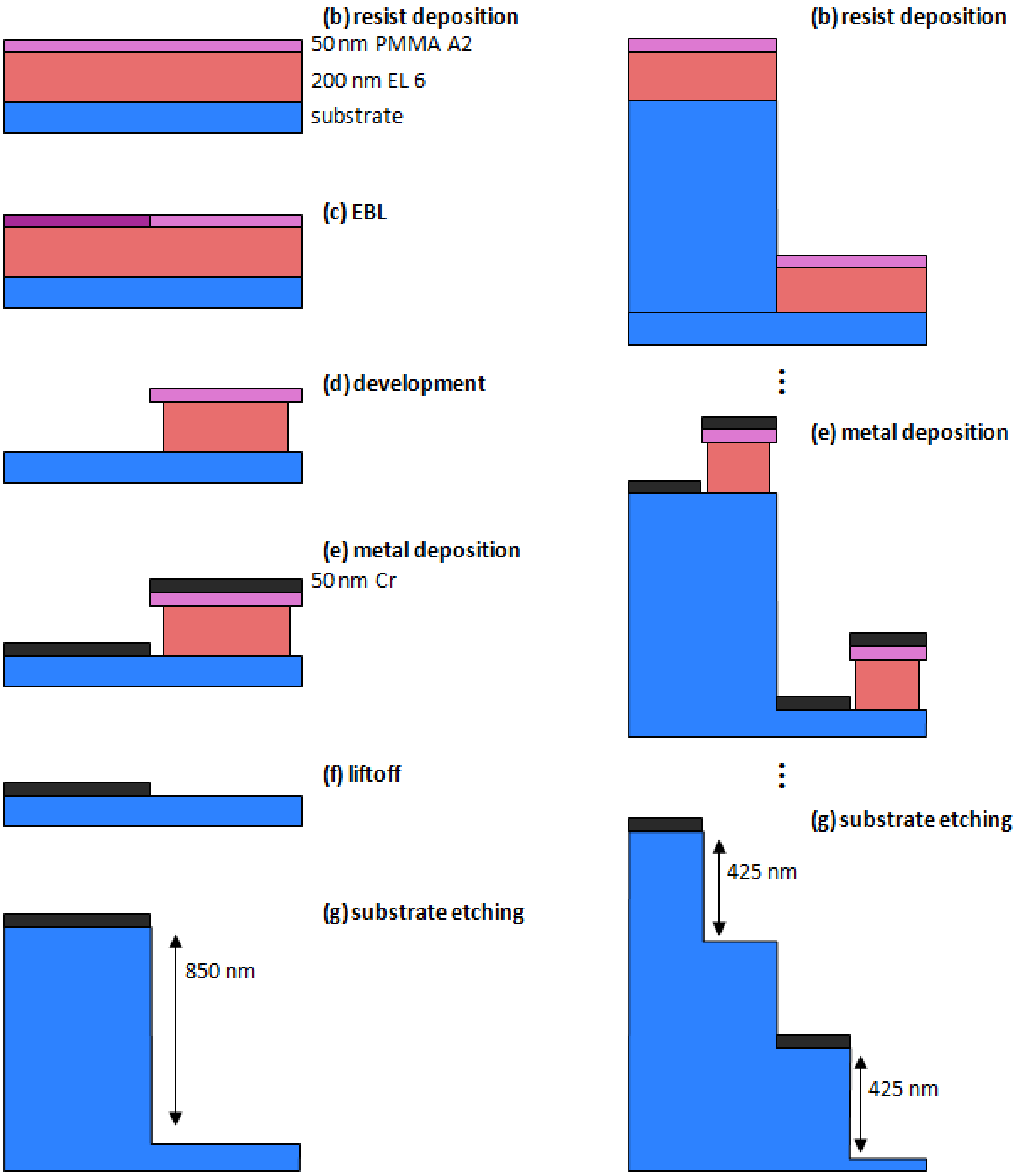

Figure 4.1: Fabrication process flow for two complete iterations to create a four-level profile in a silicon master. Steps are labelled in accordance with the lettering provided in Table 4.1. The chromium mask is removed before starting the second iteration of the process. The illustration of the second iteration omits the EBL, development, and liftoff stages, but they are to be performed exactly the same as in the first iteration.

Table 4.1: Process flow description.

<table>
<tr><th>Process Step</th><th>Description</th></tr>
<tr><td>(a) Cleaning</td><td>The sample was immersed in an acetone bath at 30°C and ultrasonically agitated for 10 minutes, and then immersed in an isopropyl alcohol (IPA) bath at 30°C and ultrasonically agitated for a further 10 minutes. The sample was dried with nitrogen gas, and then baked on a hotplate at 150°C for 3 minutes to ensure complete dehydration.</td></tr>
<tr><td>(b) Resist Deposition</td><td>For the first iteration of this process, PMMA and EL 6 were deposited using a standard spin-on technique as described in the tables below. For the second iteration of the process, an alternative method will be required, as discussed in Section 4.2.1.</td></tr>
<tr><td>EL 6</td><td>200 nm of EL 6 copolymer was spin-coated with a Laurell Spin Coater using the following steps:
<table>
<tr><th>Speed</th><th>Acceleration</th><th>Time</th></tr>
<tr><td>500 rpm</td><td>1305 rpm/s</td><td>5 s</td></tr>
<tr><td>2000 rpm</td><td>1305 rpm/s</td><td>45 s</td></tr>
<tr><td>0 rpm</td><td>1305 rpm/s</td><td>5 s</td></tr>
</table>
The sample was soft-baked on a hotplate at 150°C for 60 seconds.</td></tr>
<tr><td>PMMA</td><td>50 nm of PMMA A2 resist was spin-coated with the Laurell Spin Coater using the following steps:
<table>
<tr><th>Speed</th><th>Acceleration</th><th>Time</th></tr>
<tr><td>500 rpm</td><td>1305 rpm/s</td><td>5 s</td></tr>
<tr><td>4000 rpm</td><td>1305 rpm/s</td><td>45 s</td></tr>
<tr><td>0 rpm</td><td>1305 rpm/s</td><td>5 s</td></tr>
</table>
The sample was soft-baked on a hotplate at 150°C for 60 seconds.</td></tr>
</table>

(**Table 4.1** continued)

<table>
<tr><td>(c) Lithography</td><td>EBL was used to pattern the sample, using a Hitatchi SU-70 microscope custom-fitted for lithography purposes. The details of the alignment procedure used prior to exposure are discussed in Section 4.3. Exposure was then performed with the parameters following parameters:
<table>
<tr><th>Parameter</th><th>Value</th></tr>
<tr><td>Accelerating Voltage</td><td>20 kV</td></tr>
<tr><td>PCD Current</td><td>13.2 pA</td></tr>
<tr><td>Working Distance</td><td>6.6 mm</td></tr>
<tr><td>Exposure Dose</td><td>217 μC/cm^2</td></tr>
</table></td></tr>
<tr><td>(d) Pattern Development</td><td>As listed in the sub-steps below, the exposed PMMA was removed using a standard development recipe, and then any remaining residue was removed with a dry etch process.</td></tr>
<tr><td>Development</td><td>The pattern was developed using a 1:3 mixture of MIBK to IPA. The sample was immersed in the mixture for 30 seconds with gentle agitation, then dried with nitrogen gas, rinsed with IPA, rinsed with de-ionized water, and dried with nitrogen gas.</td></tr>
<tr><td>Asher</td><td>To remove any polymer residue that could prevent proper adhesion of chromium to the substrate, the sample was treated in the PVA TePla Oxygen Asher with the following parameters:
<table>
<tr><th>Parameter</th><th>Value</th></tr>
<tr><td>Pressure</td><td>1.00 mBar</td></tr>
<tr><td>Power</td><td>60 W</td></tr>
<tr><td>Time</td><td>20 s</td></tr>
</table></td></tr>
</table>

(**Table 4.1** continued)

<table>
<tr>
<td>(e) Chromium Deposition</td>
<td>50 nm of chromium was deposited using electron beam deposition in the Temescal BJD 1800 Evaporator with the following parameters:
<table>
<tr><th>Parameter</th><th>Value</th></tr>
<tr><td>Deposition Rate</td><td>0.1-0.2 nm/s</td></tr>
<tr><td>Power</td><td>8-10%</td></tr>
<tr><td>Emission Current</td><td>50-60 mA</td></tr>
</table>
Chromium is more volatile than most materials used in the electron beam evaporator, and if deposited too aggressively can cause sudden increases in the chamber pressure. Therefore, this deposition was not performed with an automated recipe; instead, the beam power was controlled manually.</td>
</tr>
<tr>
<td>(f) Liftoff</td>
<td>The sample was immersed in Nano™ Remover PG (an N-Methylpyrrolidone based stripper) at 62° for approximately 4 hours to remove the remaining polymer from the surface, leaving behind only the chromium deposited directly on the substrate surface. At the end of the immersion, the sample was ultrasonically agitated at low power for 30 s to help remove any small pieces of polymer that may have been stuck between the pattern lines.</td>
</tr>
<tr>
<td>(g) Etching</td>
<td>The sample was dry-etched to a depth of 198 nm using magnetic enhanced reactive ion etching (RIE) in the Applied Materials Precision 5000 tool with the following recipe:
Stabilization:
<table>
<tr><th>Parameter</th><th>Value</th></tr>
<tr><td>Pressure</td><td>20 mTorr</td></tr>
<tr><td>Power</td><td>0</td></tr>
<tr><td>Magnetic Field</td><td>0</td></tr>
<tr><td>Gas Flow</td><td>CF_4: 30sccm</td></tr>
<tr><td>Time</td><td>15 s</td></tr>
</table>
</td>
</tr>
</table>

(**Table 4.1** continued)

<table>
<tr>
<td>(g) Etching
(continued)</td>
<td>
Breakthrough:
<table>
<tr><th>Parameter</th><th>Value</th></tr>
<tr><td>Pressure</td><td>20 mTorr</td></tr>
<tr><td>Power</td><td>400 W</td></tr>
<tr><td>Magnetic Field</td><td>75 G</td></tr>
<tr><td>Gas Flow</td><td>CF_4: 30sccm</td></tr>
<tr><td>Time</td><td>10 s</td></tr>
</table>
Stabilization:
<table>
<tr><th>Parameter</th><th>Value</th></tr>
<tr><td>Pressure</td><td>100 mTorr</td></tr>
<tr><td>Power</td><td>0</td></tr>
<tr><td>Magnetic Field</td><td>0</td></tr>
<tr><td>Gas Flow</td><td>Cl_2: 30sccm
HBr: 15 sccm</td></tr>
<tr><td>Time</td><td>20 s</td></tr>
</table>
Main Etch:
<table>
<tr><th>Parameter</th><th>Value</th></tr>
<tr><td>Pressure</td><td>100 mTorr</td></tr>
<tr><td>Power</td><td>300 W</td></tr>
<tr><td>Magnetic Field</td><td>75 G</td></tr>
<tr><td>Gas Flow</td><td>Cl_2: 30sccm
HBr: 15 sccm</td></tr>
<tr><td>Time</td><td>21 s</td></tr>
</table>
Pump-out:
<table>
<tr><th>Parameter</th><th>Value</th></tr>
<tr><td>Pressure</td><td>throttle open</td></tr>
<tr><td>Power</td><td>0</td></tr>
<tr><td>Magnetic Field</td><td>0</td></tr>
<tr><td>Gas Flow</td><td>-</td></tr>
<tr><td>Time</td><td>15 s</td></tr>
</table>
</td>
</tr>
</table>

(**Table 4.1** continued)

(h) Chromium Removal	The sample was immersed for 5 minutes in Transene chromium etchant 1020, which etches at an approximate rate of 4 nm/s. The sample was then rinsed with de-ionized water.

4.2.1 Process Notes

4.2.1.1 Resist Coating

As illustrated in Figure 4.1, the resist layers are considerably thinner than the features etched into the substrate in the first iteration of the process. Therefore, it is not possible to deposit the resists using a standard spin-on procedure for the second iteration. Although not yet demonstrated, it will instead be necessary to use a spray-coating method. McGill's fabrication facilities have previously used a spray-coater to deposit PMMA, but it has not yet been tested for EL 6. Investigation into this technique will be necessary when further developing the fabrication process.

4.2.1.2 Etch Depths

In the process flow described above, the pattern was etched 174 nm into the substrate, as estimated using a cross-section of the sample. The desired depth was 212.5 nm, which would provide the required half-wavelength phase shift when testing the lens in a reflective configuration for a wavelength of 850 nm. However, for a 4-level transmissive lens replicated in a polymer with refractive index of 1.5, the required etch depths will be 850 nm for the first etch and 425 nm for the second etch.

Although not yet fully optimized, it has been demonstrated that the required etch depth should be possible with the current recipe. Figure 4.2 shows a cross-sectional profile image taken with a scanning electron microscope (SEM) from a sample that had been etched for 189 s with the recipe described above, but on a different sample holder, which dramatically altered the etch-depth calibration. Profilometer measurements before and after removal of the chromium mask suggest that approximately 15 nm of the chromium mask was removed during RIE, indicating that the mask would be sufficient for a slightly deeper etch. However, near the bottom of the trench the etch profile significantly deviates from the ideal vertical walls, indicating that the exact gas composition in the recipe requires improvement, since different power, flow rates, and gas chemistries are all reported as factors affecting the etching profile [89, 90].

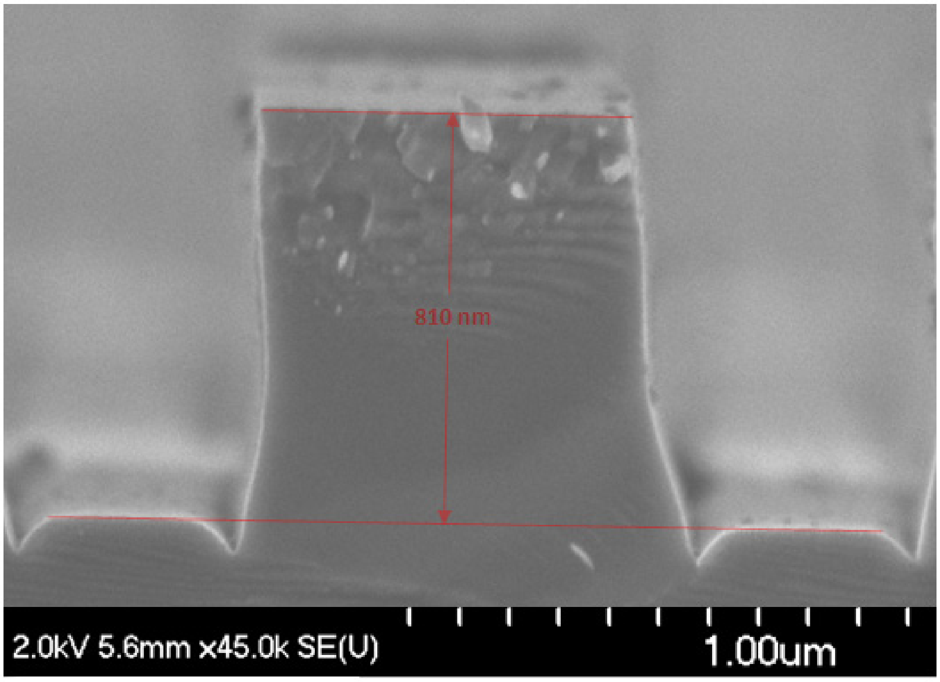

Figure 4.2: SEM image of a cross section of silicon etched approximately 810 nm with RIE.

4.3 Electron Beam Field Stitching

In order to pattern the total area required for the designed lens, patterning over multiple fields of the EBL system was necessary. A major portion of this thesis work involved developing a procedure to precisely and consistently achieve pattern stitching between adjacent fields. Software control of the system was performed using the Nanometer Pattern Generation System (NPGS), which accepts design files created in DesignCAD Express, and interfaces with the system's Hitachi SU-70 electron beam microscope and Deben SEM laser stage. Since this portion of the project only required evaluation of the EBL system, patterns were written in PMMA on silicon (with no EL 6 copolymer), developed, and then evaluated based on the patterns directly in the PMMA rather than using the full liftoff procedure described in Section 4.2.

4.3.1 Description of the Stitching Problem

As discussed in Chapter 2, EBL transfers patterns defined in software into an electron sensitive resist by tracing out the patterns with a high energy electron beam through the use of electromagnetic deflection coils. The extent to which the electron beam can be deflected defines the size of the lithography system's write-field. The further the sample is located from the electron beam tip, the larger the write-field will be. However, the trade off is that an increased working distance results in a loss of minimum feature resolution. For the Hitatchi SU-70 system, a working distance of approximately 6 mm has typically been deemed necessary to achieve features on the order of 300 nm, although it is possible that this value could be increased. At a working distance of 6.6 mm, the corresponding field size is 105 by 105 μm. However, to minimize possible aberrations occurring at the very edge of the deflection range, the field size that is actually used should be slightly reduced, in this case to 92 by 92 μm.

To meet design specifications, each diffractive lens must be 2.76 by 2.55 mm, which is many times larger than the size of a single write-field. Consequentially, it is necessary to stitch together multiple fields to produce the entire pattern. Stitching is performed by writing a single field, then moving the stage holding the sample to each subsequent position and writing the next field.

Particularly in the focusing axis, it is important to have very precise stitching control. The optical zones in this design are on average 1.2 μm wide, meaning that in a binary-level device, feature sizes are on the order of 600 nm. Therefore, if the positioning between two adjacent fields is off by 600 nm, the contributions from zones in the first and second fields will interfere at the desired focal point deconstructively. To a lesser degree, smaller misalignments will also negatively impact the lens' efficiency. In a four-level device, the tolerances will be correspondingly smaller.

In brief, accurate stitching requires two major components: high precision control of the sample stage, and high precision rotational alignment of the sample, stage, and field axes. The control of these two aspects is discussed in detail in the following sections.

4.3.2 Control of Stage Position

The EBL system uses a Deben SEM laser stage, motorized with a Sprite stage-controller and interfaced with a computer via RS-232. This stage includes piezoelectric actuators to control its fine-scale motion. To ensure the stage does not drift during the course of writing a single field, it is possible to keep the piezoelectric actuators enabled while the EBL system is writing.

The stability of these actuators was tested in order to determine when the NPGS program should ignore any remaining positioning error and consider the stage stationary in order to begin writing a pattern. Position data from the stage controller can be read by querying the controller through HyperTerminal as described in the Deben stage manual. Figure 4.3 shows the stability of the stage's position along the x-axis for five separate trials, where the stage was moved 100 μm in the x-direction for each trial. After some initial “false” settling points, the stage ultimately settles to a point no more than 10 nm away from the desired position, with jitter of no more than 20 nm from this steady state. These values could be off by a further 5 nm, since the precision of the values read from the stage are rounded to the nearest 10 nm. It is also worth noting that for the same trials, the position of the stage along the y-axis always displayed zero error, despite the fact that the stage does also move and recoil along this axis. Although not shown, similar results were obtained for movement in the y-axis.

These results indicate that the contribution of alignment error caused by the stage position should be minimal, and as will be seen in the following section, accurate alignment is dominated by rotational considerations.

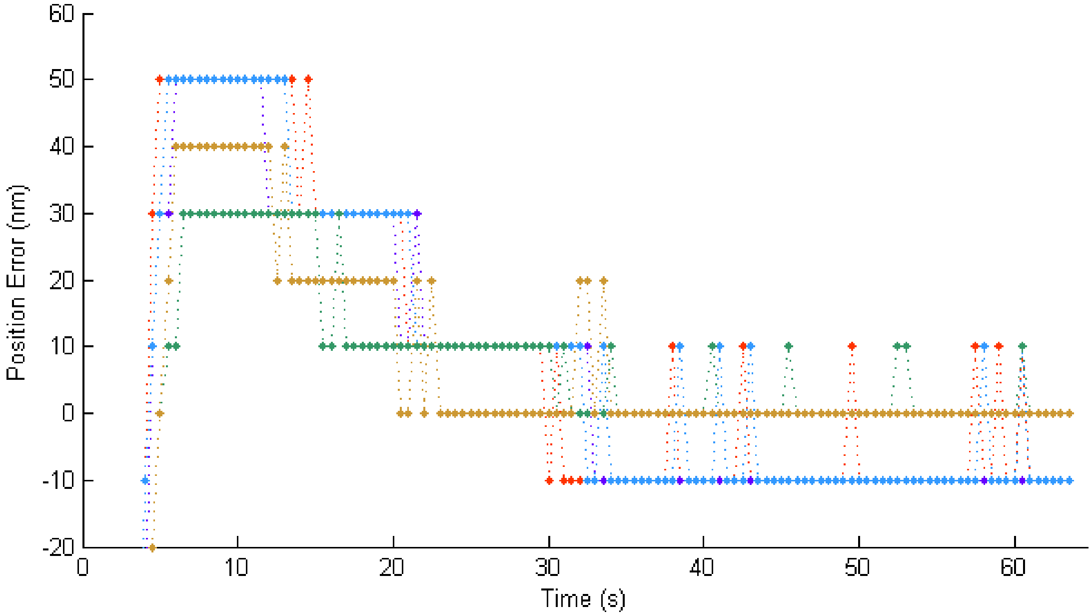

Figure 4.3: Positioning error of the x-axis of the stage for five different trials, each moving the stage 100 µm in the x-direction.

4.3.3 Control of Rotation Alignment

As illustrated in Figure 4.4, the stitching problem has three distinct sets of axes: the sample axes, the stage axes, and the field axes. Although the lithography system is installed such that the field and stage axes are relatively closely aligned, by default they are not perfectly concurrent. Furthermore, although the sample can be placed onto the stage such that the stage and sample axes are relatively close to each other, they will not inherently be perfectly aligned. Therefore, when patterning a sample that already has features on it, it is necessary to align all three sets of axes; and when patterning a sample with no existing features, it is necessary to align the stage and field axes.

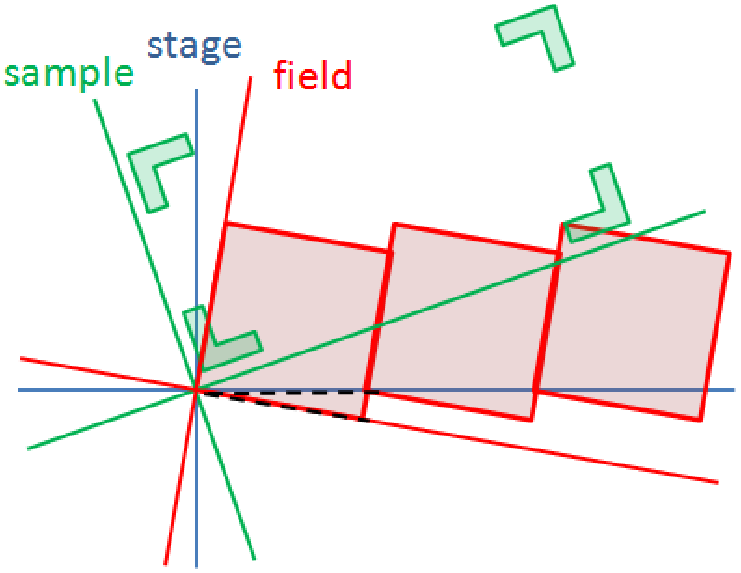

Figure 4.4: Illustration of the three sets of axes that must be aligned for field stitching. If no patterns are already present on the sample, only the stage and field axes need to be aligned to each other. Black dashes indicate the angle between the stage and field axes.

4.3.3.1 Alignment Mark Method

In principle it should be possible to pattern alignment marks on the sample with optical lithography, use the sample axes as the reference axes, and align the remaining two sets of axes to the reference. To align the field and sample axes, the Hitatchi SU-70 has a parameter referred to as “raster rotation”, which adjusts the angle of the microscope field. By viewing the alignment marks with the microscope, the raster rotation angle can be adjusted until the reference marks appear aligned with the microscope field. To align the stage and sample axes, the NPGS control system includes a rotational matrix routine. This procedure involves viewing the sample through the microscope and positioning the stage at three known positions on the sample. NPGS collects data on these stage positions, and then applies a rotation transformation to subsequent movement commands such that the stage moves parallel to the axes defined on the sample.

This alignment method was tested by writing two separate fields, each with 500 nm lines and 500 nm gaps across the entirety of the field, which ideally should align perfectly at the boundaries. Initial results did not prove satisfactory for high accuracy field stitching, as illustrated by the preliminary results in Figure 4.5. However, optimization of this process should be possible with a more complete understanding of the system; so in order to simplify the parameters under consideration, a closer investigation of the system began with the stage-field characterization discussed below. Based on the knowledge obtained from this characterization, it should in future be possible to improve stitching with an alignment mark method.

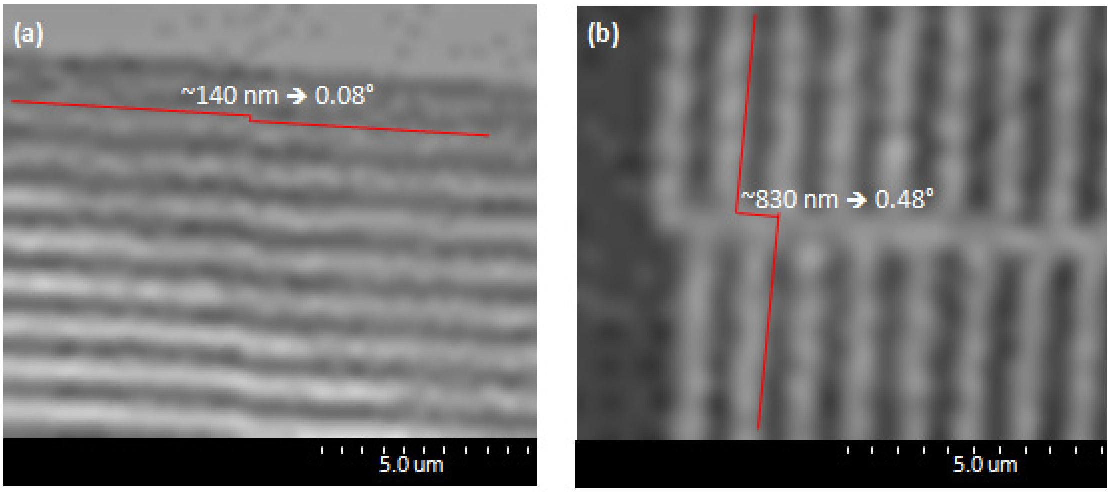

Figure 4.5: SEM images of preliminary results for stitching along **(a)** the x-axis and **(b)** the y-axis, obtained with the alignment mark method. The poor image quality is due to imaging at low magnification to see the entire write-field area,

and then cropping the image to a small portion of its original size. Despite the low quality of the image, it is possible to see a certain amount of misalignment in the x-axis and a greater amount in the y-axis. (50 nm PMMA on Si.)

4.3.3.2 Stage-Field Characterization Method

To address the problems observed in the alignment mark method, it was necessary to better understand the characteristics of the various sets of axes within the system, first by characterizing the relationship between the stage and field axes. The first step in this characterization was done without considering the orientation of the sample. As such, no alignment marks were used to calculate a rotation transformation for the stage, and so the stage moved along its default axes. With no raster rotation applied to adjust the angle between the stage and the field, adjacent fields were poorly stitched with a rotational error of approximately 0.43°, as shown in Figure 4.6.

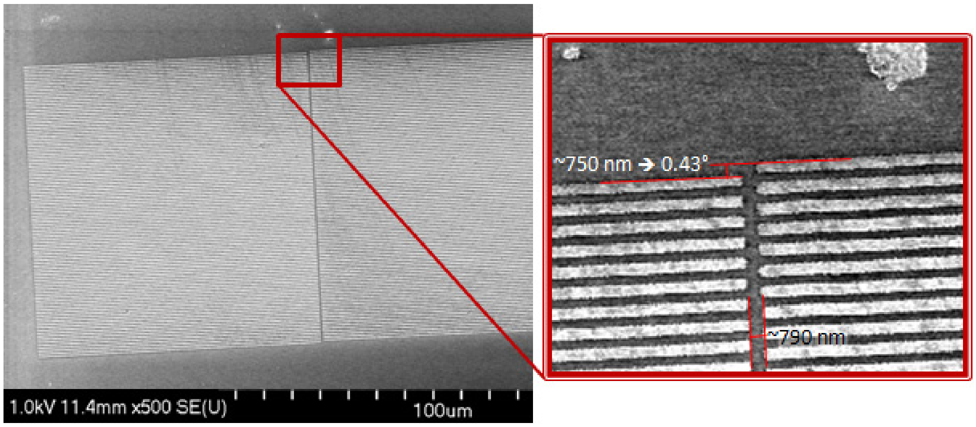

Figure 4.6: SEM image of poor field stitching when no raster rotation correction was applied. (50 nm PMMA on Si.)

Referring back to Figure 4.4, it can be seen that the angle formed between corners on adjacent written fields is equal to the angle between the stage and the field. By applying this angle as a raster rotation in a subsequent lithography session, it was possible to correctly align the stage and field axes. The gap seen in Figure 4.6 was also corrected for by decreasing the MAGscale value to 94240. (Details related to the MAGscale parameter are provided in

Appendix A.2.) As shown in Figure 4.7, the stitching between adjacent zones was nearly flawless, with only a slight bump visible where the resist received a double exposure.

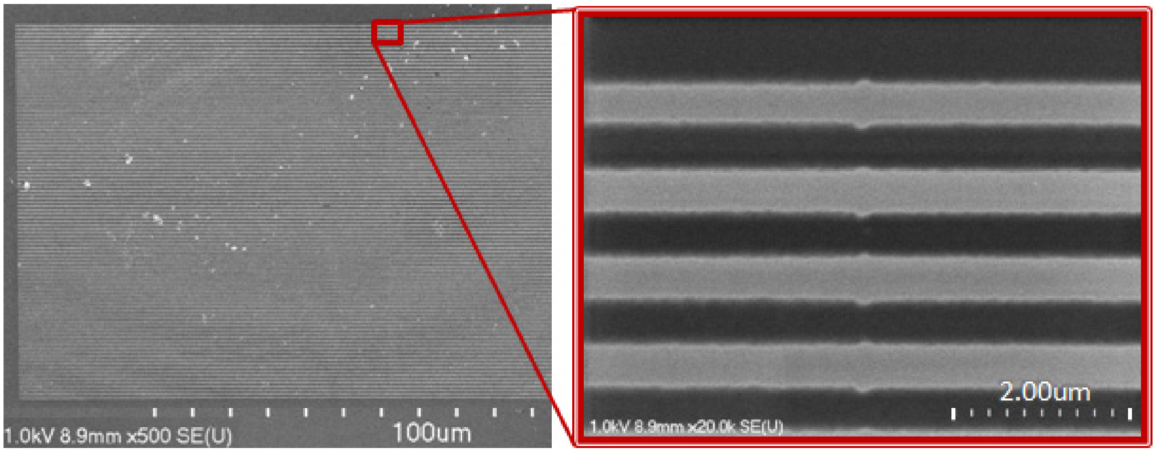

Figure 4.7: SEM image of corrected field stitching using a raster rotation angle of -0.3°, and a MAGscale of 94240. (50 nm PMMA on Si.)

Unfortunately, this characterization method currently suffers from some repeatability issues. As shown in Figure 4.8, the same raster rotation correction was applied in three separate lithography sessions. Although initially near-flawless, the alignment became progressively worse in subsequent sessions. The second test was arguably a result of the fact that the microscope system only offers 0.1° of control of the raster rotation parameter, but the third test appeared to be outside this range. The deflection of the electron beam is controlled by electro-magnetic coils, and it is expected that there are some hysteresis effects [91, 92] when the coils are turned on and off, which would account for slight variations between sessions.

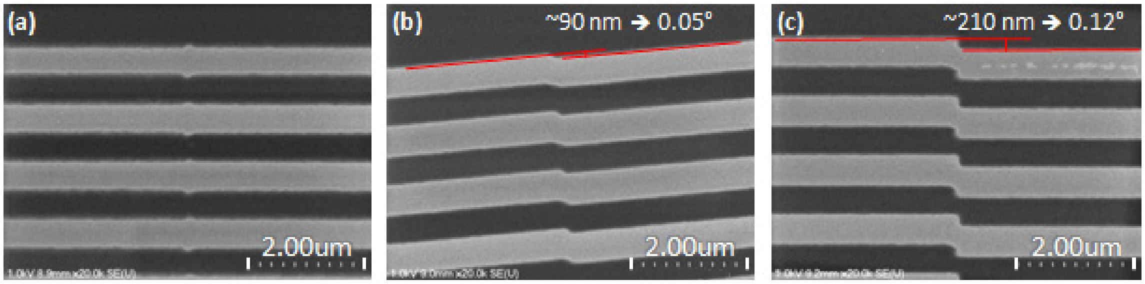

Figure 4.8: SEM images of three separate lithography trials, each with a raster rotation of -0.3°, showing worse alignment over time. (50 nm PMMA on Si.)

Although not yet attempted, it has been suggested that it may be possible to characterize the angle between the field and stage in the same session as the lithography itself. This improvement would avoid any shift in the field-stage offset that presumably occurs when the voltage coils are shut down and then turned on again. The characterization could be done by using a second polymer sample which is very susceptible to the build-up of polymerized hydrocarbons on its surface. In brief, certain polymers have a residual amount of solvent present that will degas to the surface of the sample and become polymerized by the energy of the electron beam, creating a "contamination feature" that can be observed under the electron microscope [93]. On this sample it would be possible to expose the edges of two adjacent fields in a manner such that an observable amount of carbon builds up on the surface. By then immediately imaging the two adjacent samples, it would be possible to measure the field-stage angle and then apply this correction to the raster rotation.

4.3.4 Simultaneous x and y Axis Stitching

It would initially be expected that the above method described for aligning the stage and field axes would provide precise stitching of fields in both the x and y directions. To test these capabilities, the lithography system was aligned using the stage-field characterization method described above.

Then, under identical conditions, two fields were stitched in the x direction, immediately followed by two fields in the y direction, as shown in Figure 4.9. The stitching in the x-axis is accurate to within the limits of the raster rotation control, but the stitching in the y-axis is several times worse.

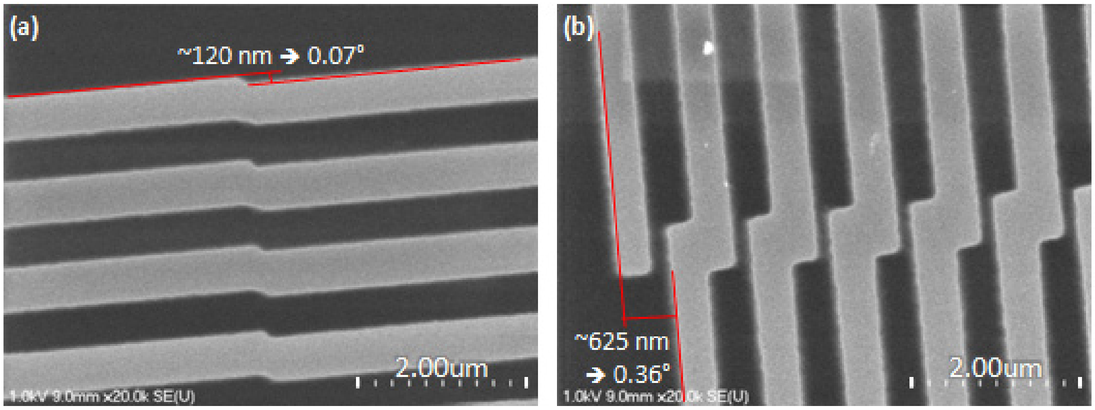

Figure 4.9: SEM images of **(a)** field stitching in the x-axis, followed immediately in the same test by **(b)** field stitching in the y-axis. (50 nm PMMA on Si.)

Two principal reasons are proposed as possible causes for this alignment problem. Firstly, the field written by the electron beam may be slightly sheared. As illustrated in Figure 4.10a, this type of distortion would mean that alignment would be correct in one axis, but not both. Secondly, it is also possible that the axes of the stage are not exactly at 90° to each other. Consequentially, as illustrated in Figure 4.10b, the stage would move nominally in the y direction, but would actually also have some movement in the x direction. Attempts were made to measure the dimensions and angles of exposed squares in order to determine whether either or both of these effects were present; however, for such small measurements the results were inconclusive.

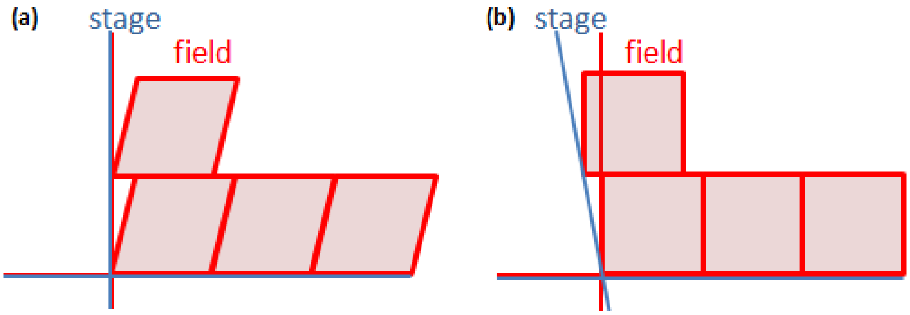

Figure 4.10: Illustration of possible causes of misaligned stitching in the y-axis even when the x-axis is stitched correctly: **(a)** write-field shear, and **(b)** stage axes not at exactly 90° to each other.

But regardless of the cause of these misalignments, it was possible to implement a procedure to provide precise stitching along the second axis. Similar to the stage-field characterization, this procedure involved correcting for errors observed in previous lithography sessions, this time through altered control of the stage. Referring to Figure 4.10, the correction requires that for a specified motion nominally in just the y direction, a small amount of motion in the x direction is also required. From the image in Figure 4.9b, the required correction is approximately 625 nm. Initially this correction was implemented by altering the rotational matrix implemented in NPGS that transforms the given set of stage coordinates to new coordinates with altered axes. But as shown in Figure 4.11, this implementation of the method appeared to provide either no correction (Figure 4.11b), or an overcorrection (Figure 4.11c).

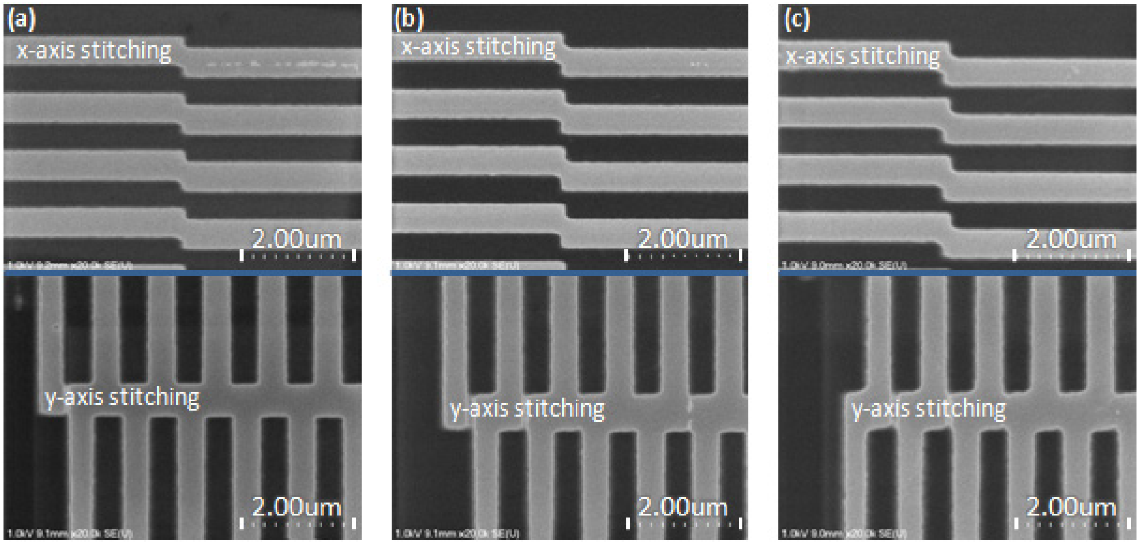

Figure 4.11: SEM images of three cases of simultaneous x and y axis stitching. In all three cases the x-axis rotation was slightly over-corrected with the raster rotation parameter, but the effects of the rotational matrix correction can still be seen in the y-axis. **(a)** No rotational matrix correction. **(b)** A rotational matrix correction of 0.24° (matrix: [1, 0.0042; 0, 1]) provides identical results to the reference case. **(c)** A rotational matrix correction of 0.32° (matrix: [1, 0.0052; 0, 1]) provides an over-correction compared to the reference case. (50 nm PMMA on Si.)

Essentially, it appears that NPGS does not implement the required precision on its rotational matrix calculations. However, as discussed in Section 4.3.2, the stage itself can be controlled with precision down to approximately 10 nm, which is considerably better than the offsets of several hundred nanometres shown in Figure 4.11. Therefore, the required coordinates were calculated based on the desired rotational matrix and sent them directly to the stage via HyperTerminal without using NPGS. As shown in Figure 4.12, this method provided very high precision stitching in both axes: within 0.04° in the x axis, and within 0.03° in the y axis.

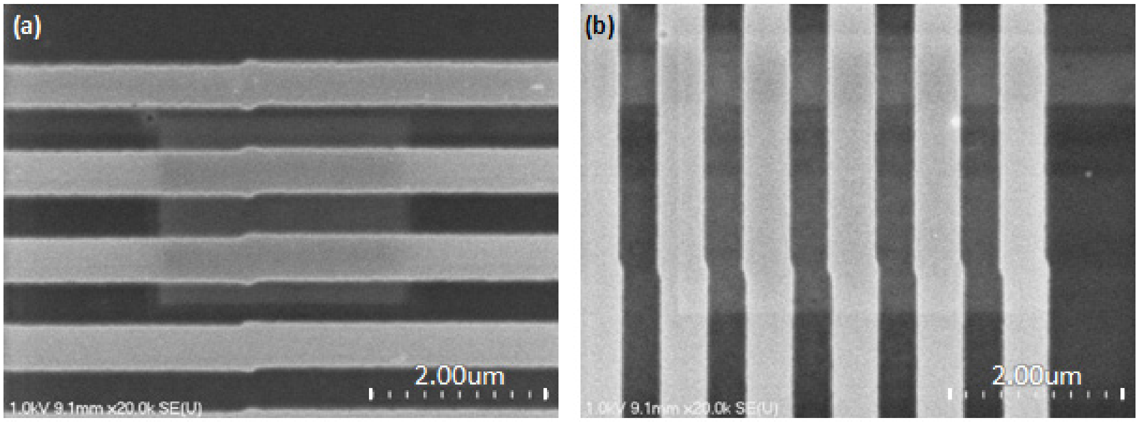

Figure 4.12: SEM images of **(a)** precise stitching in the x-axis, and **(b)** simultaneous precise stitching in the y-axis, implemented using a rotational matrix correction of 0.24° (matrix: [1, 0.0055; 0, 1]), sent directly to the stage via HyperTerminal, rather than by NPGS. (50 nm PMMA on Si.)

These results indicate that it should be possible to accurately stitch multiple fields to produce an entire diffractive lens. Although not yet implemented, the correction described above should be possible to automate. Ideally, a modification would be made directly within the NPGS program to calculate coordinates with the required degree of precision. Alternatively, it would be possible to create a script that calculates the coordinates and sends them to the stage via HyperTerminal.

It is also worth noting that while the results presented in this section were obtained based upon the stage-field characterization method described in Section 4.3.3.2, the alignment mark method of Section 4.3.3.1 should be equally capable of producing similar results. The results in Figure 4.5 and Figure 4.9 are essentially comparable, with the slight misalignment in the x-direction caused by a lack of high precision in raster rotation control, and the larger misalignment in the y-direction caused by the stage movement issues identified in this section. Therefore, with a correction to the y-axis stitching implemented in NPGS, it should be possible to use the alignment mark method with equal accuracy, thus making it possible to align the sample, stage, and field axes.

4.4 Line Width Control

The most critical parameter in the fabrication of a cylindrical lens is its pitch, since it determines the diffracted angle in accordance with the grating equation. The pitch of the lens is controlled by where adjacent lines are defined in software, and should be relatively stable regardless of process variations such as exposure dose and development time.

However, for high diffraction efficiency it is also important to have control over the width of the lines to maintain the intended duty cycle of the grating. Such control is of particular importance for multi-level structures owing to the potential for etching artefacts resulting from misplaced lines, but is also relevant for two-level structures.

For the binary-level device, the line widths required were between 640 and 680 nm. While these line widths are comparatively large for electron beam lithography, their variation from one end of the device is only 40 nm. Initial tests showed that to maintain a level of control capable of gradually producing this trend across the sample, the sample should be patterned using as low a beam current as possible. For the Hitatchi SU-70 system, the lowest possible beam current was between 14 and 17 pA. This value was constant within approximately 0.1 pA for a single session, and dose calibrations in NPGS allowed for exposure dose consistency from one session to the next. With a low beam current the beam must trace out many adjacent lines to create the overall width of the desired line, rather than a higher beam current that would require fewer adjacent lines. However, the trade-off to this approach is that the pattern is written very slowly, typically about 10 or 15 minutes for an area 100 by 100 μm patterned with a 50% duty cycle of 660 nm lines. It is possible that once the control process has been fully optimized it would be possible to increase the beam current and thus write the patterns faster, or alternatively to investigate a defocusing method such as that discussed in Chapter 2 [71] in order to write each line with a single pass of the beam.

To assess the width and pitch of fabricated features, SEM images of features replicated in chromium (step f in Figure 4.1) were taken and analyzed using an automated technique. First the image was rotated through a range of angles to determine which gave the sharpest contrast when vertically averaging the image. The peaks of the best vertically averaged image were taken to be the edges of the features. A representative analysis image with an overlay of its vertical average is shown in Figure 4.13. The texture of the chromium mask is thought to be a result of the chromium deposition process, and was used to help ensure that each image was in sharp focus.

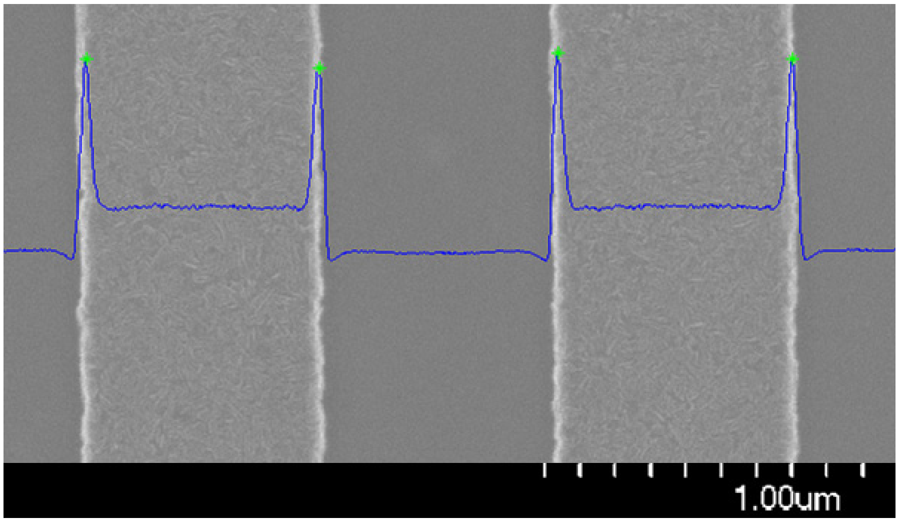

Figure 4.13: Representative SEM image used for analysis of line width and pitch, with vertically averaged data overlaid. (50 nm Cr on Si.)

To determine whether the line width was influenced by its position or the order in which it was written, many sets of lines all nominally 660 nm wide were written in a single write field in the order illustrated in Figure 4.14a. However, as can be seen from Figure 4.14b, there was no clear relationship in line width to vertical or horizontal position within the write field, or to the order in which the lines were written. As discussed with more detailed analysis in Chapter 5.2, an individual line width measurement is estimated to be accurate within ±3 nm. However, the standard deviation of the data points in Figure 4.14b is approximately 6 nm, suggesting that variation between lines exceeds the variation within a single line. This variation is consistent with the variation of the final device presented in Chapter 5.2.

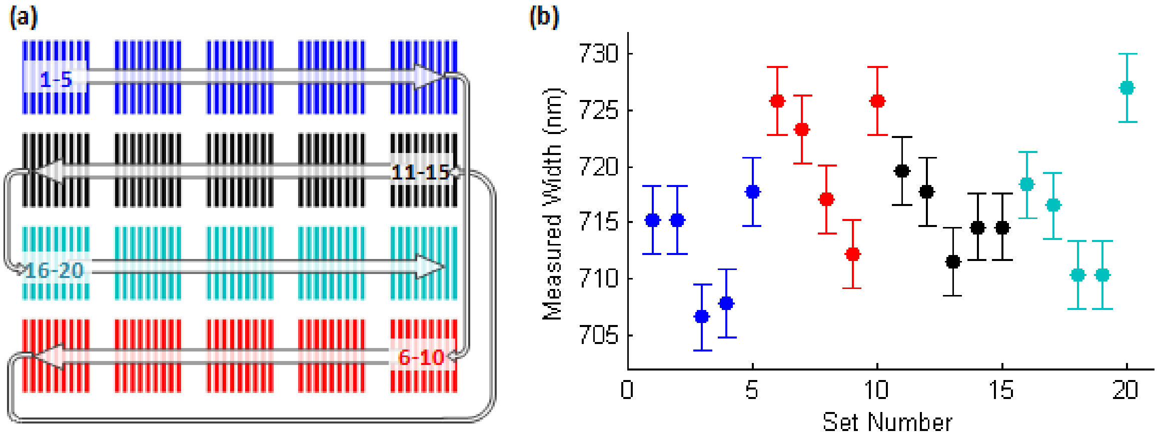

Figure 4.14: (a) Illustration of the order in which identical sets of lines were written (each line was 12 µm tall with a width of 660 nm and pitch of 1320 nm). **(b)** Measured line widths for the central line of each set.

However, the one clear trend from the data in Figure 4.14b is that the lines were all considerably wider than their nominal value: on average 716 nm instead of the desired 660 nm. As a first approximation it was assumed that this scaling factor would be linear; and therefore that the desired line widths should be scaled by a factor of 0.92 prior to patterning. This correction can be written simply as

$$LW_{nom.scaled} = 0.92 \cdot LW_{desired}. \tag{4.1}$$

The scaling factor was tested for a range of desired line widths of between 645 and 675 nm all at a 50% duty cycle, and as shown in Figure 4.15, it did bring the measured line widths closer to their desired values. Although the data points are not very well described by a linear fit, there does appear to be a trend in the measured widths as a function of the nominal width. However, while the desired range of line widths was 30 nm, the measured range according to the linear fit was slightly less than 20 nm. The cause of this discrepancy was presumed to be the proximity effect discussed in Chapter 2, whereby the dose required for a given line is dependent on the density of the surrounding features and not just the size of the feature itself. Therefore, since the narrower lines are also more tightly packed, they experience a greater proximity effect and thus end up being wider than expected.

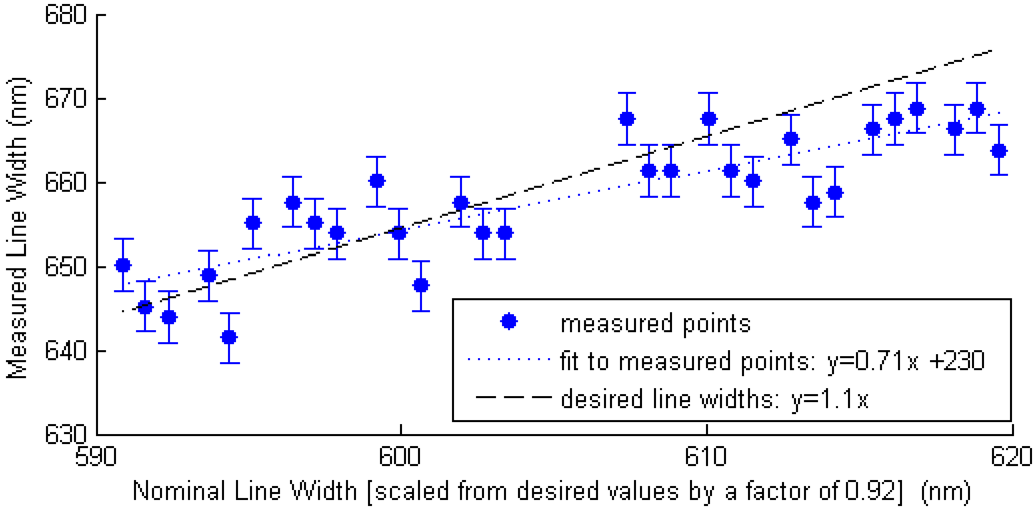

Figure 4.15: Measured and desired line widths as patterned using a linear scaling correction factor.

To correct for the proximity effect, it was first observed that the fit to the measured points matches correctly with the desired width at a nominal value of 599 nm. For nominal values either side of this point, a further correction is required using the slopes of these two lines: the slope of the measured points essentially needs to be increased by the ratio of the two slopes, equal to 0.65. This second correction can be written as

$$LW_{nom.slopes} = LW_{nom.scaled} + 0.65 \cdot (LW_{nom.scaled} - 599\,nm). \qquad (4.2)$$

Combining the slope correction with the scaling correction from Equation 4.1, the overall correction can be calculated as

$$LW_{nom.} = 1.5 \cdot LW_{desired} - 389\ nm. \tag{4.3}$$

As will be presented in Chapter 5, this correction was effective over a range of line widths between 640 and 675 nm, providing line widths with a trend-line within 2 nm of the desired trend-line, and individual points that were at most 12 nm from their desired values. These results have not yet been replicated, so in the future it will be important to test the repeatability of this calibration. Furthermore, the calibration was performed for a relatively narrow range of feature sizes at a 50% duty cycle, and so its broader applicability for more general patterns is expected to be limited.

4.5 Future Development

As has been mentioned throughout this chapter, there are a number of modifications and areas of further development that are still necessary for consistent and large scale fabrication. These issues are summarized in Table 4.2.

Table 4.2: Summary of issues to be addressed in further process development.

4-level device	
	- spray coating of PMMA and EL 6 - alignment of field and stage axes to sample axes for second patterning iteration
Polymer device	
	- optimization of etch depth for use as a polymer mould or stamp - verification of polymer replication procedure (not in-house)
Full-size device	
	- automation of rotation alignment method for simultaneous x and y axis stitching - improvement of writing speed
Miscellaneous improvements	
	- optimization of silicon etch recipe for sharper side-walls - real-time stage-field angle characterization for improved alignment control - verification of consistency for line width calibration method

4.6 Summary

Development of a fabrication process using the facilities available at McGill University has involved a considerable amount of investigation into the optimization of various process parameters, as well as the development of procedures to use the EBL system with as much precision as possible. Although the optimization of the process is not yet complete, the process described above has demonstrated the feasibility of using McGill's facilities to fabricate diffractive optics. As will be demonstrated in Chapter 5, this process has been used to fabricate a portion of the design presented in Chapter 3.

5 : RESULTS AND DISCUSSION

5.1 Introduction

This chapter demonstrates a proof-of-concept device fabricated at McGill University: a two-level diffractive lens fabricated in silicon. The lens was not yet replicated in a transparent polymer, but its optical properties were verified by utilizing the lens in a reflective configuration. First, this chapter evaluates the fidelity of the fabricated design when compared to intended specifications. It next describes the expected lens performance and implemented optical test configurations, and lastly presents the optical results and provides a discussion of the apparent limitations of the device's performance.

5.2 Fabrication Measurements

The lens was fabricated with the process flow described in Chapter 4, using a liftoff process to create a hard chromium mask, followed by RIE of the silicon substrate. To assess the accuracy with which the desired pattern had been fabricated, SEM images were taken of the chromium mask prior to etching, since at this point there is a higher degree of contrast than the bare silicon that remains after etching and mask removal. The fidelity of pattern transfer to the silicon is reasonably high, but the differences between the pattern at this imaged step and after the mask removal will be subsequently discussed. Figure 5.1a shows a complete view of the lens, approximately 1.2 mm long by 90 μm tall. Figure 5.1b and Figure 5.1c show portions of the device at increasing magnifications.

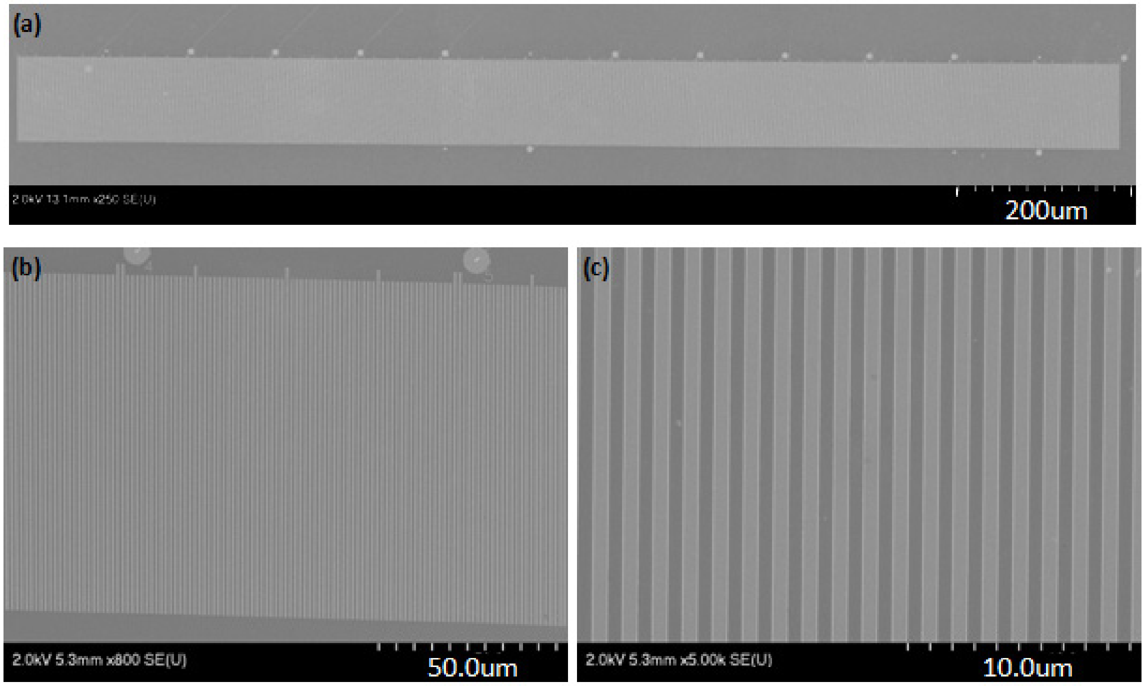

Figure 5.1: SEM images of the fabricated lens after the liftoff step. (50 nm Cr on Si.) **(a)** The entire device, imaged at 250x magnification. **(b)** A representative central portion of the device imaged at 800x magnification. **(c)** The central portion of the 800x image, taken at 5000x magnification.

Figure 5.2 shows two adjacent extensions from the main design, which define the edges of two EBL fields (as presented in the pattern layout described in Chapter 3). The rotational alignment of the fields is within approximately 0.03°, which is well below what can be corrected for with the raster rotation parameter discussed in Chapter 4. Using the same measurement technique described in Chapter 4.4 for measuring pitch, the pitch between the two lines in separate fields was found to be 1273 ± 2 nm, compared to the intended 1283 nm. Considering that the stage can be expected to display approximately 10 nm of positioning error, the alignment accuracy is likely close to the limits of what could be obtained by the system.

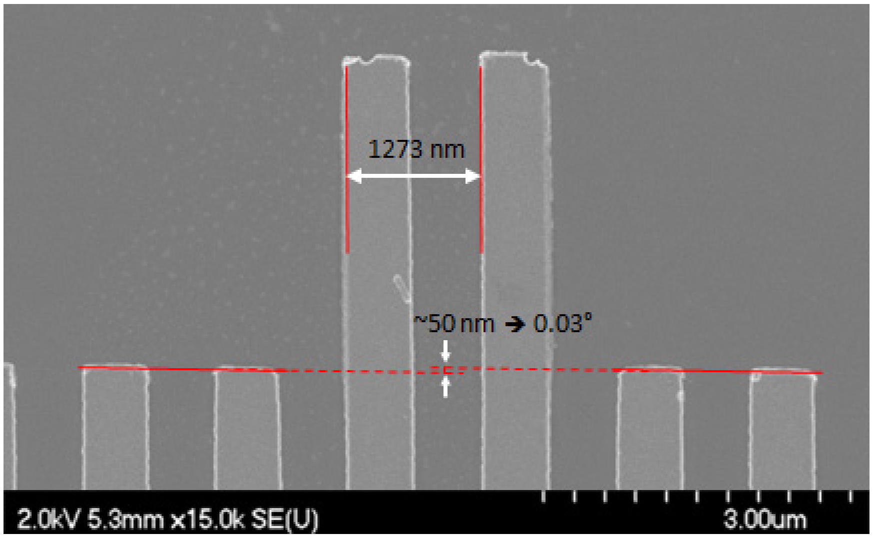

Figure 5.2: SEM image of two adjacent EBL fields, displaying accurate rotational and lateral alignment. (50 nm Cr on Si.)

Again using the automated technique for line width and pitch measurement described in Chapter 4, the line width and pitch were measured at three points on each of the thirteen EBL write fields. One such image used for measurement is shown in Figure 5.3, and the overall results are plotted in Figure 5.4. Measurement errors for the pitch and width were estimated by measuring a single line at five points along its length and determining the standard deviation of these measurements: 2 nm for the pitch, and 3 nm for the width. As discussed further below, estimates on measurement error are important in order to determine the extent to which observed points are indicative of fabrication errors.

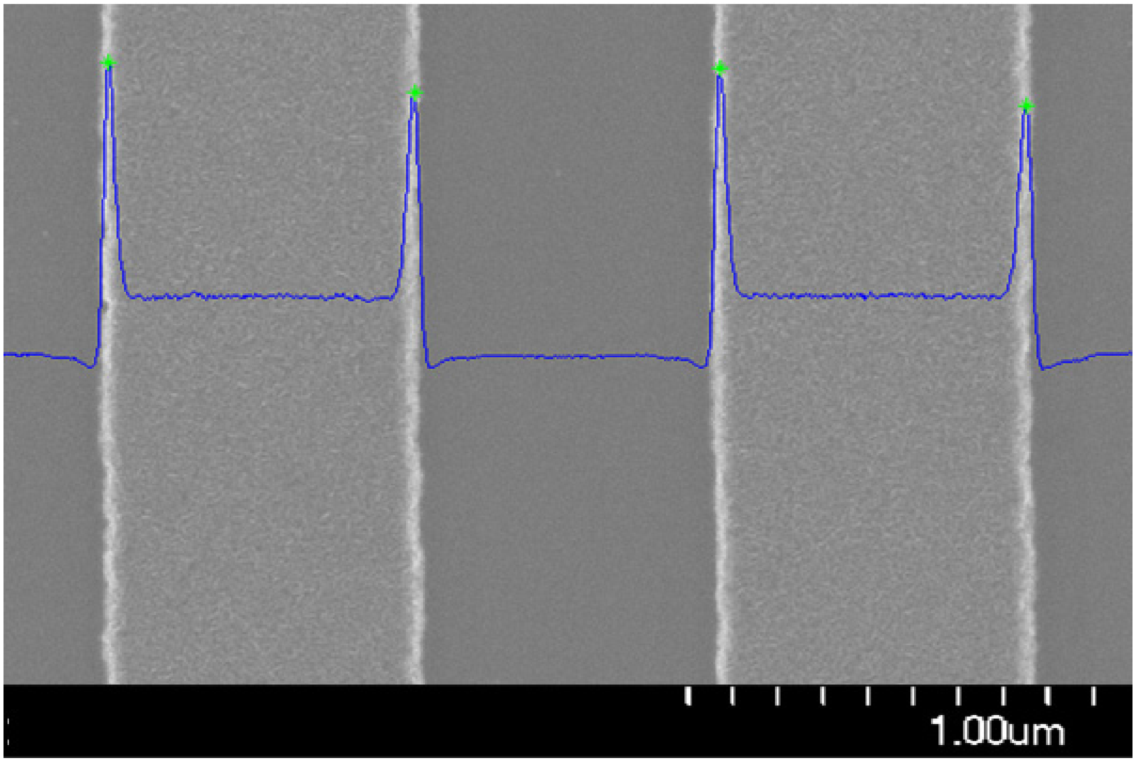

Figure 5.3: One of the SEM images used to measure the width and pitch of the fabricated device. (50 nm Cr on Si.)

The focal length of the lens is determined by the systematic variation in its pitch, which is found to be -0.065 ± 0.006 nm/µm, compared with the desired trend of -0.064 nm/µm, indicating that the focal length of the lens should be very close to that of the design. The fabricated pitch is consistently larger than the desired pitch by approximately 10 nm. However, this systematic shift is essentially equivalent to fabricating a portion of the lens slightly closer to the optical axis than intended by the design, and should not significantly affect the performance of the lens.

In terms of random errors, as mentioned above, the measurement error associated with the data points for the line pitch is estimated at 2 nm. However, the root-mean squared deviation of the data points from the linear fit is 6 nm, which indicates that the data has a greater variation about the trend-line than would be expected from measurement error alone, and suggests that the variance of fabrication errors is approximately 6 nm. This type of fabrication error in the lens pitch would be expected to affect the efficiency of the lens, with more variation from the intended design leading to more scattering and therefore lower efficiency.

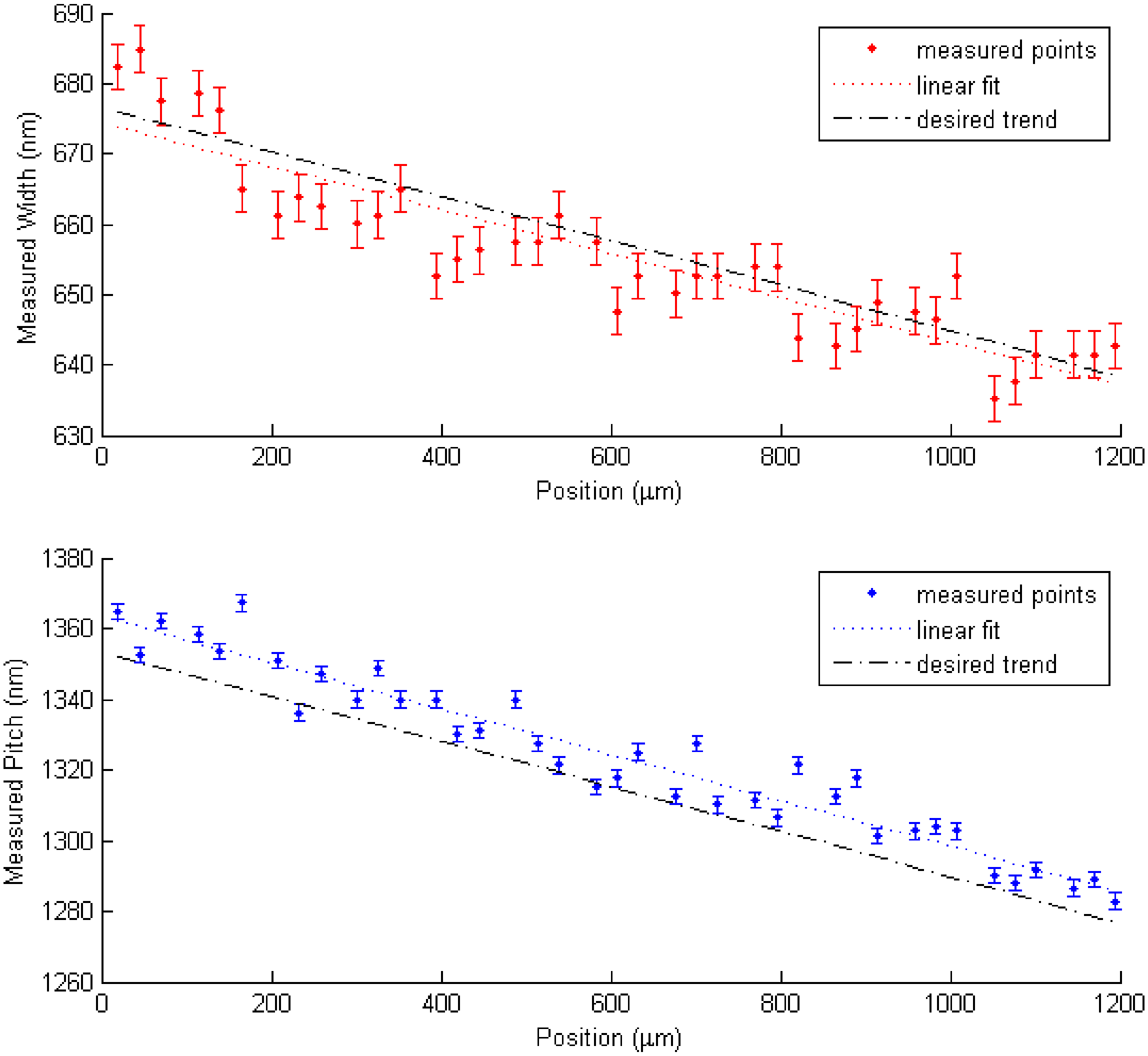

Figure 5.4: (a) Plot of the measured width of features on the fabricated device. Linear fit to y = m·x+b with m = -0.031(5) nm/μm, b = 674.5(3) nm; R-squared = 0.8232. The desired trend was m = -0.032 nm/μm, b = 676.7 nm. **(b)** Plot of the measured pitch of features on the fabricated device. Linear fit to y = m·x+b with m = -0.065(6) nm/μm, b = 1363(4) nm; R-squared = 0.9324. The desired trend was m = -0.064 nm/μm, b = 1353 nm.

After characterizing the sample with SEM images, it was etched with the recipe described in Chapter 4, after which the chromium mask was removed. To compare the feature profiles before and after the etch, three measurements were performed at evenly spaced points across the sample. Although the pitch measurements remained consistent, the width of the features was broadened by approximately 50 nm.

Once the optical measurements described below were completed, the sample was cross-sectioned to measure the etch effects in more detail. Figure 5.5a shows a perspective view of the cross-section, where some surface roughness is apparent, particularly on the tops of the etched features, as well as noticeable corrugation on the side wall surfaces. Figure 5.5b provides a side-on view with measurements of the feature dimensions. The etch-depth is measured to be approximately 174 nm as opposed to the desired 212.5 nm. When considering the horizontal dimension, the pitch is larger than any of the measurements in Figure 5.4, owing to the fact that the cross-section did not slice through the sample exactly perpendicular to the features, but at an angle estimated to be about 20°. Nevertheless, the ratio of the measured pitch and width should still give an accurate indication of the duty cycle: approximately 52% at the top, and 55% at the bottom, as opposed to the ideal 50%. These variations can also be considered in terms of the angle of the side walls, which are approximately 7° from vertical. As will be discussed in Section 5.4, these various imperfections will all have an impact on the efficiency of the lens.

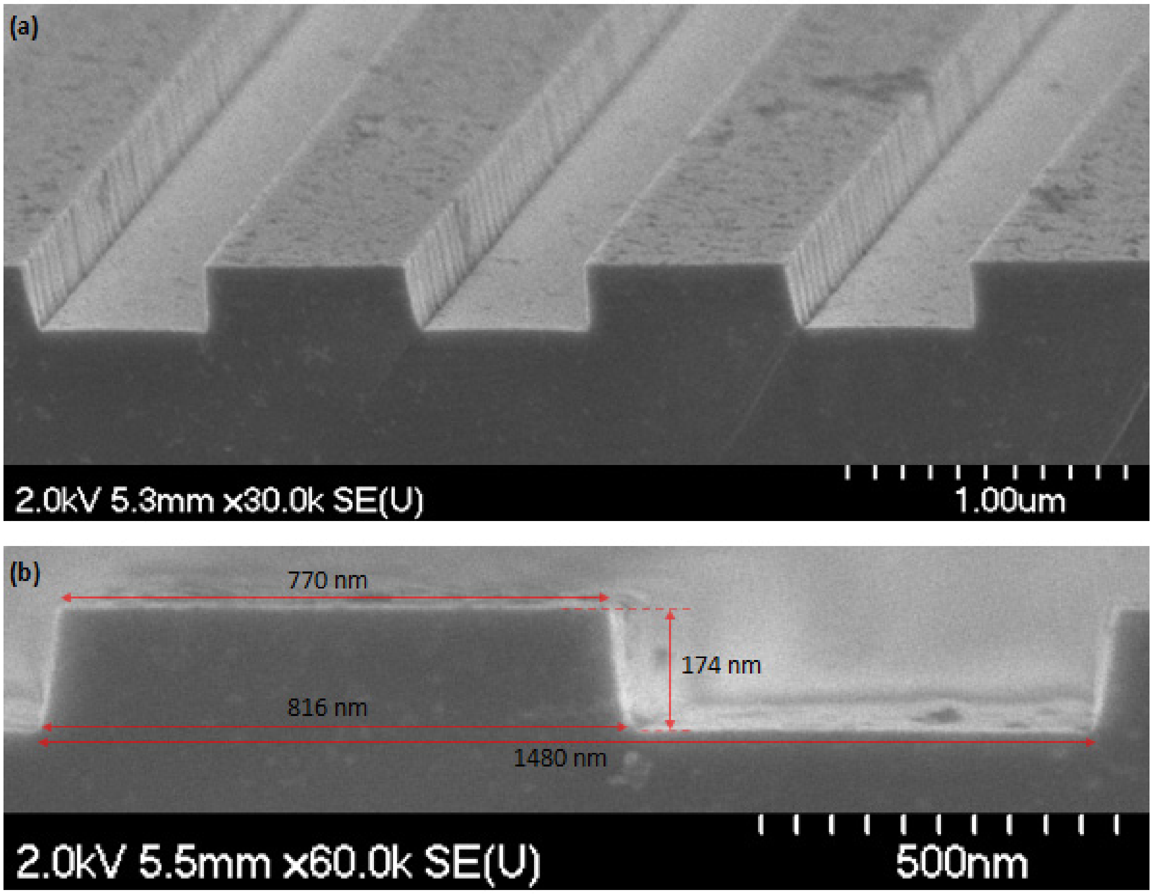

Figure 5.5: (a) SEM image showing an angled view of the cross-sectioned sample. **(b)** SEM image of the cross-sectioned sample. The measurements appear inconsistent with the values presented in Figure 5.4 because the cross-section was not perfectly perpendicular to the features.

5.3 Optical Testing

The fabricated lens was tested as a reflective device, which was expected to alter its focusing characteristics in comparison to the original transmissive design. Therefore, as presented below, the location of its focal spot was first modelled using the same theory used to design the original lens, and then a test configuration was implemented based on the expected lens characteristics.

5.3.1 Predicted Focal Spot

The design presented in Chapter 3 was created as a transmissive device which would function correctly when replicated in a polymer with a refractive index of 1.5. However, for this thesis the polymer replication was not yet completed, and therefore the device was instead tested directly on the silicon substrate as a focusing diffractive mirror. This modification will alter the focal properties of the lens, as can be seen by rearranging the grating equation of Equation 2.2 to solve for diffracted angles θ_2 as

$$\theta_2(x) = \sin^{-1}\left[\frac{1}{n_2}\left(\frac{m\lambda}{\Lambda(\mathrm{x})} + n_1 \sin\theta_1\right)\right]. \tag{5.1}$$

In a reflective configuration, both n_1 and n_2 will be 1. For the dimensions of the fabricated device, with the original intended incident angle of 45°, wavelength of 850 nm, and +1 diffractive order, the argument for the arcsin will be greater than 1, which means that the +1 diffraction order will not propagate. However, the -1 diffraction order will propagate, with diffracted angles between 2.6 and 4.8°.

The location of the -1 order can be illustrated by plotting rays emanating from multiple points along the lens, based upon the lens' intended pitch and the resulting values of θ_2, as in Figure 5.6a. This plot illustrates light incident on the diffractive lens, and the resulting diffraction that occurs from various points, as shown in dark blue. For this configuration the -1 order produces diverging rays, and therefore ray traces of the diffracted light are shown in light blue going backwards towards the virtual focal point, which occurs at a distance of 31.5 mm. Figure 5.6b shows an enlargement of the focal point, indicating that the virtual spot size should be approximately 30 μm. In other words, the size of the virtual focus spot is predominated by severe geometric aberrations, which is the result of the erroneous linear lens profile that was discussed in Chapter 3, as well as the fact that the lens is being tested in a reflective configuration. Nonetheless, the model does suggest that for uniform illumination of the sample, the beam should have a virtual focus that is compressed from its original width by a factor of 40, or equally that when illuminated by a Gaussian beam, the width of the virtual Gaussian spot should be compressed by a factor of 40 from its original width.

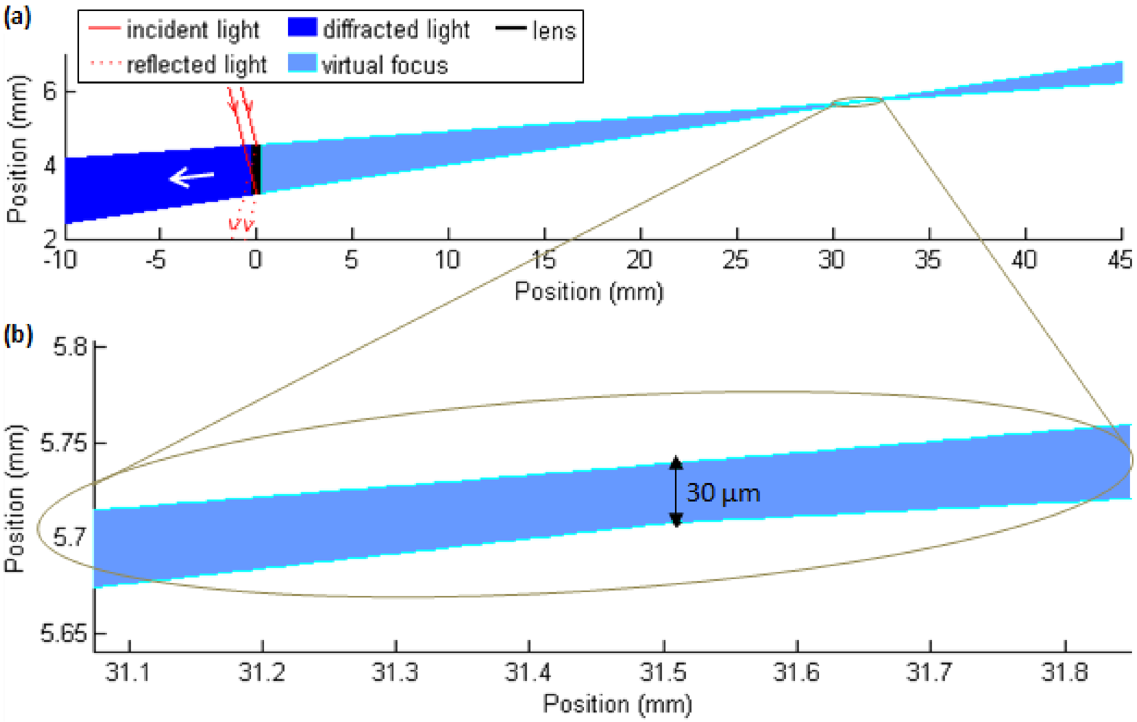

Figure 5.6: (a) Ray tracing illustration of the virtual focal point of the designed device for the m=-1 diffractive order, based upon Equation 5.1. **(b)** Enlargement of the designed focal point, illustrating that the spot size is not diffraction-limited.

To obtain a converging lens, it is necessary to alter the incident angle such that the +1 diffraction order propagates. Similar ray trace plots to the one shown above indicate that the sharpest focus will occur for light that is almost normal to the surface. As shown in Figure 5.7a, at an incident angle of 1°, light will focus approximately 13 mm in front of the lens, over a range of angles between 40.2 and 43.4°. Figure 5.7b shows that the focal point will be approximately 55 µm wide, which again is dominated by geometric aberrations rather than the diffraction limit of an optimal design. However, this model does represent a compression of the beam by a factor of 21.8.

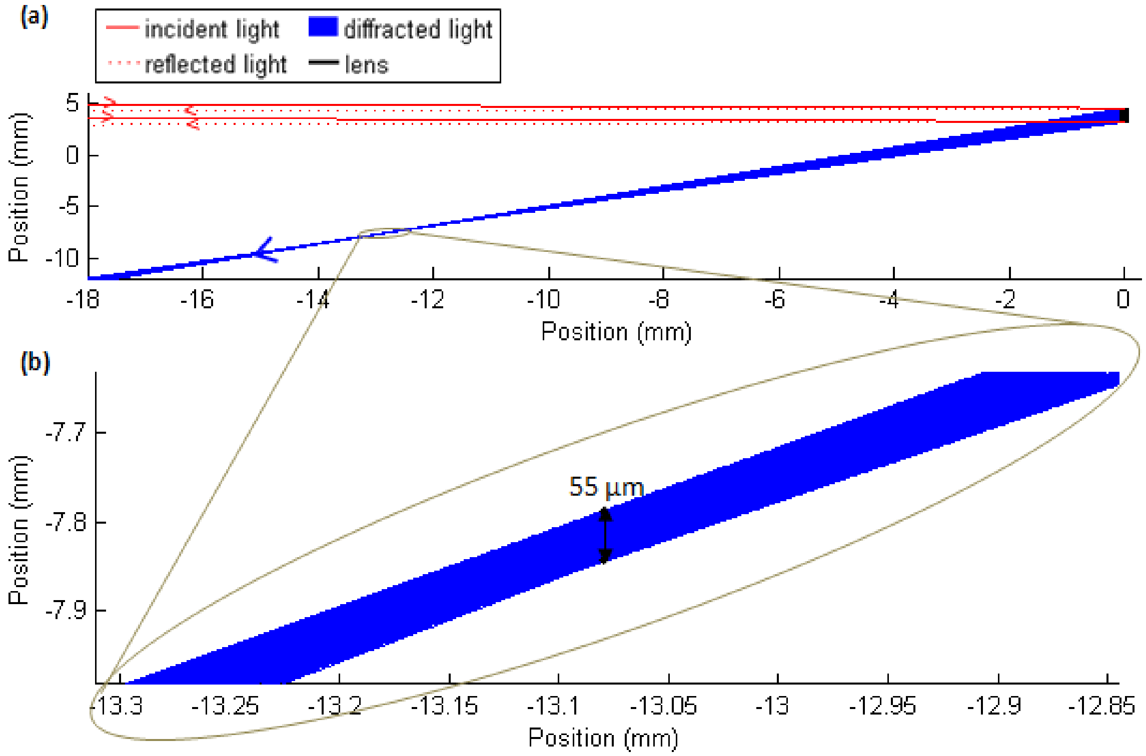

Figure 5.7: (a) Ray tracing illustration of the focal point of the designed device for the m=+1 diffractive order, based upon Equation 5.1. **(b)** Enlargement of the designed focal point.

5.3.2 Experimental Set-Up

The experimental configuration for testing the lens was designed based upon the expected locations of the -1 and +1 diffractive orders as discussed in Section 5.3.1. Figure 5.8 shows two possible configuration of the system, one used to observe the light reflected directly off the sample, and the other to observe the -1 diffracted order. A similar configuration was also used to observe the +1 diffracted order: incident light was provided at an almost normal angle to the sample surface, and the diffracted light was observed at a 40° angle from the sample surface. For this order, the f = 60 mm lens shown in configuration #2 was replaced with an f = 30 mm lens owing to the fact that the focal point was in front of the sample rather than behind it.

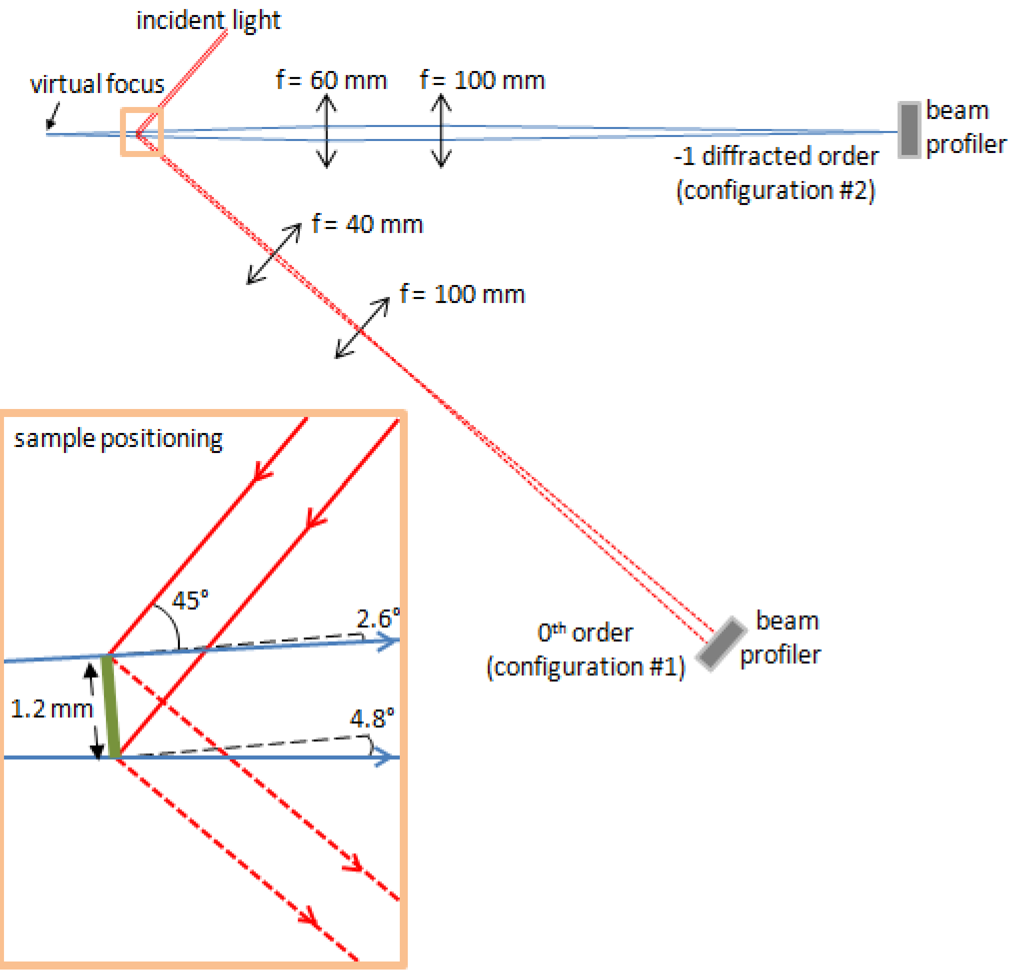

Figure 5.8: Schematic of two variations of the experimental configuration used for optical testing. The insert shows a closer view of the angles involved at the sample surface. Configuration #1 creates an image of the sample surface at the detector: the first lens is 40 mm from the sample, the second lens is approximately 30 mm away from the first lens, and the detector is 100 mm away from the second lens. Configuration #2 collects the m = -1 diffractive order and then refocuses it at the detector: the first lens is 60 mm from the virtual focus point, the second lens is approximately 30 mm from the first lens, and the detector is 100 mm from the second lens.

Illumination was provided by an SDL-8630 tunable laser diode at a wavelength of 850 nm with a nominal multi-mode line-width of 0.02 nm. The laser light was filtered by a band-pass filter centred at 850 nm with a FWHM of 10 nm to remove a broader spectrum that was otherwise seen around 830 nm. The light was also TM polarized prior to hitting the sample. The sample, lenses, and beam profiler were placed on rotation stages such that they could all be rotated together with respect to the incident light, and such that the lenses and beam profiler could be rotated together with respect to the sample. The beam profiler used was an LBP-2-USB from Newport Corp., which uses a silicon CCD camera with a detector area of 6.47 by 4.83 mm.

5.3.3 Optical Measurements

5.3.3.1 0th Diffractive Order

Using the experimental configuration described in Section 5.3.2, a collimated laser beam was centred on the fabricated sample. The power of the incident beam was approximately 3.5 μW, as measured with a free-space optical power meter. For 850 nm light, two-thirds of the incident power would be absorbed by the silicon, leaving approximately 1.2 μW that could be diffracted or reflected by the sample.

Figure 5.9 shows the intensity plot of light reflected off the fabricated sample, obtained by using configuration #1 from Figure 5.8 to image the surface of the sample. Light incident on areas surrounding the grating is merely reflected, but there is comparatively little light reflecting directly off the grating itself, indicating that it is instead being diffracted or otherwise scattered by the grating features. The power measured by the beam profiler was approximately 0.83 μW, accounting for about 70% of the expected reflected power. The remaining 0.37 μW of the expected power is assumed to be either diffracted or scattered by the grating.

In addition to the scaling factor included to account for the beam expander used during imaging, the x-axis of Figure 5.9 has also been scaled by a factor of 1/sin(45°) to account for the 45° angle at which the sample was observed. As such, the dimensions labelled on the image correspond to the actual dimensions of the device, which is confirmed by the fact that in the image the device is approximately 1.2 mm wide, as expected. This scaling factor is also correct when discussing the ratio of the focused m = -1 diffracted order and the incident light, because in Section 5.3.1 light was assumed to be incident on a grating 1.2 mm wide, meaning that the width of the incident beam should also be discussed in terms of its width on the physical sample, rather than before or after striking the angled surface. For the m = +1 diffractive order, this scaling factor was not used when comparing the expected and observed performance, since the incident light was at normal incidence to the sample.

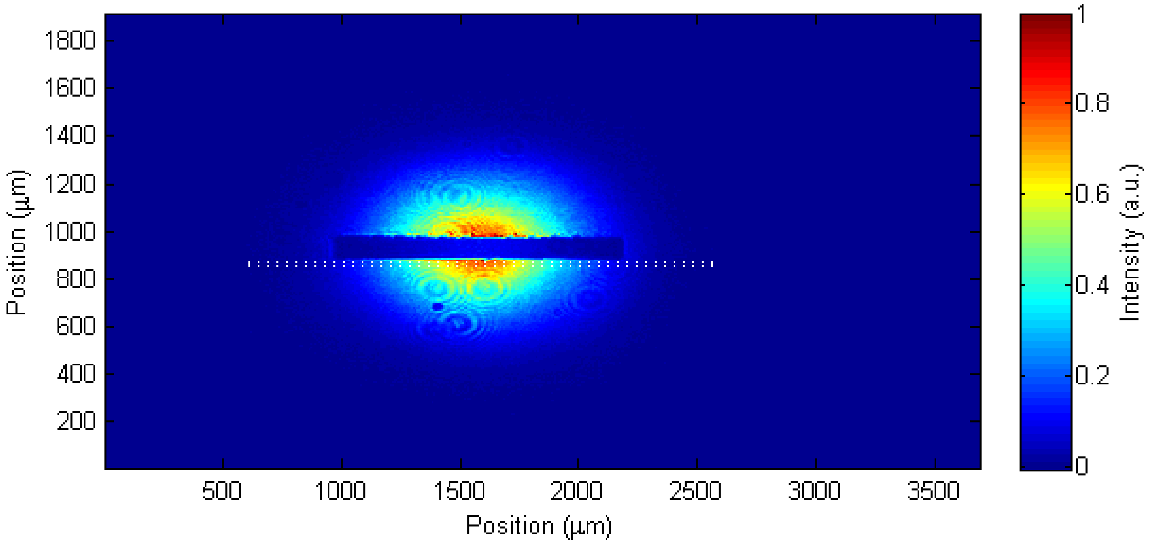

Figure 5.9: Intensity plot of light reflected off the fabricated grating for incident light at 45° to the surface. The position axes have been scaled to account for the beam expander used in imaging, and also to account for the 45° angle relative to the lens surface. Dashed white lines indicate the portion of data used to obtain the profile in Figure 5.10.

In order to compare the profile of the beam that is incident on the sample with the profile of the beam collected after diffraction, a section of the data in Figure 5.9 was used to create a cross-sectional profile of the beam.

The dashed lines in Figure 5.9 indicate six rows of data very close to the diffraction grating, which were averaged to create the profile shown in Figure 5.10. The beam is well-described by a Gaussian fit, despite a small pattern in the residuals.

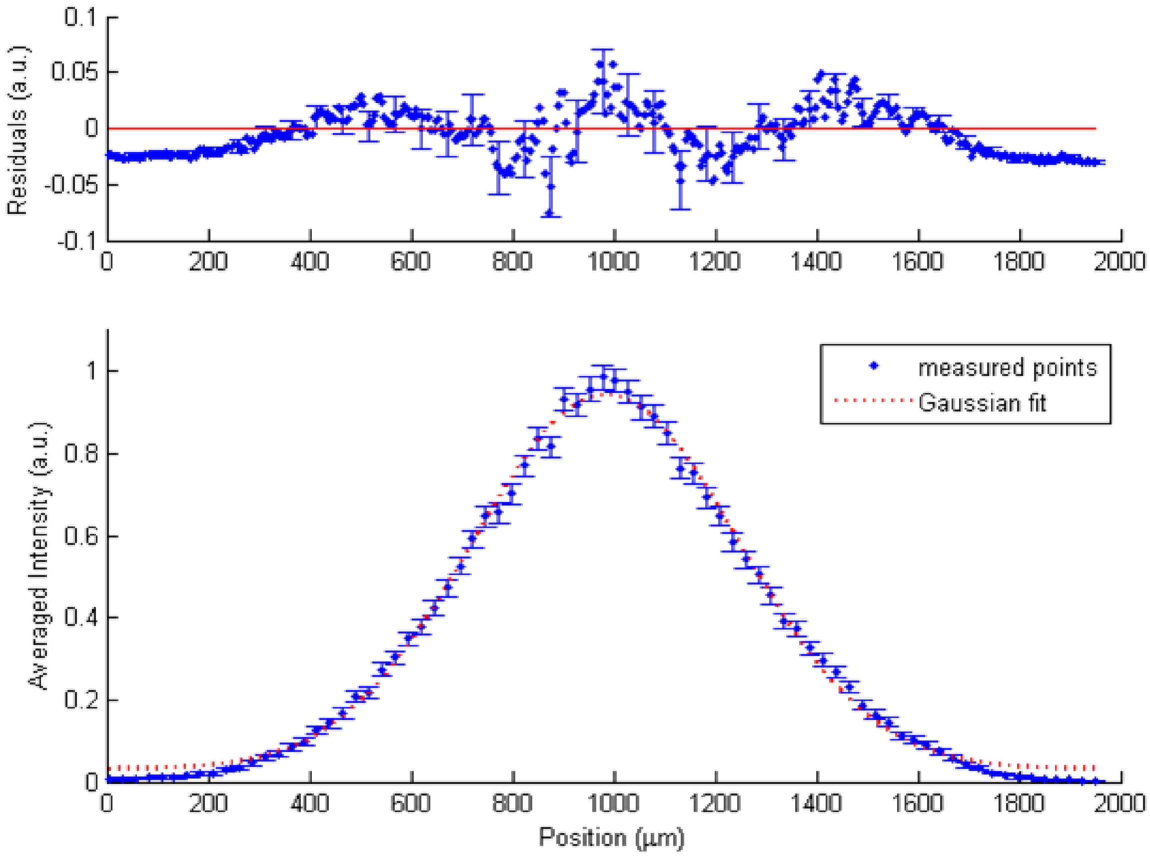

Figure 5.10: Average profile of the six rows of data highlighted in Figure 5.9. For clarity, in the main graph only every 5th data point has been shown; in the residuals plot all residuals are shown but only every 10th error bar is shown, but other error bars are of comparable size. The data was fitted to a Gaussian curve of the form y = a{exp[(x-b)/c]^2}+d, with fit parameters a = 0.913(7) a.u., b = 984(2) μm, c = 370(4) μm, d = 0.031(7) a.u.; R-squared = 0.9952.

5.3.3.2 -1 Diffractive Order

The experimental set-up was altered to configuration #2 of Figure 5.8 to observe the -1 diffracted order, shown in Figure 5.11. As estimated above, approximately 0.37 μW could actually be diffracted or reflected by the lens itself. The beam profiler measured approximately 0.06 μW in the -1 order, meaning that the lens functions with approximately 16% efficiency.

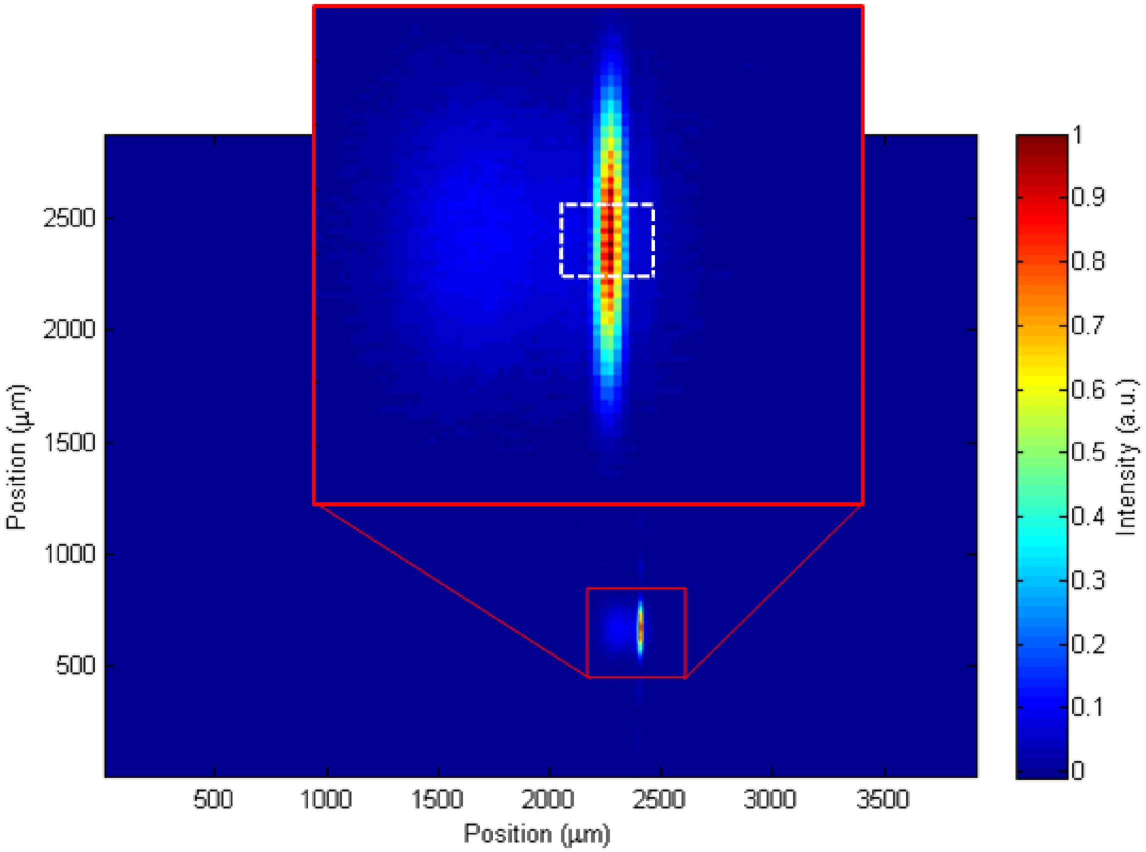

Figure 5.11: Intensity plot of light in the -1 diffracted order. The x and y axes have been scaled to account for the beam expander used during imaging, and thus the image represents the size of the virtual focal spot located behind the fabricated sample. The white dotted line in the top insert indicates data used to create the profile in Figure 5.12.

The data within the dashed lines in Figure 5.11 was vertically averaged to create the profile shown in Figure 5.12, where the main portion of the virtual focal line is still Gaussian in shape. The width of the virtual focus spot is 36±2 times narrower than that of the original incident beam, compared to the theory in Section 5.3.1 that suggested the designed lens should be capable of creating a virtual focus spot 40 times narrower than the incident beam. Therefore, it appears that in terms of spot-size the lens is performing near the limit of what is expected for the design.

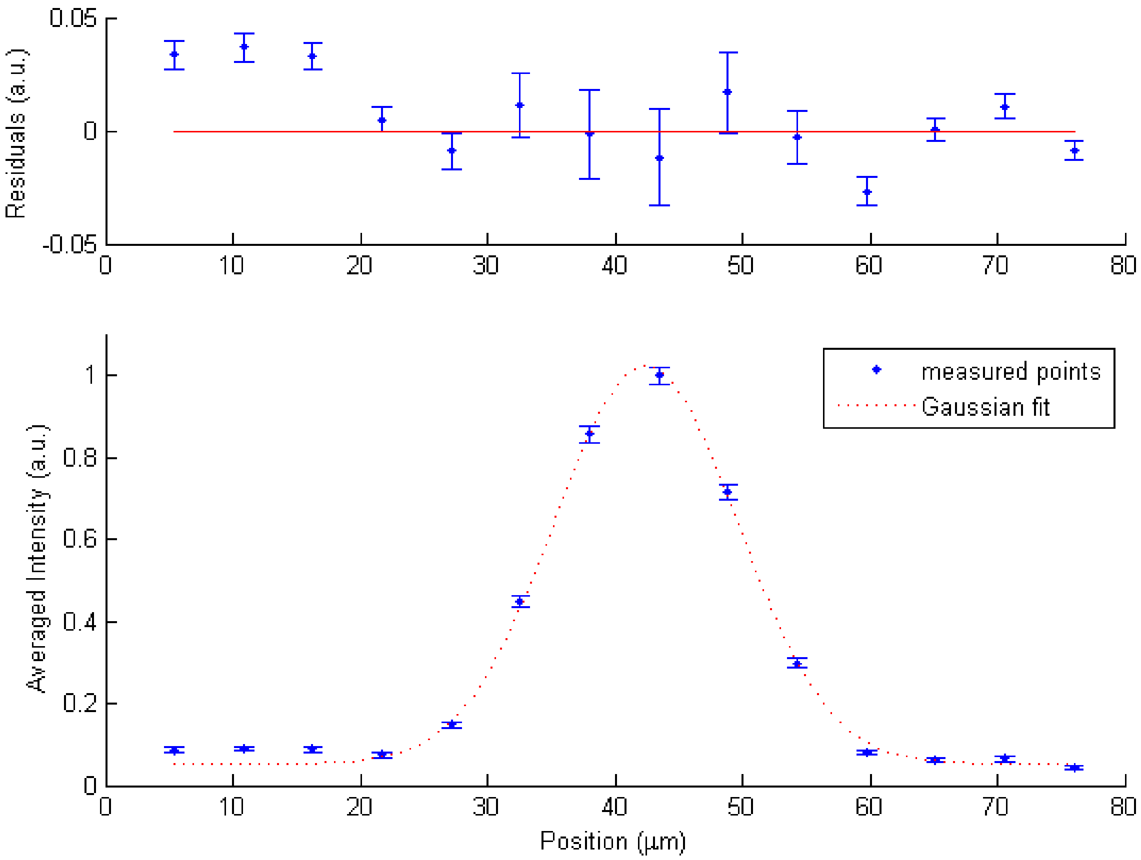

Figure 5.12: Vertically averaged profile of the data bounded by white lines in Figure 5.11. The data was fitted to a Gaussian curve of the form $y = a\{\exp[(x-b)/c]^2\}+d$, with fit parameters a = 0.97(3) a.u., b = 42.4(3) µm, c = 10.2(4) µm, d = 0.05(1) a.u.; R-squared = 0.998.

It is noted that in addition to the main focal point in Figure 5.11, there is also a weaker spot to its left. Although not explicitly verified, this feature is thought to be due to a small amount of light at wavelengths close to 830 nm that was not completely removed by the filter at the input optics.

5.3.3.3 +1 Diffractive Order

The experimental setup of Figure 5.8 was repositioned to instead observe the +1 diffractive order, using incident light at a near-normal angle, and observing the diffracted light at 40°. As explained in Section 5.3.1, it was expected that this focal spot would be slightly broader than the -1 diffractive order, but would result in a real focus point rather than a virtual focus point.

The intensity plot of the focus line is shown in Figure 5.13. Similar to the power measured for the -1 order, the +1 order had approximately 0.07 µW of power, indicating a diffraction efficiency of about 19%.

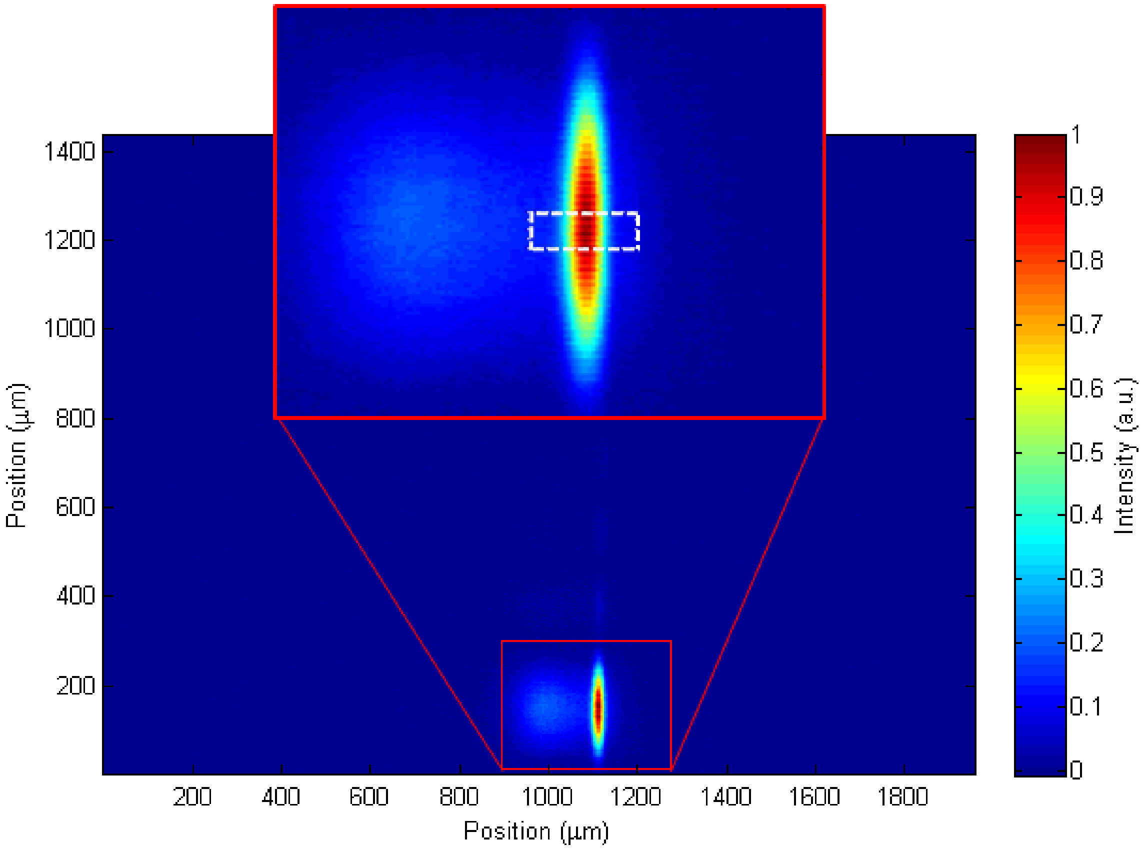

Figure 5.13: Intensity plot of the +1 diffracted order. The axes have been scaled to reflect the beam expander used during imaging, so the dimensions shown indicate the size of the focal point immediately in front of the fabricated sample. The white lines in the insert show the data used to create the profile in Figure 5.14.

As with the -1 diffracted order, the central portion of the focal line was vertically averaged to create a cross-sectional profile of the beam, shown in Figure 5.14. The beam remains Gaussian in shape, and its width at the focal point of the fabricated lens is 20.9±0.9 times narrower than the incident beam. When compared with the expected 21.8 times reduction in beam size, the lens is once again performing close to its expected limits.

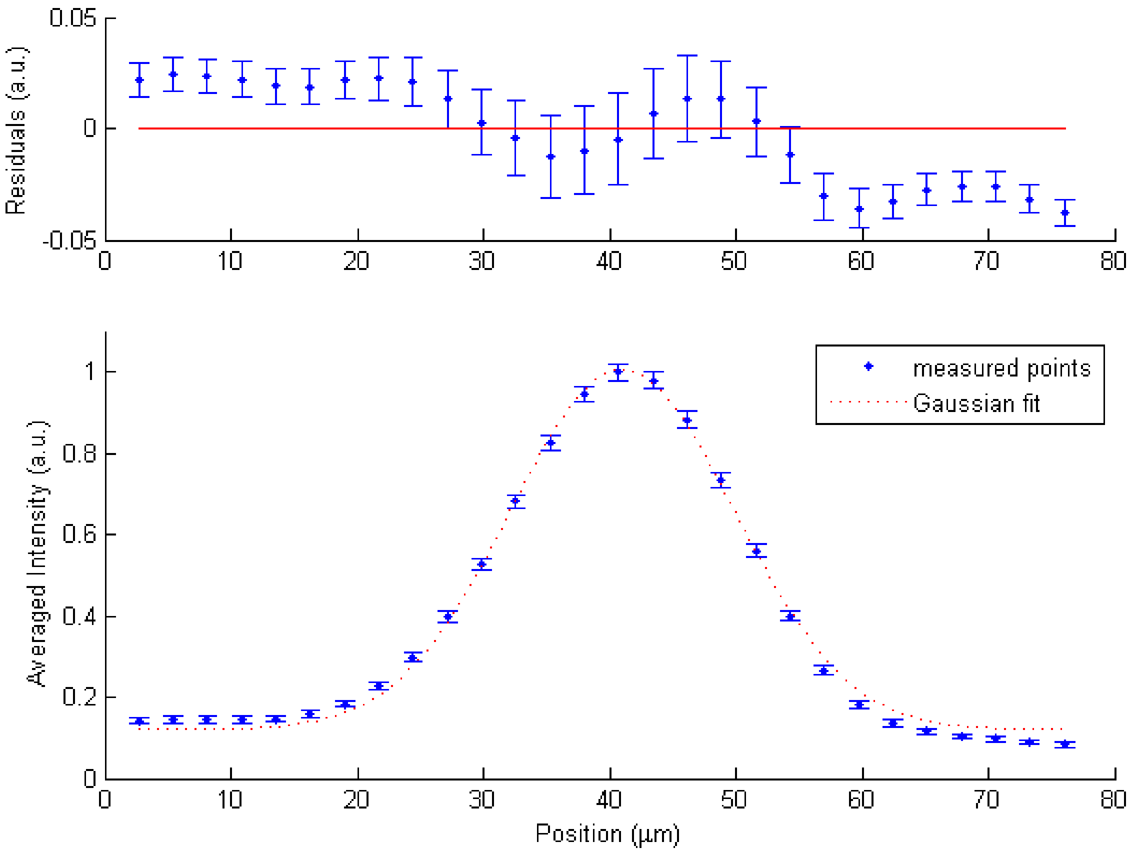

Figure 5.14: Vertically averaged profile of the data highlighted in white in Figure 5.13. The data was fitted to a Gaussian curve of the form $y = a\{\exp[(x-b)/c]^2\}+d$, with fit parameters a = 0.89(2) a.u., b = 41.0(2) µm, c = 12.6(4) µm, d = 0.12(2) a.u.; R-squared = 0.9969.

5.4 Discussion

5.4.1 Efficiency

For both the -1 and +1 diffracted orders, the efficiency of the lens is slightly less than half of what would be expected based on scalar theory for a two-level binary profile. In general, scalar theory is not expected to provide an accurate estimate of efficiency as features become comparable to the wavelength. However, the pitch of this lens was designed to take advantage of the resonance effects that occur for feature pitches approximately 1.5 times the wavelength, similar to previously modelled effects [37]. RCWA modelling of individual zone profiles performed in DiffractMOD indicates that the efficiency of the ideal profile should have comparable efficiency to that predicted by scalar theory. Therefore, this section presents a closer analysis of the various fabrication imperfections that could account for the observed reduction in performance.

One of the main sources of error is the incorrect etch depth, which was approximately 38 nm less than the desired value. The optical path length error will be twice the etch depth error: 76 nm. The effect of an etch depth error can be quantified based upon the amount of destructive interference it would create, given that the normalized intensity of two interfering light waves of equal intensity can be expressed as

$$I = \frac{1}{2}\left[1 + \cos\left(\frac{2\pi n \Delta z}{\lambda}\right)\right], \tag{5.2}$$

for light of wavelength λ travelling in a medium with a refractive index n over a physical path length difference Δz. Therefore, the measured etch depth error would be expected to result in a drop in efficiency of approximately 7.5%. To include this effect in the overall efficiency, the otherwise expected efficiency of 40.5% should be multiplied by the efficiency associated independently with the etch depth error: 100% less its inefficiency of 7.5%; that is, 92.5%. This factor means a reduced overall efficiency of 37.5%, which is also supported by RCWA modelling.

Etching errors also affected the duty cycle of the lens features, owing to the imperfect manner in which the mask profile was transferred to the substrate. The effect of the duty cycle on efficiency can be calculated by determining the first order coefficient for the Fourier series of an infinitely long grating with the measured duty cycle. The measured duty cycle of the lens was on average 52% at the top and 55% at the bottom. Even if the largest duty cycle is used for calculations, the efficiency would only be expected to drop by 2.5%. When included multiplicatively in the same manner described above for the etch depth, this loss brings the overall efficiency to approximately 36.6%. Aside from the direct effects of the etch profile in terms of the duty cycle of the lens, the angled edges are also expected to contribute to unwanted scattering; however, the exact effect of this contribution has not yet been determined.

Another important fabrication imperfection is the variation in feature pitch about the desired trend, which as discussed above in Section 5.2 appears to have a root mean squared deviation of approximately 6 nm. Features with the incorrect pitch would have the effect of providing a certain amount of destructive interference rather than constructive interference at the focal point. Previous work has shown that when the standard deviation of the grating period is equal to 1% of the grating period, its efficiency will drop from 41% to approximately 30%; and that when the standard deviation increases to 2% of the period, the efficiency drops to less than 10% [94]. The standard deviation of 6 nm for the fabricated lens corresponds to about 0.5% of the pitch, suggesting that the variance's contribution to decreased efficiency would be somewhat less than the aforementioned values, conceivably reducing it to about 35%. If it is assumed that this contribution is independent of the etch-depth error contribution and again included multiplicatively, the overall efficiency could be expected to decrease to approximately 32.0%. However, the modelling performed in the reported work was for a grating period of 20 μm, and it is possible that these effects would be even more pronounced for smaller structures.

Surface roughness can also be expected to contribute to scattering losses of the lens, with an estimate of the fractional loss given by [95]

$$\frac{P_S}{P_T} = 1 - e^{-\left(\frac{4\pi\sigma\cos\theta_i}{\lambda}\right)^2}, \qquad (5.3)$$

for scattered power P_S, total power P_T, root mean squared surface roughness σ, incident angle θ_i, and wavelength λ. As seen in Figure 5.5a, the raised portion of the relief structure has noticeably more roughness than the troughs. Atomic force microscopy was used to measure the surface roughness of one of the raised features, indicating a root mean squared roughness of approximately 4 nm. In accordance with Equation 5.3, the resulting scattering should be negligible: less than 0.5%. Scattering from the corrugated side walls of the grating would also contribute to losses, but this contribution was not yet quantified.

The inefficiencies described above do not fully account for the performance of the lens, and more detailed measurements and rigorous analysis would be necessary to fully account for the observed efficiency. A summary of the losses discussed above is provided in Table 5.1, wherein the amount of light remaining after each consideration is listed as a cumulative decrease in observable power.

Table 5.1: Cumulative summary of power loss mechanisms for light observed at the focal point. In each row, the remaining percentage of incident power is calculated as the percentage from the previous row multiplied by the independent efficiency of the factor in consideration (100% minus the independent percentage loss of that factor). In the right-most column, the values are re-normalized to the remaining percentage of light that could be reflected or diffracted off the sample, to more clearly assess the performance of the lens, independent of other losses inherent in the experimental setup. The theoretical efficiency and the actual measured efficiency are bolded.

	independent % loss from each factor	remaining % of incident power	remaining % of light reflected or diffracted off sample
normalized incident power		100	
light in lens	70.0	30.0	
reflectivity of silicon	70.0	9.00	100
theoretical diffraction efficiency	59.5	3.65	**40.5**
etch depth error losses	7.51	3.37	37.5
duty cycle error losses	2.45	3.29	36.6
pitch variation losses	12.5	2.88	32.0
unaccounted inefficiencies	45.3	1.58	**17.5**

In the literature, the design that most closely parallels the lens tested in this thesis is an off-axis lens designed for a wavelength of 780 nm and an incident angle of 30° [66]. Although at the edges of the lens its pitch was 0.74 μm, it also had feature pitches as large as 40 μm. With a reported efficiency of 21%, this lens is of comparable efficiency to the device presented in this thesis, although presumably the larger features contributed a higher efficiency to the lens than the sub-micron features, and therefore the comparison is not entirely valid. Furthermore, this design had a blazed profile, which has a higher theoretical efficiency than a binary profile. Another reasonable device for comparison is not a lens but a blazed grating with a pitch of 4 µm fabricated by EBL, which at a wavelength of 633 nm had a reported efficiency of approximately 50%, compared with the 82% suggested by rigorous theory [69]. Though neither of these examples is identical to the current design, they appear to indicate that for two-level diffractive devices with features close to the wavelength of light, it is not uncommon for the observed efficiency to be considerably lower than that predicted by theory. However, it does seem that with multi-level designs, the observed efficiency tends to more closely match the theory [73, 76], which would hopefully also be the case when fabricating the four-level version of the current design.

5.4.2 Spot Size

Both the -1 and +1 diffractive orders were able to focus the incident beam to a spot size close to the minimum size expected for the fabricated profile. However, the expected spot sizes were approximately 30 and 55 µm, respectively, which are far from diffraction limited. As discussed in Chapter 3, the fabricated design was based upon a linear interpolation of feature pitch between the extreme edges of the design, whereas the optimal trend is actually not linear. Another device fabricated in accordance with the exact zone periods across the entirety of the lens and tested in the correct transmissive configuration would be expected to produce spot sizes considerably closer to the diffraction limit.

5.5 Summary

This chapter has presented the physical and optical characteristics of a diffractive lens that was successfully fabricated with the process flow developed in this thesis project. The results indicate that although the discrepancy between the expected and measured efficiency is not fully accounted for, the efficiency of the device is degraded on account of certain systematic and random fabrication errors. However, the focusing characteristics are shown to be close to what would be expected for the designed profile. Based on these results, the following chapter wraps up this project with a concluding summary and some comments for future improvements.

6 : CONCLUSION

6.1 Summary

This thesis project has successfully demonstrated the development of a high-precision fabrication method for EBL over multiple fields, and has presented the optical results for a diffractive lens fabricated with this process. Although not yet demonstrated for a multi-channel SPR application, the results provide a proof of principle for the optical design.

The fabrication process development was comprised of two main components. The first development stage established a protocol to ensure precise stitching of adjacent EBL fields in both the x and y axes. The automation and repeatability of this method still requires some improvements, but in principle it has been shown that a high degree of precision is possible. Positioning control of the sample stage was demonstrated to a precision of approximately 10 nm. However, the stitching capabilities of the system are in fact limited by rotational misalignments. Rotational control was achieved down to the 0.1° limitation of the microscope, equivalent to approximately 175 nm of lateral misalignment between adjacent 100 µm fields. For applications where this amount of lateral misalignment is unacceptable, one solution would be to write smaller fields, thus decreasing the amount of lateral misalignment caused by the rotational error. In effect this solution would distribute the rotational error into many smaller lateral errors rather than fewer larger lateral errors. The rotational control of the system currently suffers from a lack of repeatability between lithography sessions, which may be possible to overcome by characterizing the rotation error within each lithography session, rather than relying on development and imaging for characterization. For the fabricated lens, the rotational alignment was better than the worst case scenario, and was measured to be 0.03°, equal to less than 50 nm of lateral misalignment between adjacent 92 μm fields. Although the fabricated lens only utilized stitching in one axis, it should be possible to create larger lenses by stitching in both axes once the method is fully automated.

The second fabrication development stage implemented a method to ensure that the width and pitch of specified features were reproduced accurately on the device. For a range of 37 nm in specified feature width variation, the systematic error on the width was 2.2 nm and the random error was approximately 5 nm. Similarly for feature pitch, over a range of 75 nm in specified pitch variation, the systematic error was 10 nm and the random error was approximately 6 nm. This method was sufficient for the diffractive lens, but it is not clear how well it would translate to other cases with a wider range of feature sizes and non-uniform duty cycles. Due to proximity effects in EBL, in general it is probably more difficult to calibrate the measured feature sizes than in this particular case.

Optically, the diffractive lens was tested in a reflective configuration, where it acted as a diverging lens for the -1 diffracted order and a converging lens for the +1 diffracted order. The diffraction efficiency of the lens was approximated to be between 16 and 19%. Of the fabrication errors that were analyzed, the efficiency was primarily limited by an incorrect etch depth and by random variations from the desired feature pitch, although a considerable amount of unaccounted inefficiency also remained. A four level device would be expected to increase the efficiency of the +1 order of the lens by better approximating the desired phase profile, and also because there are more degrees of freedom for optimization using rigorous theory. The observed focal point of the lens was 36 times smaller than the incident beam for the -1 order and 22 times smaller than the incident beam for the +1 order, close to what was predicted by theory. These values were not diffraction limited, and should be improved by fabricating a device with the correct hyperbolic trend in feature variation, rather than the linear trend that was mistakenly designed and then implemented.

6.2 Future Work for SPR Implementation

This thesis does not provide an ultimate answer in terms of the feasibility of the final goal of fabricating a multi-channel SPR sensor. The initial optical results are encouraging, and show that the basic functionality of the designed lens can be implemented in practice. However, the remaining fabrication challenges may severely limit the practicality of scaling up the fabrication process to a device level.

Improving the device from a two-level structure to a four-level structure will be contingent on implementing a spray-coating method for the resist layers, and on aligning the second binary mask pattern with sufficient accuracy to the patterns made in the first iteration of the process. The alignment issue should be solvable by applying similar characterization and adjustment techniques to those used for field stitching, with the added challenge of requiring precise absolute positioning in addition to relative positioning.

To implement the lens in a polymer, the main remaining task is to optimize the etch depth and etch profile. Although not yet attempted, altering the gas composition of the etch recipe should provide the necessary control to improve the etch profile. Replication in a suitable polymer will be performed using the facilities of collaborators at NRC Boucherville.

The most considerable challenges remaining for this project are implementing a full-sized lens and ultimately an entire array of lenses. Currently, each 100 µm by 100 µm EBL field takes approximately 10 minutes to write, and therefore a single lens 2.5 mm by 2.7 mm would require 675 fields to pattern, which would take in excess of 100 hours. One option for overcoming this problem would be to increase the beam current used for writing to decrease the patterning time, although it would be necessary to verify that a satisfactory degree of feature width control remained possible. Although the fabrication time would probably remain at least twenty hours, this investment could be deemed worthwhile if it was confidently expected to produce a master device for mass replication. Alternatively, it might be possible to write the entire width of the lens in the focusing direction, and then implement a moulding or imprinting process to repeatedly pattern this smaller master along the required length in the non-focusing direction. Regardless of which approach is taken, it will certainly be infeasible to create an entire array of lenses with EBL, and a step-and-repeat patterning method would be required. Ultimately, once the design is past the prototyping stage, the dimensions of the design are well within the capabilities of deep UV lithography, which would make mass production of the device considerably more feasible.

In conclusion, the optical results presented in this thesis are significant because they demonstrate that it is possible to create diffractive optics with an in-house fabrication process; however, significant work still remains before a multichannel SPR sensor can be implemented.

APPENDIX: ADDITIONAL TECHNICAL NOTES ON EBL

Chapter 4 describes the process flow and parameters used for fabrication, and also describes the techniques used to overcome challenges encountered with EBL field stitching and line-width control. However, there are other procedures and technical details that may be helpful for future work related to the fabrication of diffractive lenses, or to EBL field stitching in general, which are presented in this appendix.

A.1 Alignment, Focusing, and Stage Control

In addition to the process flow described in Chapter 4, there are a few further details involved in the actual EBL setup procedure that were necessary in order to achieve accurate stitching and precise line-width control.

The sample was set on a bare silicon wafer mounted on the EBL sample holder as shown in Figure A.1. The sample on the left is an astigmatism correction target comprised of gold particles on a copper grid, and was used for preliminary focusing and astigmatism adjustments. The sample on the right was the actual sample to be used for lithography. Extending from near the top-left corner is a scratch made with a diamond scribe after the PMMA and EL 6 were coated on the sample. This mark was used in subsequent imaging sessions as an easy way of locating the fabricated patterns. Near the scratch are four small circles comprised of gold nano-particles. A commercially prepared solution of 50 nm spheres at a concentration of $4.5 \cdot 10^{10}$ particles per millilitre was diluted in ethanol by approximately a factor of 10, and then small drops were applied to the sample. As described below, these four points were used to calibrate the x-y autofocus capability of the NPGS software. Carbon tape was used to secure the sample in place, and also to make it easier to locate the drops of nano-particles under the electron microscope.

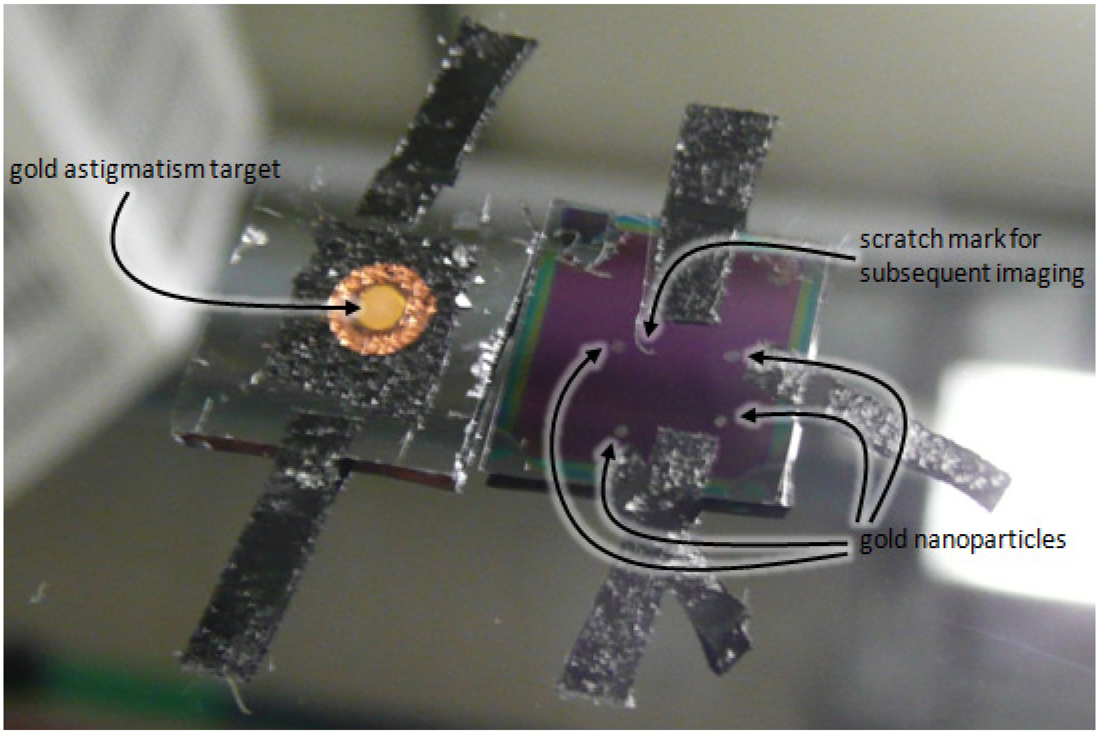

Figure A.1: Photograph of the astigmatism target (left) and sample (right), mounted on the EBL sample holder. The sample is approximately 1.5 cm by 1.5 cm.

After turning on the EBL system following the standard procedure, the raster rotation was set as required by entering the appropriate value under the "SEM" settings tab on the EBL microscope software, shown in Figure A.2. The beam blanker was also set to the "out" position, because at the time this thesis work was performed, other results suggested problems with this component of the EBL system. The beam-blanker allows the electron beam to be deflected away from the sample while the beam is moved to a new position, and is therefore helpful when patterning areas that are not directly connected to each other. However, when it was used it appeared to interfere with accurate focusing when using the x-y autofocus mode described below. Therefore, all focusing adjustments were performed with the beam blanker in the "out" position; however, this problem has subsequently been fixed and it should be possible to do future work with the beam blanker in place.

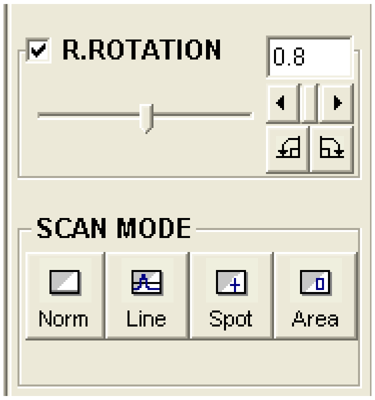

Figure A.2: The raster rotation and spot mode options, located under the "SEM" settings tab of the EBL microscope.

Preliminary aperture alignment, stigma x and y alignment, focusing, and astigmatism correction were performed using the astigmatism correction target. An example of the type of image obtained after these adjustments is shown in Figure A.3a. The correction target was set on a different sample of silicon than the sample actually to be used for EBL, and therefore it was not at the exact same working distance as the lithography sample and could not be used to exactly focus the electron beam for lithography work. However, it provided a preliminary method of adjustment that would ensure that the focus and astigmatism were set at approximately the right positions, thus making subsequent improvements to the beam alignment easier.

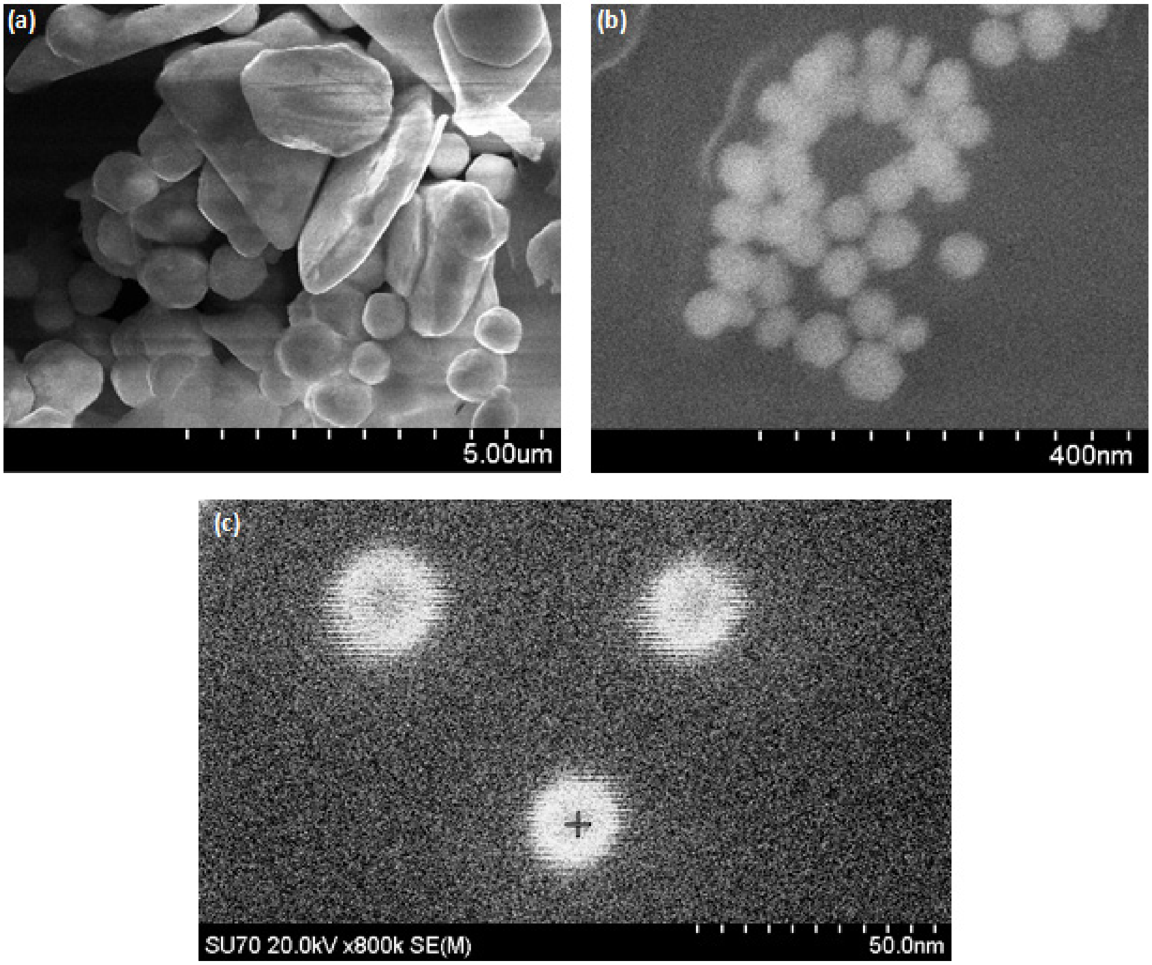

Figure A.3: SEM images obtained during the focusing procedure for EBL. **(a)** Gold particles on astigmatism test target, imaged at 10 kx magnification. **(b)** 50 nm gold nano-particles on the PMMA surface, imaged at 130 kx magnification. **(c)** PMMA spot-burns, imaged at 800 kx magnification. The cross-hair in the bottom spot is a screen-artifact and not part of the actual image.

After focusing on the astigmatism target, focusing was performed at the edge of one of the four droplets of gold nano-particles shown in Figure A.0.1. Further adjustment to the aperture alignment, stigma x and y alignment, focusing, and astigmatism was typically necessary. A satisfactory image obtained after these adjustments is shown in Figure A.3b.

As a final confirmation that astigmatism adjustments were acceptable, the beam was “spot-burned” into the resist, using the “spot” function shown in Figure A.2. This technique holds the beam stationary on one point for an extended period, thus polymerizing the resist in an observable manner. If the beam is well-adjusted for astigmatism the spot should be round, if not it will appear skewed. An initial spot burn was performed at 220 kx magnification for approximately 30 seconds, followed by several shorter spot burns at 800 kx magnification for approximately 3 seconds. Further astigmatism and focusing adjustments were performed as necessary. An example of well-adjusted spot burns is shown in Figure A.3c.

After these adjustments, the first x-y autofocus point was read into the NPGS system. For the remaining three points, focusing was repeated first on the gold nano-particles and then with spot-burning. The focus was adjusted as necessary, but the astigmatism and other beam alignment tools were not adjusted from the positions set at the first focus point.

Prior to writing the patterns, the stage controller was also set such that it will continue to activate the piezo controllers while a pattern is being written, thus preventing drift in the stage position. On the stage controller itself, this feature is activated by selecting “cal”, then “setup”, then “piezo”. All values should be unchanged (pressing “enter” advances to the next option), except that “hold on/off” should be set to 1, and “hold time” should be set to 0, which actually tells the stage to wait indefinitely in the hold position until another command is provided. In order to interface correctly with NPGS, the project folder in use for NPGS must contain a system file named “Pg_Sprite.sys” rather than the default “sprite32.sys” to interface with the stage controller while the piezo controllers remain activated. This stage driver must also be selected in NPGS by going to “Options”, “System Files...”, and “PG_STG.sys”. If all these parameters have been set correctly, the single speed arrow on the stage controller will continue to flash while the pattern is being written, as opposed to turning solid once the stage has determined that it is in the correct position.

A.2 MAGscale

The MAGscale parameter is defined as the microscope's magnification multiplied by the field width. Intuitively what this factor means is that as the magnification of the microscope is increased, the field of view of the sample will be decreased, and the MAGscale is the constant that relates these two parameters for a given working distance. The importance of the MAGscale parameter in EBL is that it allows NPGS to calculate the appropriate beam deflection required to create a feature of a certain size; in other words, it allows for the correct scaling of software patterns. It also determines the size of a single EBL field, which dictates how far the stage should move between adjacent fields.

Ideally, the MAGscale is set by using a calibration grid with very well-defined spacing, but in reality, a sample at a slightly different height from that of the calibration grid will not require exactly the same value. Instead, it is possible to use pre-patterned features on the sample to be used for lithography to perform a MAGscale calibration at the start of each session.

However, for the current work, efforts were made to ensure that between separate lithography sessions the height of the sample was kept constant, which should mean that the ideal MAGscale value would remain essentially constant. Small corrections to the MAGscale were then performed based upon observed results in adjacent lithography fields. The approach taken for these corrections is illustrated schematically and with representative SEM images in Figure A.4. If the MAGscale value is set correctly, NPGS will determine the field size at a given magnification, and will write features of the correct size and also correctly calculate the distance the stage should move between adjacent fields. However, if the MAGscale value is too large, NPGS will calculate that the field size is larger than it actually is. Therefore, it will provide smaller deflection voltages to write certain features than actually required, and will also calculate that the stage needs to move further than it actually should between adjacent fields. By observing the resulting gap or overlap between adjacent fields, it was possible to alter the MAGscale value as necessary. The MAGscale can be adjusted in NPGS by selecting the “Options” menu, then “System Files...”, and “PG.sys”.

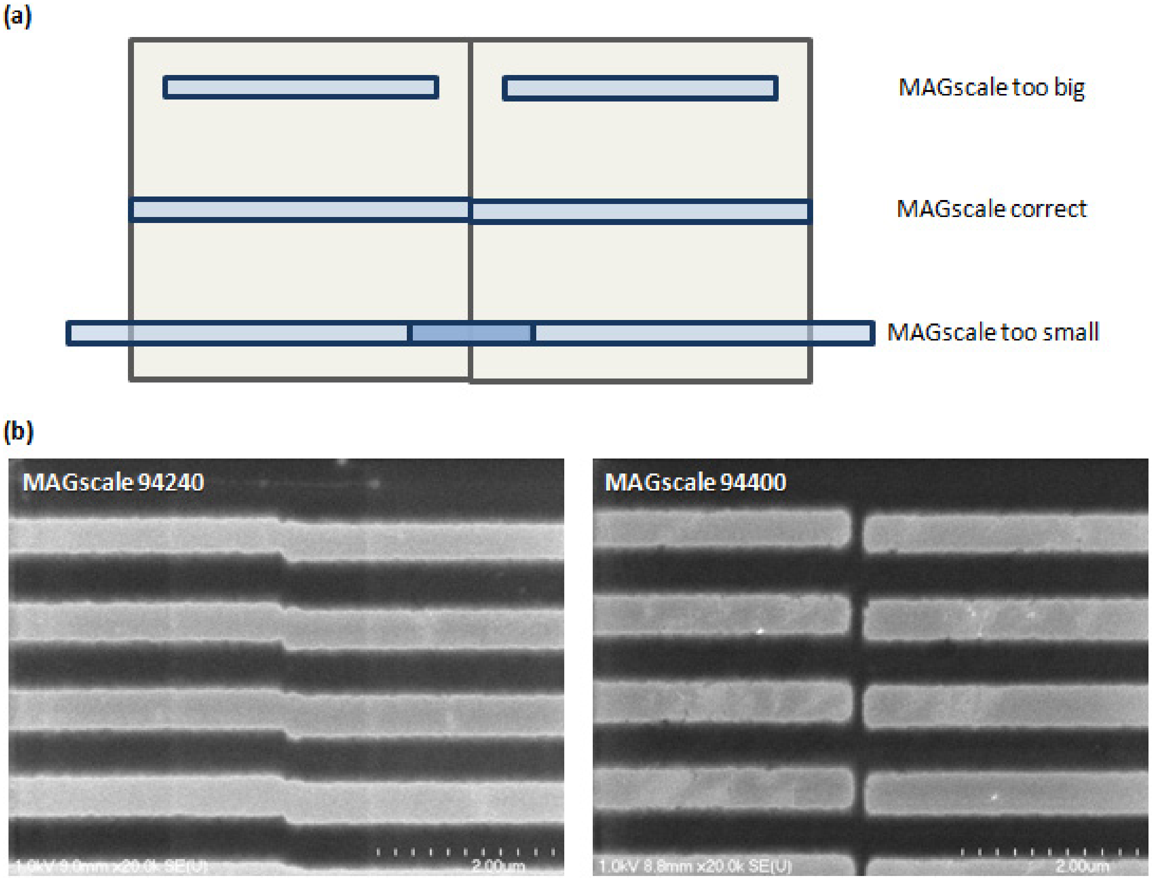

Figure A.4: (a) Schematic illustration of the effects of the MAGscale parameter when writing a line across the entire width of two adjacent EBL fields. **(b)** SEM images of two examples of fabricated lines with different MAGscale values.

A.3 Deflection Voltage

The MAGscale parameter discussed above should provide accurate scaling in both the x and y axes. However, in one axis or the other, some additional fine-tuning may be required to ensure there is no gap or overlap present between adjacent fields. These adjustments are done by modifying the maximum deflection voltage for either the x or y axis, which is done in NPGS by selecting the “Options” menu, then “System Files...”, and “PG.sys”. Using a similar pattern evaluation technique to that described for MAGscale adjustments, the effect of different maximum y-axis deflection voltages was assessed as shown in Figure A.5.

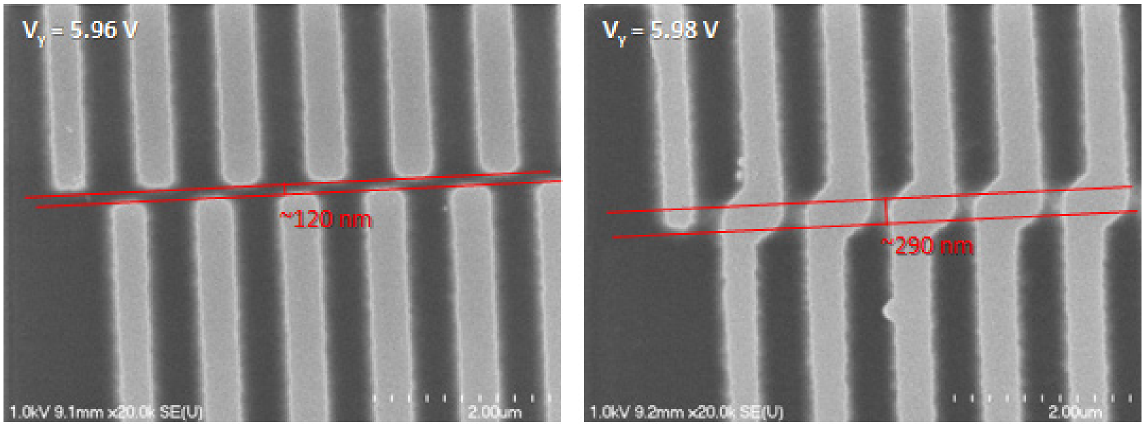

Figure A.5: SEM images of lines written with different maximum deflection voltages for the y-axis. The positioning of adjacent fields in the x-direction is not correct, but the gap or overlap in the y-direction created by the voltage deflection is apparent. The optimum deflection voltage appears to be approximately 5.97 V.

REFERENCES

[1] F. B. Myers and L. P. Lee, "Innovations in optical microfluidic technologies for point-of-care diagnostics," *Lab Chip,* vol. 8, pp. 2015-2031, 2008.

[2] P. Yager, T. Edwards, E. Fu, K. Helton, K. Nelson, M. R. Tam, and B. H. Weigl, "Microfluidic diagnostic technologies for global public health," *Nature,* vol. 442, pp. 412-418, 2006.

[3] M. A. Cooper, "Optical biosensors in drug discovery," *Nature Reviews Drug Discovery,* vol. 1, pp. 515-528, 2002.

[4] P. S. Dittrich and A. Manz, "Lab-on-a-chip: microfluidics in drug discovery," *Nature Reviews Drug Discovery,* vol. 5, pp. 210-218, 2006.

[5] M. Packirisamy and S. Badilescu, *BioMEMS: Science and Engineering Perspectives*. Boca Raton: Taylor & Francis/CRC Press, 2011.

[6] C. Dass, *Fundamentals of Contemporary Mass Spectrometry*. Hoboken: John Wiley & Sons, 2007.

[7] J. Franzke, K. Kunze, M. Miclea, and K. Niemax, "Microplasmas for analytical spectrometry," *Journal of Analytical Atomic Spectrometry,* vol. 18, pp. 802-807, 2003.

[8] D. Janasek, J. Franzke, and A. Manz, "Scaling and the design of miniaturized chemical-analysis systems," *Nature,* vol. 442, pp. 374-380, 2006.

[9] J. Homola, "Present and future of surface plasmon resonance biosensors," *Analytical and Bioanalytical Chemistry,* vol. 377, pp. 528-539, 2003.

[10] D. Mustafa, T. Yang, Z. Xuan, S. Chen, H. Tu, and A. Zhang, "Surface Plasmon Coupling Effect of Gold Nanoparticles with Different Shape and Size on Conventional Surface Plasmon Resonance Signal," *Plasmonics,* vol. 5, pp. 221-231, 2010.

[11] S. Kawata, "Near-field microscope probes utilizing surface plasmon polaritons," in *Near-Field Optics and Surface Plasmon Polaritons*. vol. 81, S. Kawata, Ed., ed Heidelberg: Spring-Verlag, 2001.

[12] M. Piliarik and J. Homola, "SPR sensor instrumentation," in *Surface Plasmon Resonance Based Sensors*, J. Homola, Ed., ed Berlin: Springer Verlag, 2006.

[13] E. Kretschmann and H. Raether, "Radiative decay of non radiative surface plasmons excited by light," *Zeitschrift Fuer Naturforschung (Astrophysik, Physik und Physikalische Chemie),* vol. 23a, pp. 2135-2136, 1968.

[14] G. G. Nenninger, M. Piliarik, and J. Homola, "Data analysis for optical sensors based on spectroscopy of surface plasmons," *Measurement Science and Technology,* vol. 13, p. 2038, 2002.

[15] X. D. Hoa, A. G. Kirk, and M. Tabrizian, "Towards integrated and sensitive surface plasmon resonance biosensors: a review of recent progress," *Biosensors and Bioelectronics,* vol. 23, pp. 151-160, 2007.

[16] J. Homola, "Surface plasmon resonance sensors for detection of chemical and biological species," *Chemical Reviews,* vol. 108, p. 462, 2008.

[17] S. Löfås and A. McWhirter, "The art of immobilization for SPR sensors," in *Surface Plasmon Resonance Based Sensors*, J. Homola, Ed., ed Berlin: Springer Verlag, 2006.

[18] E. Baldrich, O. Laczka, F. J. Del Campo, and F. X. Muñoz, "Gold immuno-functionalisation via self-assembled monolayers: Study of critical parameters and comparative performance for protein and bacteria detection," *Journal of Immunological Methods,* vol. 336, pp. 203-212, 2008.

[19] A. D. Taylor, J. Ladd, J. Homola, and S. Jiang, "Surface Plasmon Resonance (SPR) Sensors for the Detection of Bacterial Pathogens

Principles of Bacterial Detection: Biosensors, Recognition Receptors and Microsystems," M. Zourob, S. Elwary, and A. Turner, Eds., ed: Springer New York, 2008, pp. 83-108.

[20] M. Piliarik and J. Homola, "Surface plasmon resonance (SPR) sensors: approaching their limits?," *Optics Express,* vol. 17, pp. 16505-16517, 2009.

[21] H. Wang, Z. Wang, M. Lu, and H. Zou, "Microdialysis Sampling Method for Evaluation of Binding Kinetics of Small Molecules to Macromolecules," *Analytical Chemistry,* vol. 80, pp. 2993-2999, 2008.

[22] A. N. Naimushin, S. D. Soelberg, D. U. Bartholomew, J. L. Elkind, and C. E. Furlong, "A portable surface plasmon resonance (SPR) sensor system with temperature regulation," *Sensors and Actuators B: Chemical,* vol. 96, pp. 253-260, 2003.

[23] C. Nylander, B. Liedberg, and T. Lind, "Gas detection by means of surface plasmon resonance," *Sensors and Actuators,* vol. 3, pp. 79-88, 1982.

[24] T. Okamoto and I. Yamaguchi, "Surface plasmon microscope with an electronic angular scanning," *Optics Communications,* vol. 93, pp. 265-270, 1992.

[25] K. Matsubara, S. Kawata, and S. Minami, "Optical chemical sensor based on surface plasmon measurement," *Applied Optics,* vol. 27, pp. 1160-1163, 1988.

[26] J. F. Masson, Y. C. Kim, L. A. Obando, W. Peng, and K. S. Booksh, "Fiber-optic surface plasmon resonance sensors in the near-infrared spectral region," *Applied Spectroscopy,* vol. 60, pp. 1241-1246, 2006.

[27] A. Suzuki, J. Kondoh, Y. Matsui, S. Shiokawa, and K. Suzuki, "Development of novel optical waveguide surface plasmon resonance (SPR) sensor with dual light emitting diodes," *Sensors and Actuators B: Chemical,* vol. 106, pp. 383-387, 2005.

[28] M. Piliarik, H. Vaisocherová, and J. Homola, "Towards parallelized surface plasmon resonance sensor platform for sensitive detection of oligonucleotides," *Sensors and Actuators B: Chemical,* vol. 121, pp. 187-193, 2007.

[29] T. Chinowsky, J. Quinn, D. Bartholomew, R. Kaiser, and J. Elkind, "Performance of the Spreeta 2000 integrated surface plasmon resonance affinity sensor," *Sensors and Actuators B: Chemical,* vol. 91, pp. 266-274, 2003.

[30] C. Thirstrup, W. Zong, M. Borre, H. Neff, H. Pedersen, and G. Holzhueter, "Diffractive optical coupling element for surface plasmon resonance sensors," *Sensors and Actuators B: Chemical,* vol. 100, pp. 298-308, 2004.

[31] W. Y. Chien, M. Z. Khalid, X. D. Hoa, and A. G. Kirk, "Monolithically integrated surface plasmon resonance sensor based on focusing diffractive optic element for optofluidic platforms," *Sensors and Actuators B: Chemical,* vol. 138, pp. 441-445, 2009.

[32] G. J. Swanson, "Binary optics technology: theoretical limits on the diffraction efficiency of multilevel diffractive optical elements," DTIC Document, 1991.

[33] M. B. Stern, "Pattern transfer for diffractive and refractive microoptics," *Microelectronic Engineering,* vol. 34, pp. 299-319, 1997.

[34] E. Hecht, "Optics," 4th ed. San Francisco: Addison-Wesley, 2002.

[35] N. F. Borrelli, *Microoptics Technology*, 2nd ed. New York: Marcel Dekker Inc, 2005.

[36] E. Noponen, J. Turunen, and A. Vasara, "Parametric optimization of multilevel diffractive optical elements by electromagnetic theory," *Applied Optics,* vol. 31, pp. 5910-5912, 1992.

[37] E. Noponen, J. Turunen, and A. Vasara, "Electromagnetic theory and design of diffractive-lens arrays," *Journal of the Optical Society of America A* vol. 10, pp. 434-443, 1993.

[38] Y. Sheng, D. Feng, and S. Larochelle, "Analysis and synthesis of circular diffractive lens with local linear grating model and rigorous coupled-wave theory," *J. Opt. Soc. Am. A,* vol. 14, pp. 1562-1568, 1997.

[39] F. J. Pedrotti and L. S. Pedrotti, "Introduction to Optics," 2nd ed: Prentice-Hall, Inc, 1993.

[40] B. Kress and P. Meyrueis, *Digital Diffractive Optics: An Introduction to Planar Diffractive Optics and Related Technology*: Wiley-VCH, 2000.

[41] J. E. Harvey and E. A. Nevis, "Angular grating anomalies: effects of finite beam size on wide-angle diffraction phenomena," *Applied Optics,* vol. 31, pp. 6783-6788, 1992.

[42] J. W. Goodman, *Introduction to Fourier Optics*, 2nd ed. Boston: McGraw-Hill, 1996.

[43] J. Jarem and P. P. Banerjee, *Computational Methods for Electromagnetic and Optical Systems*, 2nd ed. vol. 149. Boca Raton: CRC Press, 2011.

[44] M. G. Moharam and T. K. Gaylord, "Rigorous coupled-wave analysis of planar-grating diffraction," *Journal of the Optical Society of America,* vol. 71, pp. 811-818, 1981.

[45] K. Hirayama, E. N. Glytsis, T. K. Gaylord, and D. W. Wilson, "Rigorous electromagnetic analysis of diffractive cylindrical lenses," *Journal of the Optical Society of America A,* vol. 13, pp. 2219-2231, 1996.

[46] E. N. Glytsis, M. E. Harrigan, T. K. Gaylord, and K. Hirayama, "Effects of fabrication errors on the performance of cylindrical diffractive lenses: rigorous boundary-element method and scalar approximation," *Applied Optics,* vol. 37, pp. 6591-6602, 1998.

[47] M. Totzeck, W. Ulrich, A. Gohnermeier, and W. Kaiser, "Semiconductor fabrication: Pushing deep ultraviolet lithography to its limits," *Nature Photonics,* vol. 1, pp. 629-631, 2007.

[48] S. Damaraju, V. George, S. Jahagirdar, T. Khondker, R. Milstrey, S. Sarkar, S. Siers, I. Stolero, and A. Subbiah, "A 22nm IA multi-CPU and GPU System-on-Chip," in *Solid-State Circuits Conference Digest of Technical Papers (ISSCC), 2012 IEEE International*, 2012, pp. 56-57.

[49] M. J. Madou, *Fundamentals of microfabrication: the science of miniaturization*, 2nd ed.: CRC, 2002.

[50] K. Yamazaki, "Electron beam direct writing," in *Nanofabrication: fundamentals and applications*, A. A. Tseng, Ed., ed: World Scientific Pub Co Inc, 2008.

[51] G. Wiederrecht, *Handbook of nanofabrication*: Academic Press, 2010.

[52] L. Reimer, *Scanning Electron Microscopy: Physics of Image Formation and Microanalysis*. Berlin: Springer, 1998.

[53] Hitachi High-Technologies Corporation, "Instruction manual for model SU-70 ultra-high resolution analytical scanning electron microscope," Japan. 2006.

[54] A. A. Tseng, C. Kuan, C. D. Chen, and K. J. Ma, "Electron beam lithography in nanoscale fabrication: recent development," *Electronics Packaging Manufacturing, IEEE Transactions on,* vol. 26, pp. 141-149, 2003.

[55] M. J. Bowden, "Electron irradiation of polymers and its application to resists for electron-beam lithography," *Critical Reviews in Solid State and Material Sciences,* vol. 8, pp. 223-264, 1979.

[56] T. Ishigure, E. Nihei, and Y. Koike, "Optimum refractive-index profile of the graded-index polymer optical fiber, toward gigabit data links," *Applied Optics,* vol. 35, pp. 2048-2053, 1996.

[57] Microchem Corp., "Nano PMMA and Copolymer,". Newton, MA., 2001.

[58] G. H. Bernstein, D. A. Hill, and W.-P. Liu, "New high-contrast developers for poly(methyl methacrylate) resist," *Journal of Applied Physics,* vol. 71, pp. 4066-4075, 1992.

[59] B. Cord, J. Yang, H. Duan, D. C. Joy, J. Klingfus, and K. K. Berggren, "Limiting factors in sub-10 nm scanning-electron-beam lithography," *Journal of Vacuum Science & Technology B: Microelectronics and Nanometer Structures,* vol. 27, p. 2616, 2009.

[60] T. H. P. Chang, "Proximity effect in electron-beam lithography," *Journal of Vacuum Science and Technology,* vol. 12, pp. 1271-1275, 1975.

[61] D. Gil, R. Menon, and H. I. Smith, "Fabrication of high-numerical-aperture phase zone plates with a single lithography exposure and no etching," *Journal of Vacuum Science & Technology B: Microelectronics and Nanometer Structures,* vol. 21, p. 2956, 2003.

[62] C. G. Blough, M. Rossi, S. K. Mack, and R. L. Michaels, "Single-point diamond turning and replication of visible and near-infrared diffractive optical elements," *Applied Optics,* vol. 36, pp. 4648-4654, 1997.

[63] A. G. Poleshchuk, E. G. Churin, V. P. Koronkevich, V. P. Korolkov, A. A. Kharissov, V. V. Cherkashin, V. P. Kiryanov, A. V. Kiryanov, S. A. Kokarev, and A. G. Verhoglyad, "Polar coordinate laser pattern generator for fabrication of diffractive optical elements with arbitrary structure," *Applied Optics,* vol. 38, pp. 1295-1301, 1999.

[64] K. Kawamura, T. Ogawa, N. Sarukura, M. Hirano, and H. Hosono, "Fabrication of surface relief gratings on transparent dielectric materials by two-beam holographic method using infrared femtosecond laser pulses," *Applied Physics B: Lasers and Optics,* vol. 71, pp. 119-121, 2000.

[65] T. Fujita, H. Nishihara, and J. Koyama, "Fabrication of micro lenses using electron-beam lithography," *Opt. Lett.,* vol. 6, pp. 613-615, 1981.

[66] G.-i. Hatakoshi and K. Goto, "Grating lenses for the semiconductor laser wavelength," *Applied Optics,* vol. 24, pp. 4307-4311, 1985.

[67] J. Kim, K. Jalhadi, S. Y. Lee, and D. Joy, "Fabrication of a Fresnel zone plate through electron beam lithographic process and its application to measuring of critical dimension scanning electron microscope performance," *Journal of Vacuum Science & Technology B: Microelectronics and Nanometer Structures,* vol. 25, p. 1771, 2007.

[68] H. C. Liou and J. Pretzer, "Effect of curing temperature on the mechanical properties of hydrogen silsesquioxane thin films," *Thin Solid Films,* vol. 335, pp. 186-191, 1998.

[69] P. Laakkonen, J. Lautanen, V. Kettunen, J. Turunen, and M. Schirmer, "Multilevel diffractive elements in SiO2 by electron beam lithography and proportional etching with analogue negative resist," *Journal of Modern Optics,* vol. 46, pp. 1295-1307, 1999/07/01 1999.

[70] X. Cheng and L. Jay Guo, "A combined-nanoimprint-and-photolithography patterning technique," *Microelectronic Engineering,* vol. 71, pp. 277-282, 2004.

[71] C. David and D. Hambach, "Line width control using a defocused low voltage electron beam," *Microelectronic Engineering,* vol. 46, pp. 219-222, 1999.

[72] C. David and A. Souvorov, "High-efficiency Bragg–Fresnel lenses with 100 nm outermost zone width," *Review of scientific instruments,* vol. 70, p. 4168, 1999.

[73] A. Kowalik, K. Góra, Z. Jaroszewicz, and A. Kołodziejczyk, "Multi-step electron beam technology for the fabrication of high performance diffractive optical elements," *Microelectronic Engineering,* vol. 77, pp. 347-357, 2005.

[74] J. Kim, D. Joy, and S. Y. Lee, "Controlling resist thickness and etch depth for fabrication of 3D structures in electron-beam grayscale lithography," *Microelectronic Engineering,* vol. 84, pp. 2859-2864, 2007.

[75] J. M. Moran and D. Maydan, "High resolution, steep profile resist patterns," *Journal of Vacuum Science and Technology,* vol. 16, pp. 1620-1624, 1979.

[76] F. T. Chen and H. G. Craighead, "Diffractive lens fabricated with mostly zeroth-order gratings," *Opt. Lett.,* vol. 21, pp. 177-179, 1996.

[77] J. N. Mait, A. Scherer, O. Dial, D. W. Prather, and X. Gao, "Diffractive lens fabricated with binary features less than 60 nm," *Opt. Lett.,* vol. 25, pp. 381-383, 2000.

[78] T. J. Suleski and R. D. T. Kolste, "Fabrication trends for free-space microoptics," *Lightwave Technology, Journal of,* vol. 23, pp. 633-646, 2005.

[79] S. Y. Chou, P. R. Krauss, and P. J. Renstrom, "Imprint Lithography with 25-Nanometer Resolution," *Science,* vol. 272, pp. 85-87, April 5, 1996 1996.

[80] S. Y. Chou, P. R. Krauss, W. Zhang, L. Guo, and L. Zhuang, "Sub-10 nm imprint lithography and applications," *Journal of Vacuum Science & Technology B: Microelectronics and Nanometer Structures,* vol. 15, pp. 2897-2904, 1997.

[81] C. Peroz, V. Reboud, and C. M. S. Torres, "Nanoimprint Technologies Nanofabrication," M. Stepanova and S. Dew, Eds., ed: Springer Vienna, 2012, pp. 117-140.

[82] S. R. Quake and A. Scherer, "From Micro- to Nanofabrication with Soft Materials," *Science,* vol. 290, pp. 1536-1540, November 24, 2000 2000.

[83] J. Seekamp, S. Zankovych, A. Helfer, P. Maury, C. Torres, G. Boettger, C. Liguda, M. Eich, B. Heidari, and L. Montelius, "Nanoimprinted passive optical devices," *Nanotechnology,* vol. 13, p. 581, 2002.

[84] Y. Xia and G. M. Whitesides, "Soft Lithography," *Annual Review of Materials Science,* vol. 28, pp. 153-184, 1998.

[85] Y. Xia, E. Kim, X.-M. Zhao, J. A. Rogers, M. Prentiss, and G. M. Whitesides, "Complex Optical Surfaces Formed by Replica Molding Against Elastomeric Masters," *Science,* vol. 273, pp. 347-349, July 19, 1996 1996.

[86] L. Malic, T. Veres, and M. Tabrizian, "Biochip functionalization using electrowetting-on-dielectric digital microfluidics for surface plasmon resonance imaging detection of DNA hybridization," *Biosensors and Bioelectronics,* vol. 24, pp. 2218-2224, 2009.

[87] J. Homola, I. Koudela, and S. S. Yee, "Surface plasmon resonance sensors based on diffraction gratings and prism couplers: sensitivity comparison," *Sensors and Actuators B: Chemical,* vol. 54, pp. 16-24, 1999.

[88] F. Semendy, P. Wijewarnasuriya, and N. K. Dhar, "High efficiency c-silicon solar cells based on micro-nanoscale structure," Army Research Labratory, Defense Technical Information Center ARL-TR-5576, 2011.

[89] S. A. Vitale, H. Chae, and H. H. Sawin, "Silicon etching yields in F, Cl, Br, and HBr high density plasmas," *Journal of Vacuum Science & Technology A: Vacuum, Surfaces, and Films,* vol. 19, p. 2197, 2001.

[90] M. Vyvoda, H. Lee, M. Malyshev, F. Klemens, M. Cerullo, V. Donnelly, D. Graves, A. Kornblit, and J. Lee, "Effects of plasma conditions on the shapes of features etched in Cl2 and HBr plasmas. I. Bulk crystalline silicon etching," *Journal of Vacuum Science & Technology A: Vacuum, Surfaces, and Films,* vol. 16, pp. 3247-3258, 1998.

[91] J. P. Beasley and D. G. Squire, "An electron beam maskmaker," *Electron Devices, IEEE Transactions on,* vol. 22, pp. 376-384, 1975.

[92] A. Hasegawa, R. I. Kang, and K. Shono, "Electron beam direct lithography system using the SEM," *Electronics and Communications in Japan (Part II: Electronics),* vol. 75, pp. 51-61, 1992.

[93] D. L. Vezie, E. L. Thomas, and W. W. Adams, "Low-voltage, high-resolution scanning electron microscopy: a new characterization technique for polymer morphology," *Polymer,* vol. 36, pp. 1761-1779, 1995.

[94] F. J. Torcal-Milla, L. M. Sanchez-Brea, and E. Bernabeu, "Diffraction of gratings with rough edges," *Opt. Express,* vol. 16, pp. 19757-19769, 2008.

[95] C. Marxer, C. Thio, M. A. Gretillat, N. F. de Rooij, R. Battig, O. Anthamatten, B. Valk, and P. Vogel, "Vertical mirrors fabricated by deep reactive ion etching for fiber-optic switching applications," *Microelectromechanical Systems, Journal of,* vol. 6, pp. 277-285, 1997.